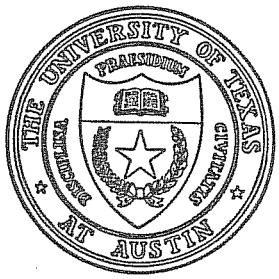

CRACK DETECTION IN NAVAL CRANE SHAFTS USING ACOUSTIC EMISSION

Timothy J. Fowler, Parry C. Berkowitzi

PHIL M. FERGUSON STRUCTURAL ENGINEERING LABORATORY
Department of Civil Engineering / Bureau of Engineering Researc
The University of Texas at Austin

CRACK DETECTION IN NAVAL CRANE SHAFTS USING ACOUSTIC EMISSION

Prepared by:

Dr. Timothy J. Fowler Parry C. Berkowitz

Ferguson Structural Engineering Laboratory
The University of Texas at Austin
J. J. Pickle Research Campus
10200 Burnet Rd., Bldg. #177
Austin, TX 78758

INTRODUCTION

In recent years, the United States Navy has experienced several failures of spool and rotate pinion (sluing) drive shafts. These failures have resulted in uncontrolled dropping of the sometimes sensitive payloads being lifted. The following is an excerpt from a report detailing one such failure:[1]

> On February 28, 1995 a catastrophic failure occurred in the rotate pinion (i.e., sluing) shaft of Naval Crane P-71 at Pearl Harbor Naval Shipyard (PHNS). The 25 ton portal crane was manufactured by R. W. Kaltenbach Corporation in 1945. The failed shaft, from the sluing assembly of a crane rated to 56,000 lbs, failed at the inside (or top) face of the pinion gear while lifting a 16,000 pound load. Fracture occurred at the transition in diameter where the shaft is reduced to accommodate the pinion gear. The failed crane is a single rotate system; if the single rotate pinion shaft fails, no backup system prevents the machinery house from rotating.
>
> Plastic deformation, i.e., necking, was not evident at the failure surface, indicating failure by slow growth of cracks. Fracture surface appearance of the failed shaft indicate that the fatigue cracks initiated at the shaft's surface and propagated towards the shaft center. The smooth, shiny appearance of the fatigue crack faces near the surface reveal that the faces rubbed together, indicating that the cracks propagated during high repetition cycling under nominal loads. Final failure occurred by rapid crack propagation in a small region of the shafts center, also characteristic of damage progression under nominal loads. The above indications lead to the conclusion that failure was caused by reverse torsional fatigue.

Figure 1.1 shows a typical Navy portal crane. These cranes are primarily located in naval shipyards where they are used to transfer payload to and from aircraft carriers, battleships, and submarines. Figure 1.2 shows a spool drive shaft and drum. The fracture, detailed in the failure report excerpt, occurred near the interlocking gears seen in the center of the photograph.

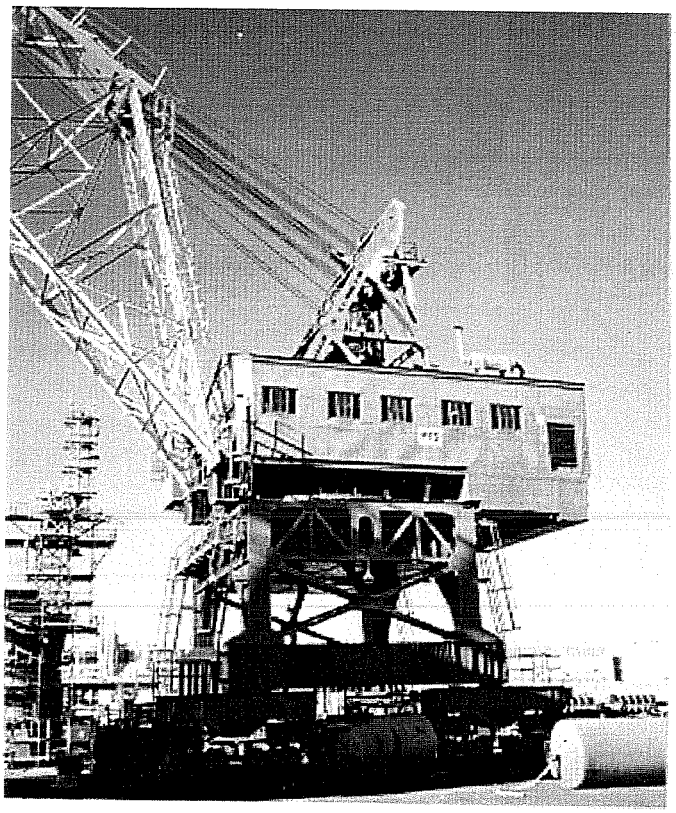

Figure 1.1: Typical Naval Portal Crane

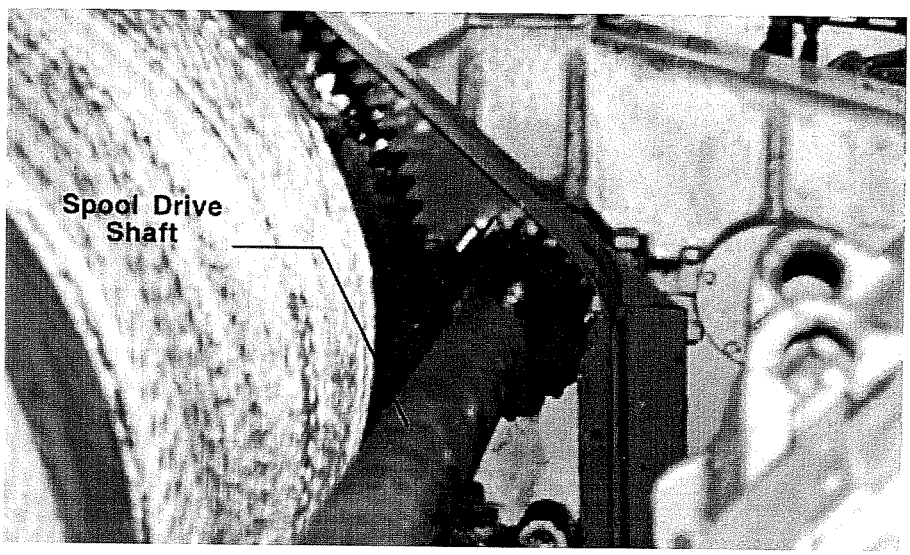

Figure 1.2: Spool Drive Shaft and Drum In-Situ

To locate the defects responsible for the observed failures using conventional nondestructive testing techniques, such as ultrasonic inspection and magnetic particle inspection, would require substantial disassembly of the crane in order to gain access to the areas of interest. The process of disassembling and reassembling the crane is many orders of magnitude more costly than the nondestructive test itself. It is estimated that there are approximately nine thousand of these cranes in the Navy's inventory, and thus a clear need is evident for a global nondestructive testing technique that may be applied in-situ which can detect fatigue cracks in the crane shafts. The global technique, in conjunction with complimentary nondestructive evaluation techniques for follow-up localized inspection if necessary, will allow the Navy to diagnose the health of their cranes without having to withstand the economic burden of disassembling each one before it can be inspected.

Following the failure of the first crane shaft, the Navy ordered all other crane shafts from the same manufacturer and vintage to be nondestructively examined for cracks. The Navy's in-house NDT personnel used both ultrasonic, and wet fluorescent magnetic particle testing to try and detect the cracks. The results were less than satisfactory.

The geometry of the shaft, especially in-situ, makes obtaining good results with traditional NDT methods very difficult. The problems experienced by the Navy were that one of the methods would give a positive indication of a defect, and then the other method would not. In one case, both methods gave no indications and then the shaft failed catastrophically only a few days after the inspection took place. The failure analysis revealed the presence of a major structural crack in the location where it was suspected when the nondestructive examination was ordered. It is impossible to say with any degree of certainty why the defect was missed. As with most traditional applications of the aforementioned NDT techniques, operator skill and acuity play a key role in the sensitivity of the method. This is yet another reason why a global nondestructive testing technique which has a clearly identified evaluation criteria is needed in order to assure the continued safe operation of the cranes.

BACKGROUND THEORY

2.1 ACOUSTIC EMISSION

Acoustic emission is an important tool for assessing the structural integrity of equipment in the chemical and petroleum industries. Over the past twenty years it has developed into a reliable, cost effective indicator of structural problems, and is now viewed as a mature technology. The method is used extensively for in-service examination of "cherry picker" manlifts, pressure vessels, tanks, and tank cars. There are many standard test procedures which use acoustic emission as the sole means to evaluate the health of equipment. Examples include: Section V of the American Society of Mechanical Engineers Code[8], the American Association of Railroads Procedure[15], and others. As a global test, it is complementary to other nondestructive examination methods which are used for follow-up inspection.

Acoustic Emission (AE) is an extremely useful tool for materials research. It is a highly sensitive technique for detecting active microscopic processes, as well as crack propagation. As such events give rise to elastic waves which propagate through the material, AE monitoring may be used to detect and locate the source of the waves and can inspect damage by using remote sensors, rather than requiring complete volumetric scanning. [2]

The usefulness of AE testing has been considerably enhanced in recent years by the incorporation of the microcomputer into AE instrumentation. Not only has the computer revolutionized the acquisition, recording and analysis of the large amount of data arising from an AE study but, above all, the combination of relevant hardware and software, together with careful mechanical procedures has succeeded in minimizing the problem of background noise. Thus AE has become a viable tool even in the noisy environment of the fatigue test.

Fatigue crack formation and initiation are generally preceded by progressive material deterioration, induced by dislocation motion and saturation, and a loss of resistance in terms of life. Monitoring this deterioration in real time allows the measured quantities to be used as indicators of the extent of fatigue damage.

Although the technology has been used extensively in the petroleum and chemical industries, it has had only limited application to bridges, cranes, and other civil engineering structures, even through its unique characteristic as a noninvasive global test makes it particularly valuable. AE can be used in conjunction with other conventional complementary nondestructive test and evaluation techniques, such as ultrasonic inspection or radiography, which can be used for follow-up local inspection in areas where the AE data suggests that a problem may lie.

All acoustic emission testing procedures are based upon a signal detection technique which ensures coverage of the entire item of equipment under test and thus specifications for equipment and sensor calibration, along with attenuation measurements, are included in all test procedures.

2.2 WAVE PROPAGATION THEORY

Wave propagation theory involves the study of fluctuations in the value of various mechanical quantities characterizing the state of matter – fluctuations of the pressure or other components of stress, or fluctuations of density, temperature, and the position of individual particles of a given material. Generally speaking, the science can be divided into two domains; primary measurement and secondary measurement. The former endeavors to determine the magnitude and waveform of the oscillations of one of these quantities at any given position in the body, whereas the goal of the latter is to characterize the propagation of these oscillations through the body by determining the speed of propagation, the intensity, or rate, of propagation of the energy, and the absorption rate of the energy. Acoustic Emission relies upon both primary and secondary parameters in the interpretation of experimental data.

Most of the early measurements used mechanical devices that would determine only the magnitude of the oscillation of displacement or velocity. The advent of electronic amplifiers led to the development of electro-mechanical transducers which convert the oscillating mechanical quantities into an electromotive force (EMF). This development is of particular significance in discussing the present subject as many AE instruments rely on amplified signals from piezoelectric pressure sensors mounted on the surface of the material being tested in order to collect valid data.

The piezoelectric sensors contain piezoelectric elements that develop an EMF in response to mechanical stress. In the pioneering days of the technology Rochelle salt crystals were used as the element, because of their high sensitivity. Present-day piezoelectric sensors generally use polarized ceramic piezoelectric elements of barium titanate, lead zirconate, or others which have high sensitivity, good durability, and are available in many the common shapes required for various sensor designs. A cross section of a typical AE sensor is shown in Figure 2.1.

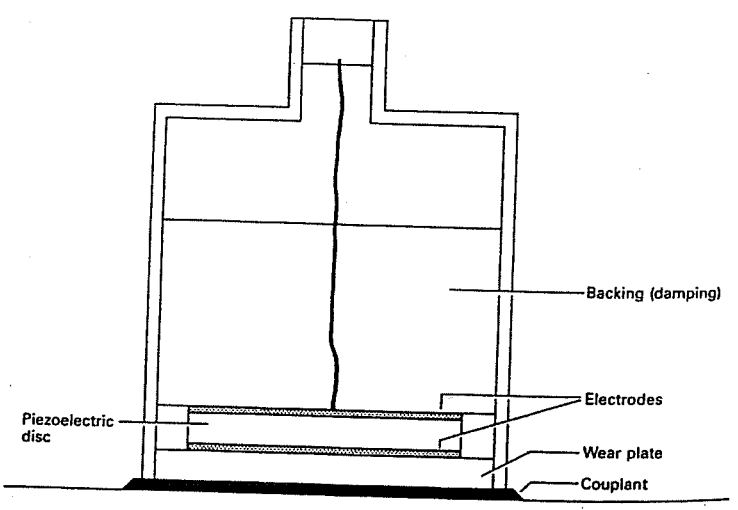

Figure 2.1: Cross Section of a Typical AE Sensor Coupled to an Object

The ratio of the generated EMF to the oscillating pressure generating the EMF is called the sensitivity of the sensor. The sensitivity is determined by a calibration procedure. Acoustic emission sensors are often calibrated so that one microbar of pressure on the sensor face causes one microvolt of output from the resonating crystal. Sensors which conform to these standards have proved to be effective and accurate in recording the acoustic energy generated from structural sources in a large variety of common engineering materials. Common resonance frequencies for AE sensors are on the order of 150 kHz through 300 kHz. Lower frequency measurements can be made, going as low as 5 kHz, using active transducers known as accelerometers. Among the most recent contributions to the field of AE is the wide band sensor, which, in essence, has no base resonating frequency - rather it is able to pick up and report the true frequency of the events taking place. Wide band sensors have an effective operating range between 50 kHz and 1.2 MHz. All certified AE sensors, though, are shipped with calibration curves which show their specific response to a given frequency pulse, as shown in Figure 2.2.

Measurements of the distribution of acoustic intensity around a sound source have become increasingly common place since the advent of digital spectrum analyzers. The intensity is a vector quantity whose component in a specified direction is the acoustic power passing through a unit cross section perpendicular to the specified direction, this being equal to the time average of the product of the instantaneous sound pressure and the instantaneous particle velocity component in that direction. With a digital spectrum analyzer, the intensity is usually measured by evaluating the cross-spectral density of the sound pressure at the sensor face; the spectral density of the intensity at any frequency can be shown to be proportional to the imaginary part of the cross-spectral density of the pressure at that frequency. This cross spectral technique is suitable for both narrow and wide bands. [4]

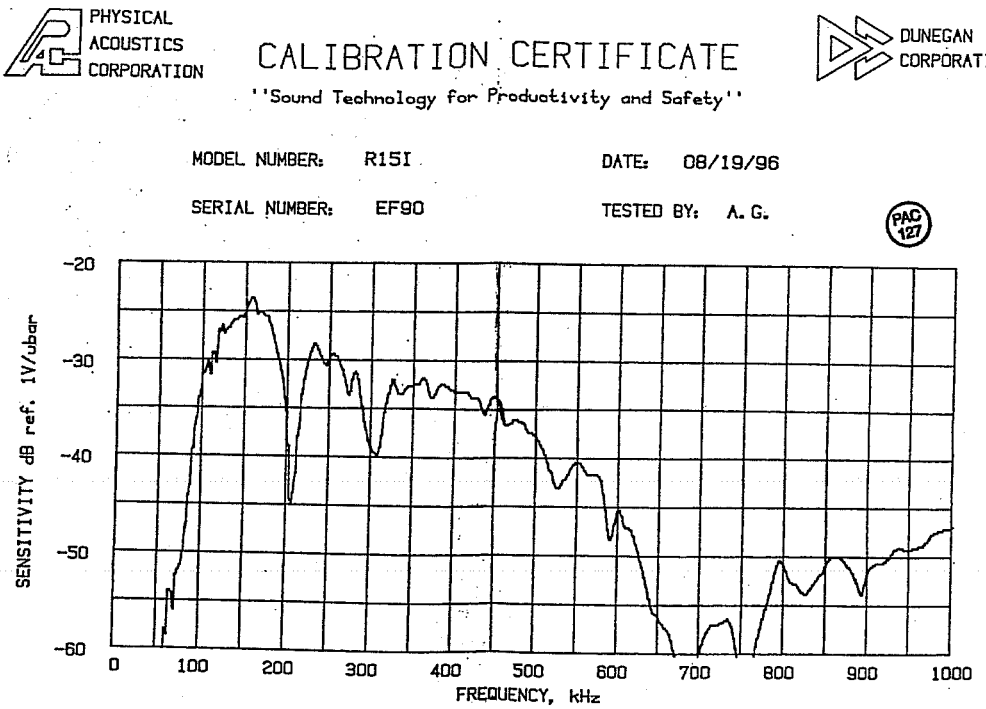

Figure 2.2: Typical AE Sensor Calibration Curve[3]

It is of much practical interest to understand some of the physical phenomena associated with acoustic wave propagation. Sound waves travel in solid materials by elastic deformation of the material, which as touched upon earlier, is called an elastic wave. In solid material, the shape of the wave changes, as it travels. This is due to the different frequency components traveling at different velocities.

The wave propagates undisturbed until it reaches some obstacle. The obstacle, which can be a heterogeneity in the material, or a physical object, distorts the sound wave is several ways. Pressure waves, as with light, are effected by reflection, refraction, diffraction, interfaces and scattering. Each is described briefly.

When a wave hits a rigid obstacle, or an air void, part of it bounces off the obstacle, a characteristic known as reflection. The reflection of the sound back toward the source is called an echo. The echo sound wave generally undergoes a phase transformation in the reflection process.

Refraction is the change of direction of a wave when in travels from one material into another where it has a different velocity. The following example explains refraction: Imagine a sound wave that is constant over a plane in a given material and a line drawn perpendicular to this plane (i.e., the normal) indicates the travel direction of the wave. When the wave travels to a different material, the normal bends, thus changing the direction of the sound wave. This normal line is called a ray. This process is shown schematically in Figure 2.3.

When a pressure wave hits an interface, part of the wave reflects and part goes through the interface. The part that goes through the interface is the transmitted wave. Reflection and transmission are related phenomena, which may be used to understand the nature of acoustic emission sources.

Diffraction is associated with the bending of sound waves around or over barriers. A sound wave can often be heard on the other side of a barrier even if the listener cannot see the source of the sound. However, the barrier projects a shadow, called the shadow zone, within which the sound cannot be heard. This phenomenon is similar to that of a light that is blocked by a barrier.

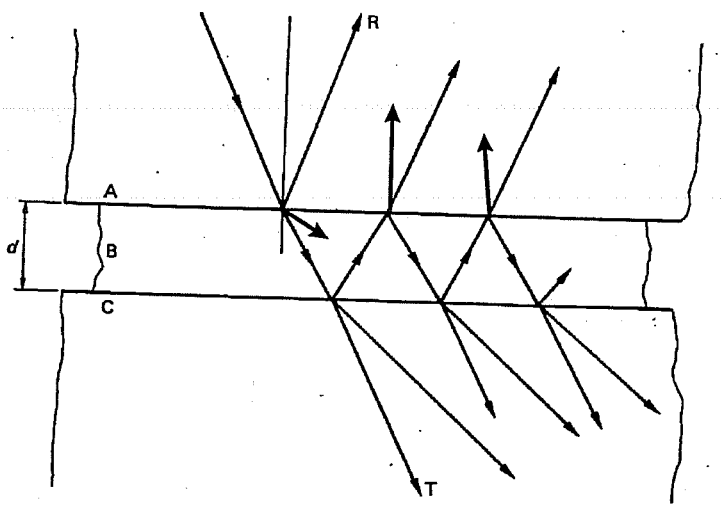

Wave refraction on an interface between two materials, A & C, with a coupling layer, B. T denotes the transmitted portion of the wave, and R the reflected portion.

Figure 2.3: Sound Wave Refraction

Interference is the phenomenon that occurs when two pressure waves converge. In linear wave theory the pressure waves can be superimposed. When this occurs, the resultant pressure wave is the sum of the two waves, taking into account the magnitude and the phase of each wave. Traditionally, however, logarithmic scales are used in measuring magnitudes, and thus the result of superimposing the crest of two waves would only be an increase of 6 dB.

Wave scattering is a related property to reflection and transmission. It is the phenomenon that occurs when a pressure wave goes around an obstacle and breaks up, producing a different pressure pattern around that obstacle. Although metals such as steel are, in a physical sense, homogeneous, obstacles such as air voids, weld inclusions, and hard grains are commonly encountered. The pressure travels off in all directions around the obstacle. The part of the wave that travels back toward the source is called the backscattered wave, and the wave that travels away from the source is known as the forward-scattered field.

A good working knowledge of these physical phenomena is important to be able to correctly interpret acoustic emission data. Although none of the parameters measured in AE testing specifically measures any of the described phenomena, all of the stress waves the sensors pick up are, in one way or another, related to these properties.

2.3 THE ACOUSTIC EMISSION SIGNAL

Through various mechanisms acoustic emission generated by a material defect propagates from the source within the solid body to the sensor, usually located on the surface, in a manner similar to earthquake waves traveling through the interior of the earth to the surface. As the signal travels, it is attenuated by the heretofore described physical phenomena. Generally speaking, high frequency components are attenuated more than low frequency components, and sensors located far away from the source receive only the low frequency components of the wave. The range of frequencies typically encountered in AE are on the order of 50 kHz to 500 kHz. Depending on the type of sensor used, and the type of information required, various filtering schemes have been developed for various purposes that can modify the signal received.

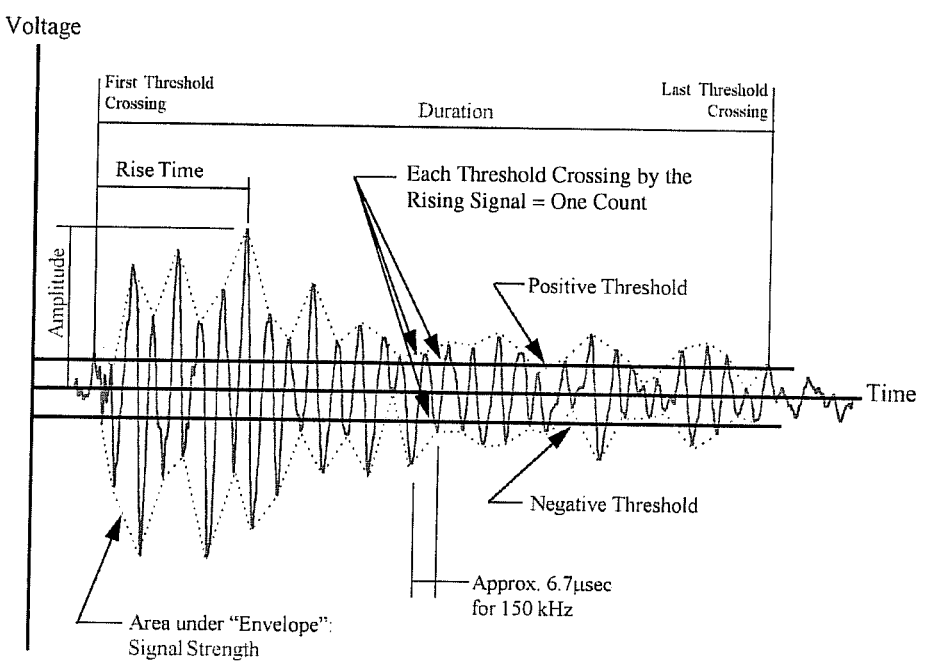

Figure 2.4: **Typical AE signal - Voltage VS Time - Showing definitions of Amplitude, Duration, Threshold, counts, and Rise Time.**

Figure 2.4 shows typical output from an AE sensor. When a stress wave strikes the face of the sensor, it causes the output signal to rise above a preset threshold. This signal is commonly referred to as a "hit". The threshold value will vary depending on the type of data required, and the circumstances of the test. It is used to selectively reject signals with amplitudes below the threshold which will not provide meaningful data, as they may be caused by spurious sources such as ambient, electronic, or electromagnetic noise.

Acoustic emission has been observed to occur in bursts, which manifests itself as a number of separate sensor hits within a short period of time. The cascade of hits is, in itself, very telling, as different cascade patterns are characteristic of different types of defects. It has been noted that emission bursts are similar to records of some earthquakes, but over a much shorter time period. The early hits are small in magnitude and foretell the main energy release. Hits occurring at the end of the bursts can be aftershocks, caused by smaller events due to the same phenomena which caused the original emission, and would generally be of much lower energy.

Although the waveform of the type presented in Figure 2.4 is a depiction of what the actual piezoelectric sensor would output, most modern acoustic emission instrumentation, uses the rectified signal, as depicted in Figure 2.5 to perform the required analysis. The area under this rectified signal envelope, or MARSE (Measured Area under the Rectified Signal Envelope), is a measure of the relative energy in the signal. In acoustic emission practice, this is sometimes used as the Signal Strength, even though it is approximating half the true signal strength. With fully digital instrumentation, such as that used in this research, the full waveform is recorded, and the user may calculate the energy without having to rectify the signal, if so desired.

Signal strength is an important parameter in assessing the validity of acoustic emission data, as the loss of high frequency components and a decrease in amplitude of the stress wave during travel causes an apparent longer low frequency signal for which the area under the envelope would have the same approximate area as the case before the wave had traveled.

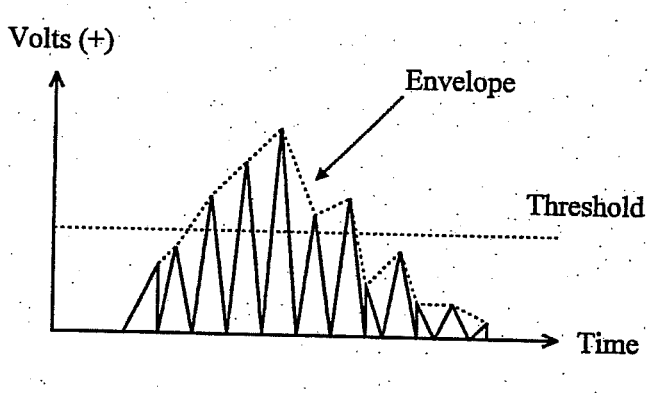

Figure 2.5: Depiction of a MARSE signal

The piezoelectric sensors require a preamplifier to overcome voltage losses between the sensor and the recording instrument. Some sensors have this preamplifier built into the sensor unit itself, whereas others require the use of an external device. The sensors which incorporate the preamplifier in themselves are preferred as there is less opportunity for spurious electronic or electromagnetic interference to contaminate the data. Generally, the preamplifier adds 40 dB to the amplitude of the signal. This 40 dB is usually subtracted out of the signal by the recording instrument before recording or displaying the data.

In order to assure an adequate acoustic bond between the solid body being tested and the sensor, some type of acoustic coupling compound must be used. For the present research hot melt glue was used to attach the sensor to the component being tested. The hot melt glue not only provided a good, strong, method of adhesion, but also proved to be an excellent acoustic coupling. As an alternative, a silicone based grease can be applied to the sensor face, and the sensor affixed to the component being tested by means of tape or spring loaded magnetic holddowns.

After attaching the sensors to the component to be tested, it is necessary to verify their correct operation. This is done by breaking a 0.3 mm 2H pencil lead in close proximity to each sensor on the surface of the solid body while monitoring with the AE equipment. The American Society for Testing of Materials (ASTM) outlines a procedure for doing this, which was adhered to at all times in order to assure scientifically admissible data (ASTM E1316 [18])

2.4 AE PARAMETERS

Well known AE parameters are used to understand the processes occurring within the crane shafts. Signal strength and amplitude are typically used together to provide a measure of the magnitude of typical events, such as material yielding in advance of the crack tip, or crack advancement, where a high parametric value is representative of significant damage within the material.

The arrival time of the signal is used for source location applications. If signals are captured by the required number of sensors located on the surface, the source of the emission can generally be localized. This is done in much the same way as an earthquake epicenter is located in seismology. Once the source has been identified, a detailed local inspection can be ordered to more clearly define the type and geometry of the defect.

The Kaiser effect is a powerful and important tool in the evaluation of acoustic emission data. The effect is defined as follows: if a material is stressed and monitored with AE, the stresses removed, and then reapplied, no acoustic emission occurs until the load reaches the level corresponding to the maximum load in the previous stage. This effect is seen in most metal and composite materials.

The Felicity effect is the breakdown of the Kaiser effect. It forms an important part of the evaluation criteria for new and in-service pressurized and atmospheric containment vessels. The Felicity ratio is defined as the ratio between the load at the onset of acoustic emission during a reload test and the maximum load applied to the element during the previous loading interval.[3] It has been shown that the Felicity ratio is related to the degree of deterioration or

damage of the element. A value very close to unity is characteristic of a material in good health, while smaller values (less than 1) are representative of the fact that damage has occurred.

The similarities between these two parameters arise from the fact that the Kaiser effect may well be represented as a special case of the Felicity ratio equal to unity. Figure 2.6 presents the Kaiser and Felicity effect, as obtained from a typical test. In this figure, the Kaiser effect may be noted in the second loading stage. The emission begins again just as the load reaches the maximum value attained at the end of the first loading.

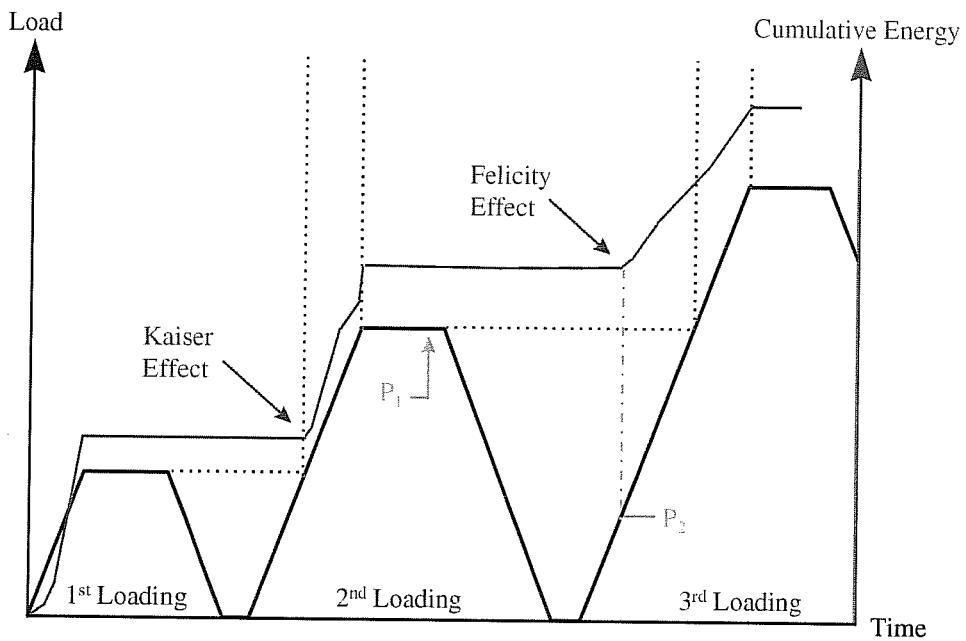

Figure 2.6: The Kaiser and Felicity Effects

The Felicity effect can be seen in the third loading, since the emission starts before the load reached the maximum value of the previous loading. For this case, the Felicity ration is P_2/P_1.

Another important technique in the evaluation of AE data is the Intensity analysis, which provides a measure of the structural significance of a defect. The two basic parameters used for this analysis are the Severity Index and the Historic Index. These indices are defined in section 12.6 of the proposed standardized testing procedure. Basically the indices are obtained from the cumulative signal strength of a series of events in a test, and give a good indication of the absolute magnitude as well as the change in the magnitude of the emission. The change in magnitude of the emission can, in turn, be related to the significance of the damage in a given structure.

2.5 AE AND FATIGUE CRACK GROWTH IN THE LITERATURE

The mechanisms that cause genuine AE in metals are discussed by Fang and Berkovitz[5], Heiple et al [6,7], and Williams [8]. While these authors all differ to some degree on precise definitions [such as nomenclature, description of the exact microscopic behavior, number of different mechanisms, and differentiation between mechanisms], all tend to agree on the following general classification schemes:

Gross Yielding. This is the most common mechanism of AE generation in metals. Heiple and Carpenter[7] provide a comprehensive summary of work done by many researchers in the 1970's and 1980's into the precise metallurgical processes [involving crystal lattice types of different metals, effects of grain boundaries, lattice twinning, microscopic inclusions, etc.]. The authors put forth that AE during yielding is due primarily to the movement of dislocations, which are imperfections in the crystal lattice. Since the energy from the motion of one dislocation is too small to be detected, there must be a progressive "unpinning" of many dislocations at once to cause detectable AE. That is, dislocations pile up at a microscopic obstruction, until the increasing stress causes one dislocation to begin to move, triggering an avalanche of dislocation movements.

Elastic Crack Growth. The energy released during the actual separation of the crack faces [by "either transgranular cleavage or intergranular fracture along the grain boundaries", according to Fang and Berkovitz[5]] causes high energy AE. This emission is fairly easy to distinguish, with very high amplitude and high signal strength hits. Most AE testing procedures [for example, the ASME Boiler and Pressure Vessel Code[8]] recognize this by treating any AE with an amplitude higher than 70 dB as evidence of the existence of cracks. Elastic crack growth is encountered more often in brittle materials, such as cast iron, or steels with a high carbon content.

Plastic, or Fatigue Crack Growth. The consensus of all the literature is that fatigue crack cracking does cause AE. Together, Heiple et al[6,7] and Fang and Berkovitz[5] describe four specific mechanisms of AE generation during fatigue crack growth, as shown in Figure 2.7. In roughly sequential order of formation, they are:

1. Dislocation movement [plastic flow] in the plastic zone, very similar to the yielding mechanisms described above [called Stage I by Fang and Berkovitz[5]];
2. Fracture/decohesion of inclusions in the plastic zone as the crack advances, also called crack nucleation or initiation [Stage II];
3. Crack advancement, similar to the elastic crack growth described previously [Stage III]; and
4. Crack face rubbing, also known as crack closure.

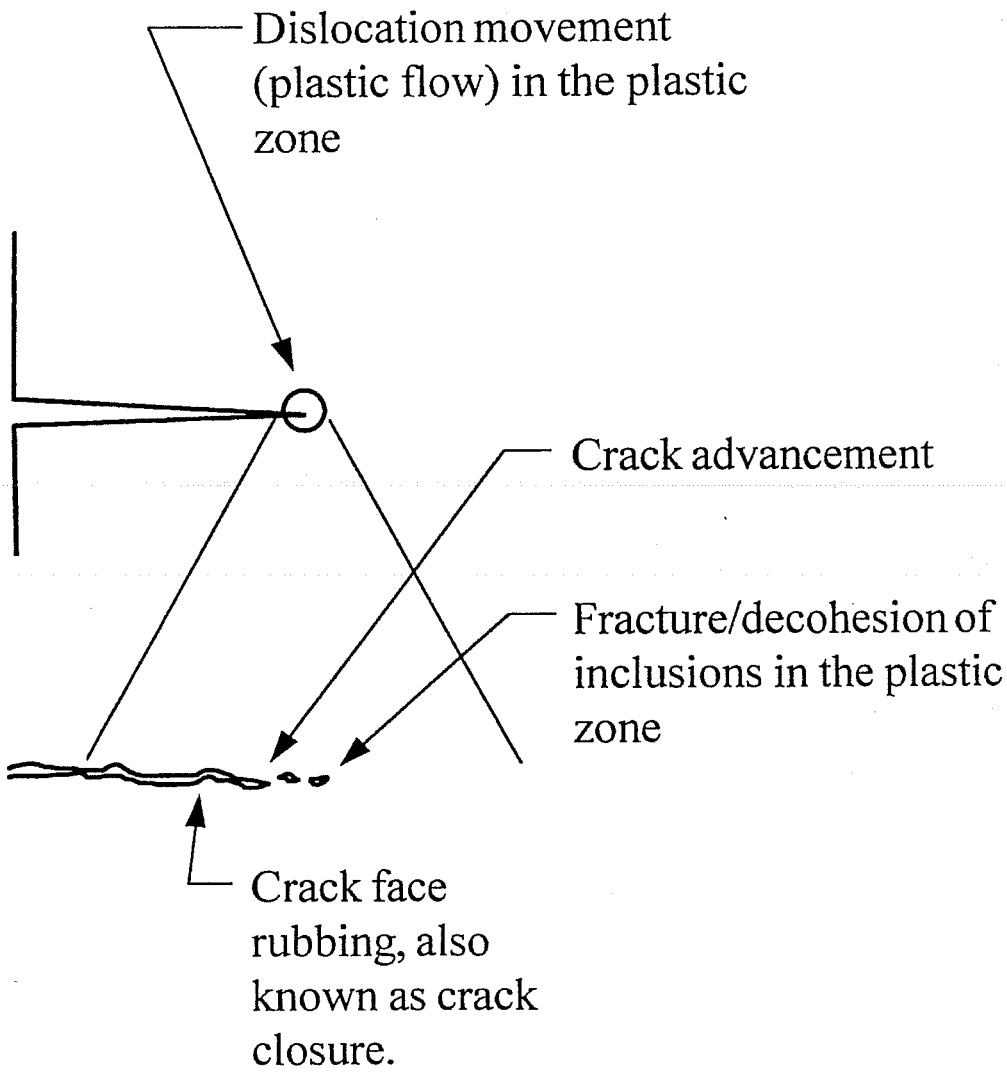

Figure 2.7: Causes of AE in Fatigue Cracks

These four mechanisms will all occur during fatigue crack growth. Each mechanism will create AE with different characteristics. At this time, there is no consistent, satisfactory way to determine which mechanism corresponds to each hit.

Fang and Berkovitz[5] performed tests on several unnotched tensile dogbone coupons machines from nickel alloys. Different specimens were tested with several different levels of maximum stress (σ_{max}), and different stress range types: tension-compression cycles $R = (\sigma_{min} \div \sigma_{max} = -1)$, tension-zero [approximately] cycles (R=0.01) and tension-tension cycles (R=0.2). In all cases of the low range of maximum stress investigated, the AE behavior

(after the first few cycles) was dependent only on the stress range $\Delta\sigma$. Figure 2.8 shows the behavior of cumulative AE counts, η (a common measure of cumulative AE in the 1970's and 1980's) versus time. Note the change in AE behavior during each of the three stages described in the forgoing discussion. The lower graph indicates that the slopes are a function of $\Delta\sigma$, but the general trend is the same for all the tests.

Williams[9] describes tests on mild steel pipes with an axial partial thickness slit. It can be seen that the experimentally observed behavior of the cumulative AE:

$$\frac{d\eta}{dN} = C_1 \Delta K^{m_1}$$

has a very similar form to the Paris law:

$$\frac{da}{dN} = C_2 \Delta K^{m_2}$$

where:

η is the cumulative AE counts,

a is the crack length,

N is the number of cycles,

ΔK is the range of K, and

C_1, C_2, m_1, m_2 are material constants.

Williams shows that for many cases, $m_1 = m_2$, leading to:

$$\frac{d\eta}{dN} \alpha \frac{da}{dN}$$

This means that AE during any period of time is proportional to the fatigue crack extension during that time. Although it was not done by Williams, this implies that might indeed be possible to calibrate AE to remaining fatigue life.

Whittaker[10] does exactly that. He describes tests performed on aluminum wedge-opening-loading specimens, which are fatgue-precracked. Whittaker analyzed the Felicity ratio from several different fatigue tests. The Felicity ratio (FR) for each cycle is defined by:

$$\text{FR} = \frac{\text{Load at Onset of AE During Current Cycle}}{\text{Maximum Load During Previous Cycle}}$$

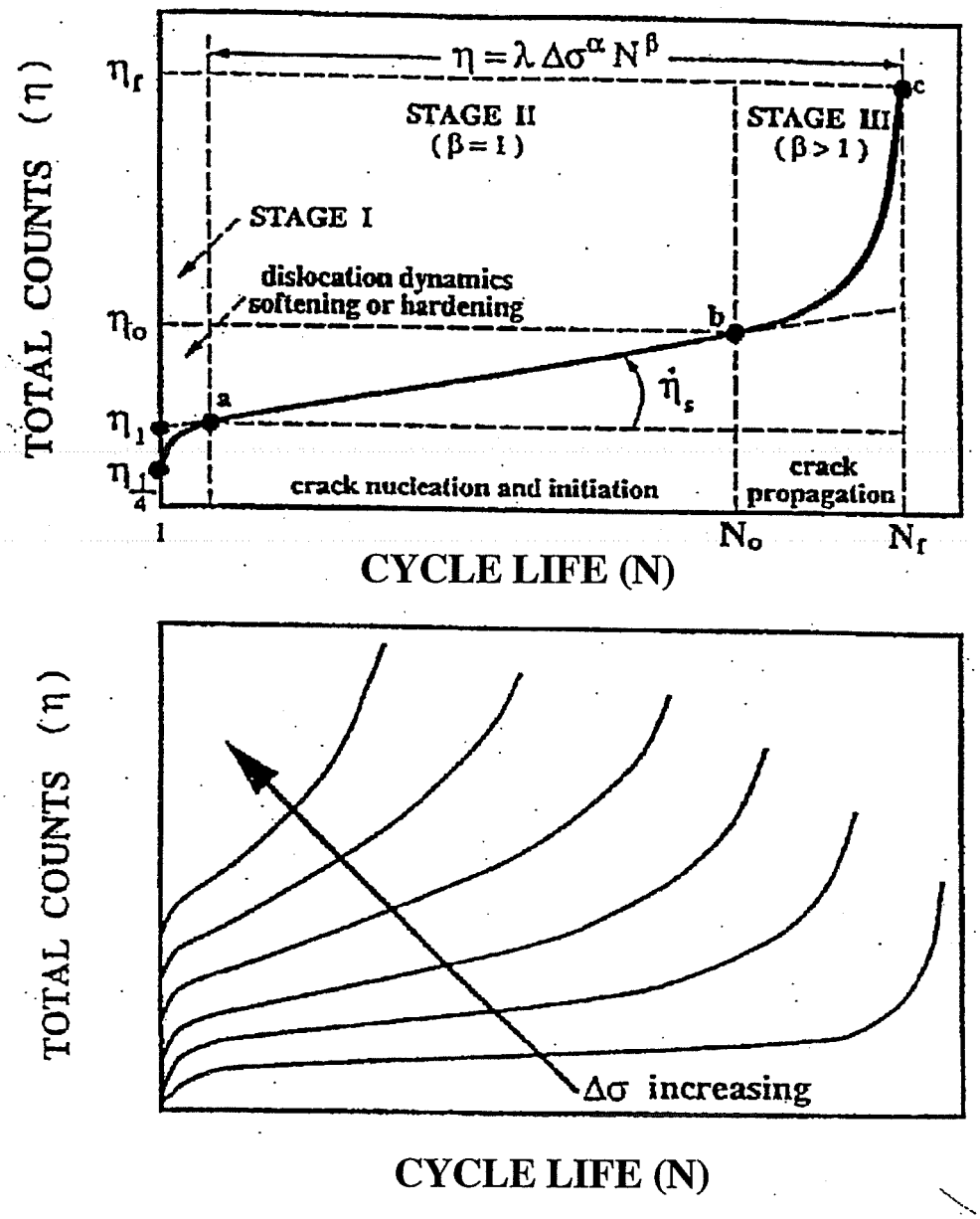

Figure 2.8: AE Behavior During a Fatigue Test

A Felicity ratio of 1.0 is an indication of an undamaged specimen. Felicity ratios lower than 1.0 indicate damaged specimens. As a specimen undergoes fatigue damage, it would be expected that the Felicity ratio would progressively drop. Whittaker's data shows a very good correlation between the Felicity ratio and the remaining fatigue life, as shown in Figure 2.9.

In light of experience gained during laboratory experimentation, the author feels that counts might not necessarily be a good measure for estimating fatigue life, but rather energy, or perhaps signal strength. By looking at counts, the relative magnitude (or intensity) of the hits are ignored. For this reason, as seen in Chapter 4, the analysis portion of this research uses the change in energy with respect to number of cycles as a primary evaluation tool.

Siedlaczek et al[11] take quite a different approach. Their work surrounded low cycle (i.e., high $\Delta\sigma$) fatigue tests of unnotched structural steel tensile dogbone coupons. During the first few cycles, significant AE was generated, likely due to localized plastic flow caused by high stresses at small imperfections. As the test proceeds, the AE quiets down. Siedlaczek attributes this to dislocation density saturation (when so many dislocations are present that there is no way for all the dislocations to move, much like a traffic jam). When crack growth is initiated, AE begins to increase again. It is theorized that as new crack surfaces are created, this allows dislocations to "escape" to the new free surface of the crack, permitting further crack growth.

The most common problem in AE monitoring of fatigue cracking is that AE from fatigue cracking is often masked by background noise. Researchers dealt with this problem in different ways Many of the researchers referenced used guard sensors. These are sensors placed near

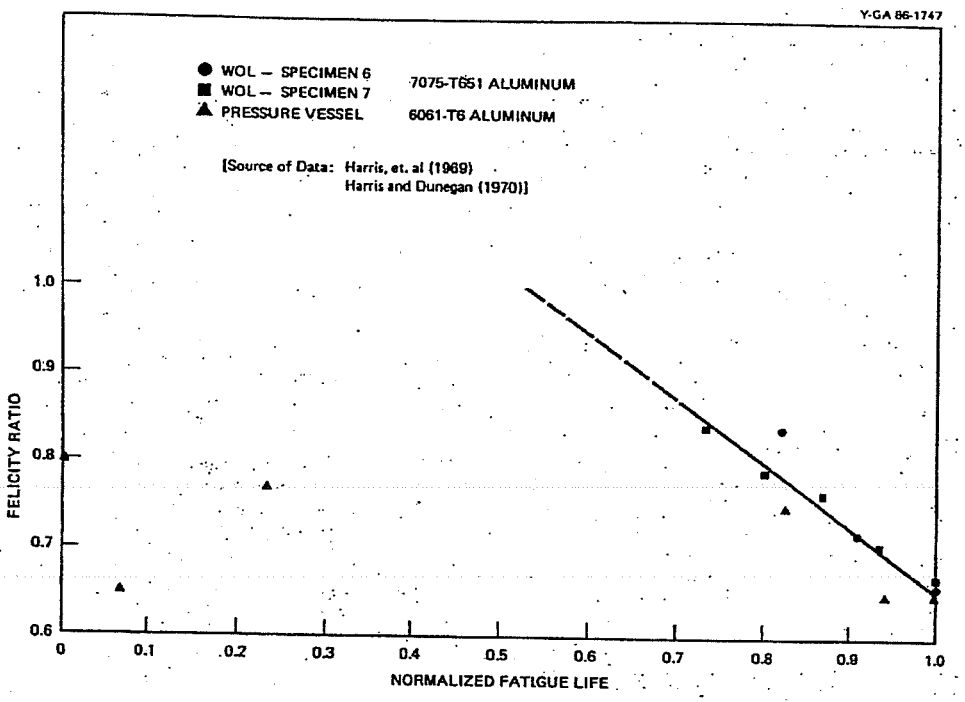

Figure 2.9: Correlation of Felicity Ratio to Fatigue Life

potential sources of background noise. When they are hit with AE before the other sensors, they lock out the instrumentation so no AE is collected for a short period of time. The use of guard sensors in field testing has been generally discredited since the late 1980's for all common AE test procedures, since it often removes genuine AE occurring about the same time as the background noise. It is, however, still used for materials research applications in the laboratory environment.

Almeida and Hill[12] report on tests of aluminum tensile coupons with rivets (a source of rubbing noise) and notched in the center to initiate fatigue cracks. They trained neural networks to differentiate between rubbing noise and fatigue cracks. Using source location software to check their results, they report that events which occurred at the crack tip were correctly classified as fatigue cracks 95% of the time.

Scala et al[13] describe tests on an aluminum bulkhead of an aircraft. They also reported that AE from fatigue cracking was drowned out by the background noise. They used fracture mechanics principles to determine the most likely location of fatigue crack initiation. They then placed AE sensors nearby, and used localized source location techniques to filter out any noise that did not originate from these regions. This approach also appeared to significantly improve the results.

2.3 STRESS AND FRACTURE MECHANICS ANALYSES

The failures observed by the Navy all initiated at the load transfer point in the shafts, at the key and keyway interface. A traditional stress analysis is very difficult owing to the complex geometry of system as well as the fact that the load is being transferred to the shaft by subjecting the key in both bearing and torsion, which in turn subjects the transfer point to a combination of stresses including a significant amount of shear. In order to gain a complete understanding of the stress and strain fields, a finite element analysis was performed on a model of the specific geometry.

The fracture mechanics analysis is equally, if not more difficult. Traditional stress concentration factors K_I (tension), K_{II} (shear), and K_{III} (torsion) needed for the fatigue life calculations cannot be calculated manually given the geometry of the load interface and the manner in which it is being loaded. The complex stress field and its interaction with each of the stress concentration factors is not at all resolvable using single parameter fracture mechanics tools. This is nowhere more evident than in the shafts themselves. The surface breaking cracks observed in the shafts started from the corner of the keyway, and the crack proceeded into the volume of the material toward the shoulder in a curved fashion. The curved nature of the crack shows that no single K factor can be used to estimate the effects of the phenomena observed to be taking place. Approaches using multiple K factors in an "interaction" equation have been proposed by Broek[14] but only work using highly idealized boundary condition and material assumptions, and in general do not appear to be widely applicable to the present research.

The most accurate estimation of fracture mechanics parameters needed to estimate fatigue life will result from an energy approach. Finite Element Analysis provides an effective means of integrating an energy approach of calculating the fracture mechanics parameters needed with any given geometry using the so called J- or Contour-Integral. This technique also allows the effects of metal plasticity to be incorporated into the analysis, which will ultimately result in a better understanding of what is actually taking place, along with an enhanced ability to predict future failures.

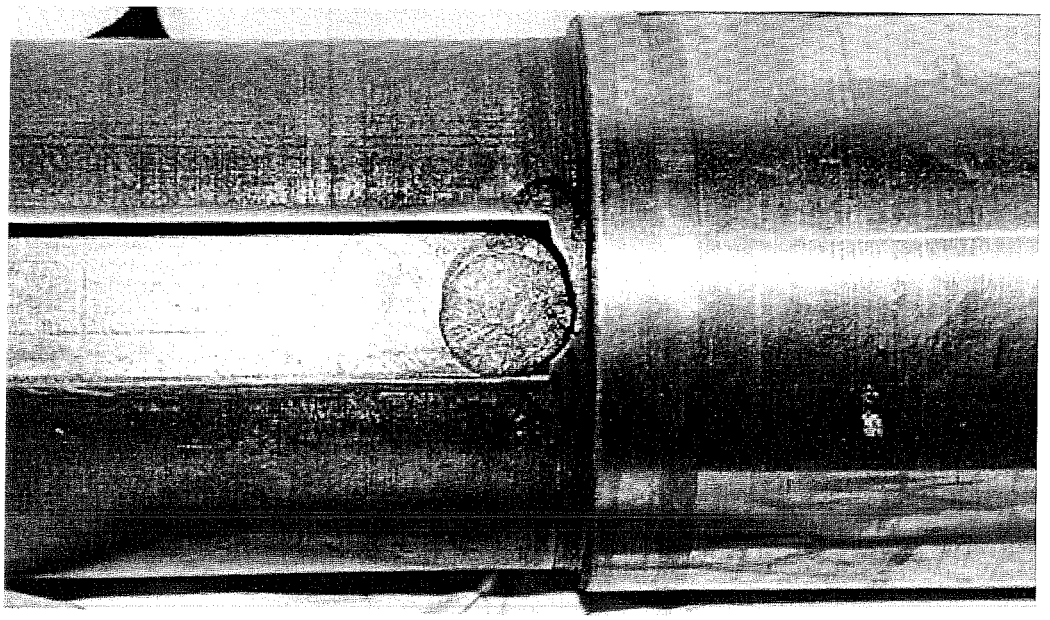

Figure 2.10: **Key and Keyway System. Note Square Corners at End of Keyway Which Were Designed to be Round - Much Higher Stress Concentrations Result.**

EXPERIMENTAL PROGRAM

3.1 GENERAL APPROACH

Two phases of laboratory testing were carried out at the Ferguson Structural Engineering Laboratory at the University of Texas at Austin. The laboratory testing afforded the opportunity to monitor the shafts under a variety of loading conditions in a controlled environment, and helped prepare for the field test that took place at the Pearl Harbor Naval Shipyard in Honolulu, Hawaii on a real Naval portal crane.

The purpose of the first phase of laboratory testing was to investigate the feasibility of using acoustic emission to find existing fatigue cracks in the crane shafts under static loading. The shafts were loaded in pure torsion, in a manner analogous to the way they would be loaded within the crane, and the acoustic emission generated was characterized. During this phase, background noise, test threshold, and acoustic attenuation were some of the parameters investigated to judge if the technology was suited to the application.

The second phase of testing incorporated and refined the results of the static loading phase with the goal of benchmarking AE from different size cracks and to learn if AE intensity increased as the crack grew and became more structurally significant. A secondary goal was to develop a better understanding
of the behavior and failure mechanism of the shafts under fatigue loading. The ultimate goal of the dynamic testing phase was to gain enough data and experience to write a standardized test procedure that could be used by the Navy's NDT personnel and contractors to examine and evaluate the crane shafts in-situ.

The knowledge and experience gained during both phases of testing was put to use during a field test at the Pearl Harbor Naval Shipyard in Honolulu, Hawaii in February 1997. The purpose of the field test was to demonstrate that the technology could be successfully used in a non-laboratory setting, as well as to validate and calibrate laboratory data for future field work. The field work provided an opportunity to evaluate the proposed standardized test procedure, and gave a good indication of the types of difficulties that would be encountered during future field testing, remedies for which were proposed in the final draft of the test procedure.

3.2 STATIC LOADING PHASE OF LABORATORY TESTING

3.2.1 Test Frame

The static testing phase of the present research was not carried out by the author. However, it will be discussed presently as an understanding of the first phase is critically important to an understanding of the subsequent work. A complete report detailing the first phase of testing, written by the original researchers, can be found in the reference [12].

The setup for the acoustic emission tests was intended to put the shaft specimen in pure torsion. The exact dimensions of the test frame were designed for the particular geometry of the specimen from crane P-68 at Pearl Harbor Naval Shipyard, a four foot long full axle. The frame was also designed to be easily expandable, so that future experiments on partial axles, different length specimens, and different loading combinations could be conducted. This first test, however, did not incorporate any effects other than pure torsion.

The loading system was designed to mimic the actual end support conditions of the axle found in the field. Thus, torsion was introduced by locking into a mechanical keyway, rather than welding a plate to the end of the axle. This also allowed for other nondestructive examination tests during and after the acoustic emission tests, with no change in the original axle.

The test setup is shown in Figures 3.1 and 3.2. The axle is placed horizontally in the frame. It is supported and loaded by two end blocks keyed into the front and back, which were specially machined to the dimensions of the axle. At the back end, the end block was sized so that it would lock between the flanges of a W12×40 steel column, and thus be restrained from rotating. The only other reaction at this end is a bearing-only connection onto a steel tube section below, with an elastomeric bearing pad. Therefore, this back end can resist torsion and the dead load of the specimen, but does not restrain the shaft with a bending moment.

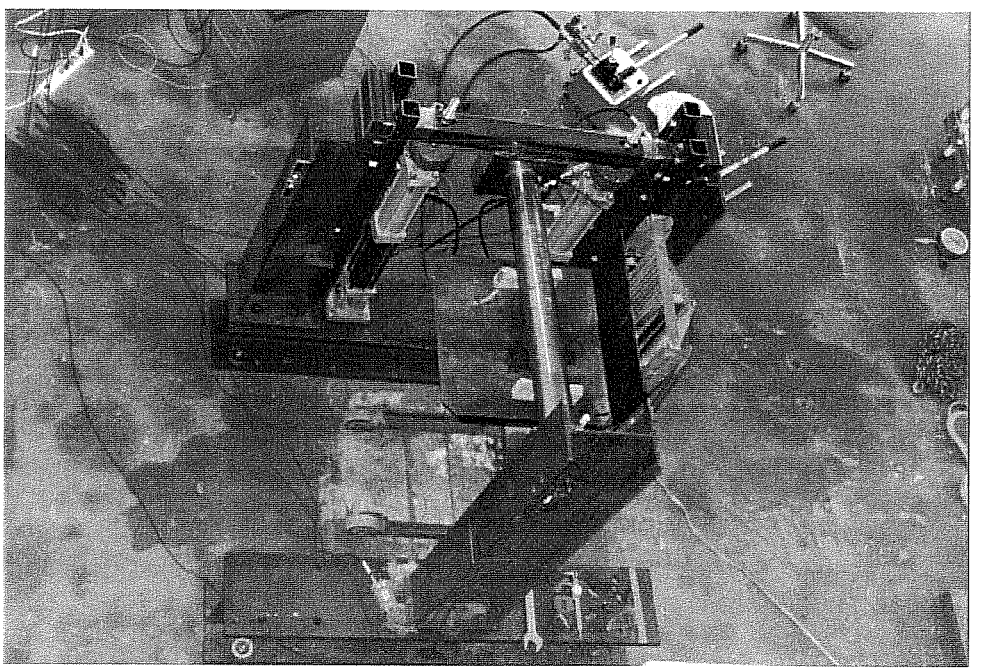

Figure 3.1: Test Setup During Static Loading Phase. View from Above.

The front end is also locked into an end block, but this end block is welded to a tubular steel arm that is supported on two reversible hydraulic rams. The rams are Model 10023 Double-Acting Hydraulic rams made by Shore Western Manufacturing. They have a maximum capacity of 50 kips. The rams are pressurized by two PowerTeam Series P460 two-speed hydraulic hand pumps, operated in unison by a single operator. The load in each ram was measured with load cells.

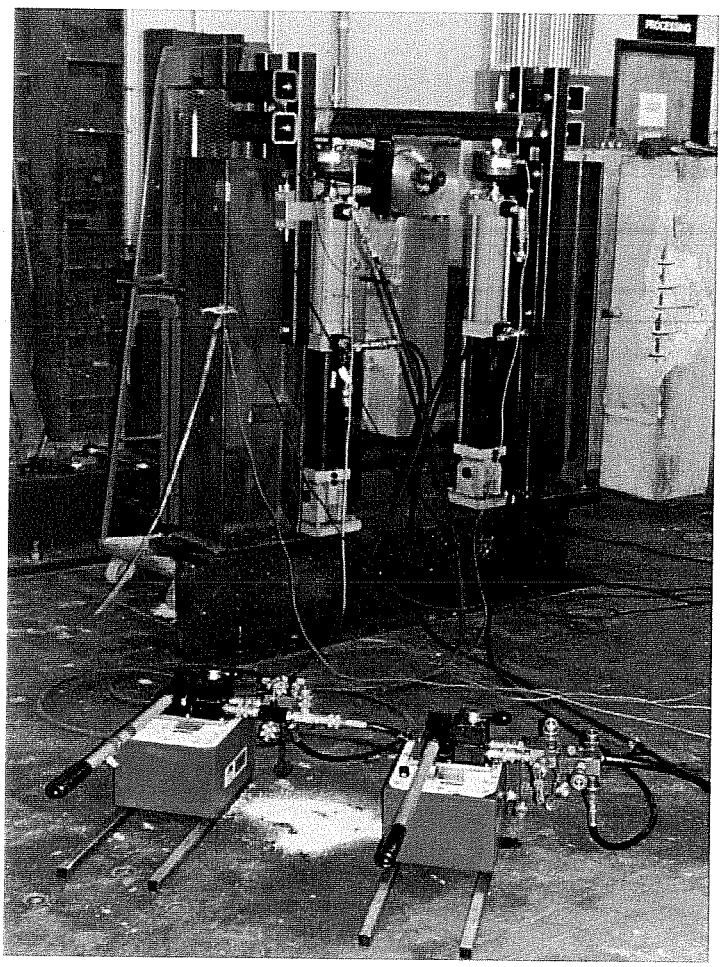

Figure 3.2: Loading End of Test Frame. View from Front End.

The steel tube at the front is "braced" with steel guides at each end to prevent out of plane rotation when the specimen is under high torsional loads. The braces are mounted to W12×40 columns, one on each side of the rams. All W12×40 columns and rams are bolted to frond and back W12×150 base beams, which in turn are bolted to a concrete reaction floor.

The test frame and rams were designed to apply a load of 200 in-kips of torsion to the specimen. This is twice the design load of 100 in-kips, which provides additional capacity to increase the loads past the design loads if desired, or to test different specimens in the future.

3.2.2 Loading

Examination of the free body diagram in Figure 3.3 clarifies how torsion is introduced into the specimen. Essentially, the torsion is introduced by putting one ram in tension and the other in an equal amount of compression. As one ram piston is slowly raised and the other is slowly lowered, statics requires the two forces to be equal and opposite. This force couple is resisted by the end blocks at the other end with the torsional load being transmitted through the specimen.

The test was setup so that the shaft could be subjected to both clockwise and counterclockwise torsion. Figure 3.3 shows the details of the loading scheme used. It may be observed that the torsional loads were applied in the clockwise and counterclockwise directions in turn, with a maximum load of 50 in-kips, one half of the design load.

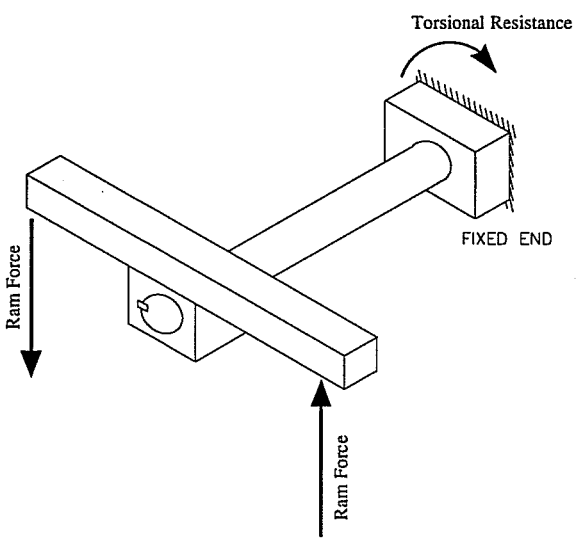

Figure 3.3: Loading Scheme Used During Static Loading Phase

The load was applied in a series of steps with intermediate load holds. Clockwise and counterclockwise (when viewed from the front of the stand) loads were alternated. This loading scheme was chosen to allow analysis of loading data, load hold data, and the Felicity effect. Loading was performed over a number of days rather than the 5,000 seconds shown in Figures 3.4 and 3.5. For purposes of analysis and display, however, the periods between tests

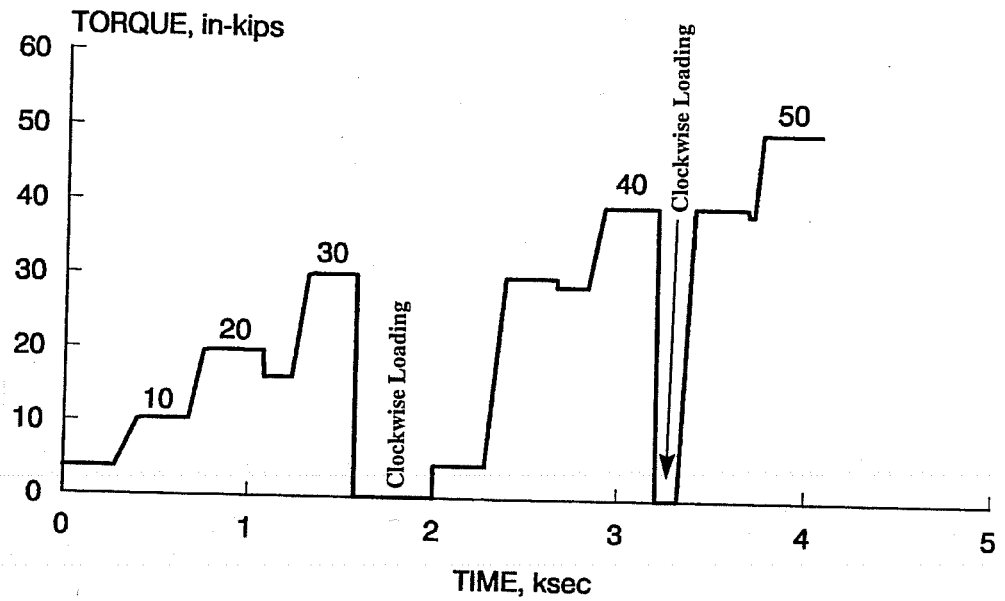

Note: For display purposes, time periods for clockwise loading... etc. have been shortened and are shown as periods of zero load.

Figure 3.5: Static Counterclockwise Loading

3.2.3 Instrumentation

Two acoustic emission instruments were used to acquire data. The first, shown in Figure 3.6, is a two-channel LOCAN AT instrument, manufactured by Physical Acoustics Corporation (PAC). It is an analog instrument, with an Intel 8 MHz 8086 CPU. Sensors were R15I resonant sensors (resonant at 150 kHz), also manufactured by PAC. The sensors, thresholds, gains, and other settings for this instrument were set to match those common in the acoustic emission field testing industry. These settings are detailed in Table 3.1.

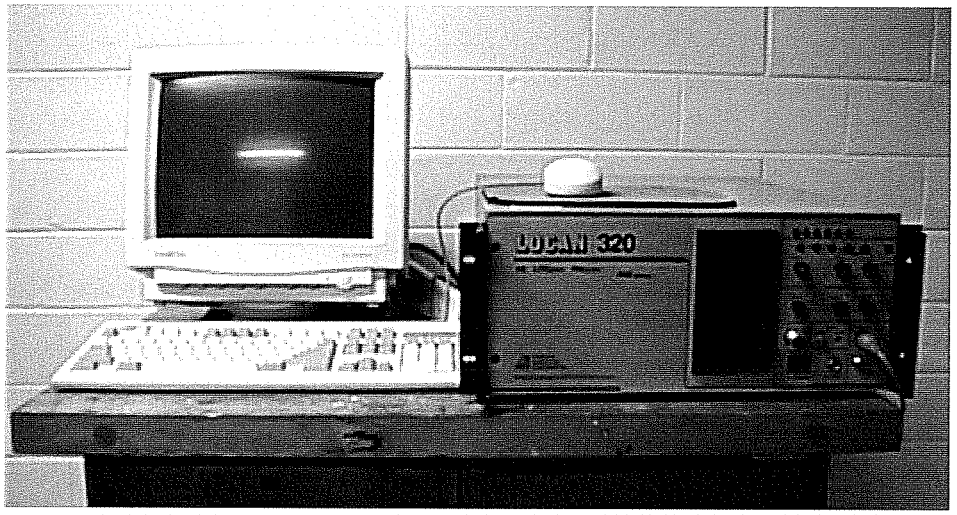

Figure 3.6: LOCAN AT Analog Acoustic Emission Instrument

The other instrument was a four-channel MISTRAS-2001, shown in Figure 3.7, also manufactured by PAC. This is a digital instrument, based on an 166 MHz Intel Pentium CPU system, and capable of recording and saving the digitized waveform of each signal it reads. In this test, acoustic emission data was sampled every 500 nanoseconds. This system was connected to several different types of sensors, to investigate the effect different sensors had on the signal received. Again, thresholds, gains, and other settings for this instrument were set to match those common in the acoustic emission field testing industry, and where possible the same as used on the LOCAN AT. These settings as well, are detailed in Table 3.1.

Figure 3.7: MISTRAS-2001 Digital Acoustic Emission Instrument

At the front, an S9208 broadband sensor was used. At the rear, a very low frequency RA2 accelerometer with a resonant frequency of 20 kHz was used. In addition, R30I resonant sensors (300 kHz) were used front and back. These high frequency sensors were used to take advantage of the greater attenuation of high frequency signals to reduce the number of reflections in this relatively small specimen. The R15I and R30I sensors had integral preamplifiers with 40 dB gain. Separate preamplifiers, set for 40 dB gain, were used for the RA2 accelerometer and S9208 sensor. The sensor layout used is shown in Figure 3.8.

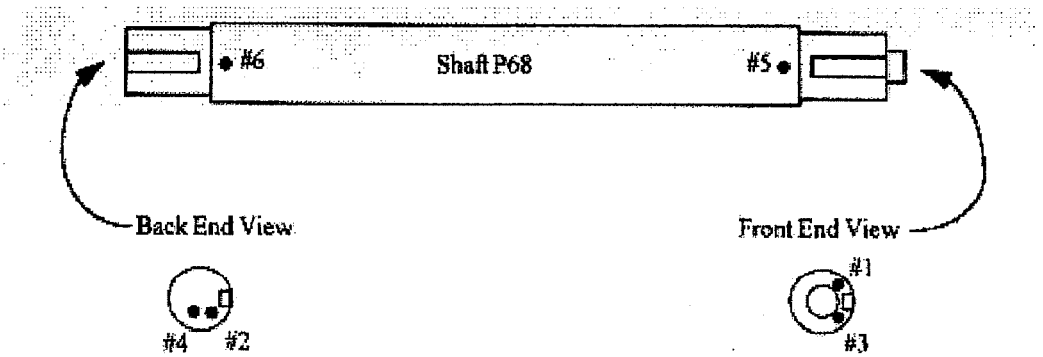

Channel	Instrument	Sensor Designation	Sensor Type
1	MISTRAS	S9208	Broad Band
2	MISTRAS	RA2	Low Freq. Resonant
3	MISTRAS	R30I	High Freq. Resonant
4	MISTRAS	R30I	High Freq. Resonant
5	LOCAN	R15I	Standard Resonant
6	LOCAN	R15I	Standard Resonant

Figure 3.8: Sensor Placement on Shaft

Table 3.1: Instrument Settings Used During Testing

Setting	*20 & 150 kHz Sensors*	*300 kHz & S9208 Sensors*
Threshold	45 dB	45 dB
Sample Rate*	4 MHz	8 MHz
Pre-Trigger*	20 µsec	20 µsec
Hit Length*	1000 µsec	1000 µsec
Peak Definition Time *(RTTO)*	200 µsec	200 µsec
Hit Definition Time	400 µsec	400 µsec
Hit Length Time*	1000 µsec	1000 µsec

* Only used with Digital Instrument

The sensors were attached to the shaft using hot melt glue. Before testing commenced, pencil lead breaks were performed next to each sensor, as set out by ASTM E1316, to ensure the acoustic coupling was adequate, and that the sensor was functioning properly.

3.2.4 Summary of Results

The exact details of the data and analysis methods used can be found in the reference[12]. The following is a summary of the results and conclusions reached in Phase I, as they pertain to the second phase of testing:

1. Acoustic emission can be used to detect fatigue cracks in crane shafts. Defects were detected in the crane shaft from Naval Portal Crane P-68.
2. A major structural defect, probably a fatigue crack, was detected at the back end of the shaft.
3. A less significant structural defect was detected at the front end of the shaft. It is probable that this defect is also a crack.
4. Both indications were detectable at a small percentage of the design load.
5. The indications were active under clockwise loading. Significant activity was also observed under counterclockwise loading. It is probable that this activity is due to reverse compression yielding at the tip of the crack.
6. 150 kHz sensors are sensitive to the emission and can be used for testing crane shafts. Emission was readily detectable at thresholds commonly employed in field testing.
7. In the event of background noise, 300 kHz sensors will provide adequate coverage of the crane shafts.
8. The Jolly-Stuart zonal source location technique makes it possible to distinguish which end of the shaft is the source of the emission.
9. The test frame can be used to test a range of crane shafts. Background noise from the loading frame and movement of the shaft and keyway was insignificant.
10. There is a high probability of success that a practical field test procedure can be developed.

3.3 Dynamic Loading Phase of Laboratory Testing

3.3.1 Test Frame

For the dynamic testing phase, the test frame had to be extensively modified. While it was originally thought that the frame could be used in the exact form it was in during the static testing phase, initial trials showed that modifications had to be made.

An automated control system consisting of an MTS 407 Programmable Electronic Controller and a MTS 293 Hydraulic Manifold was used in place of the hand pumps previously connected to the rams. These are shown in Figure 3.9. The controller and hydraulic system allowed for the load to be cycled at any given rate. The system was under load control, with feedback from load cells in the rams governing the amount of load applied. The electronic controller passed the load level through an output which was in turn used as a parametric input for the acoustic emission instrumentation.

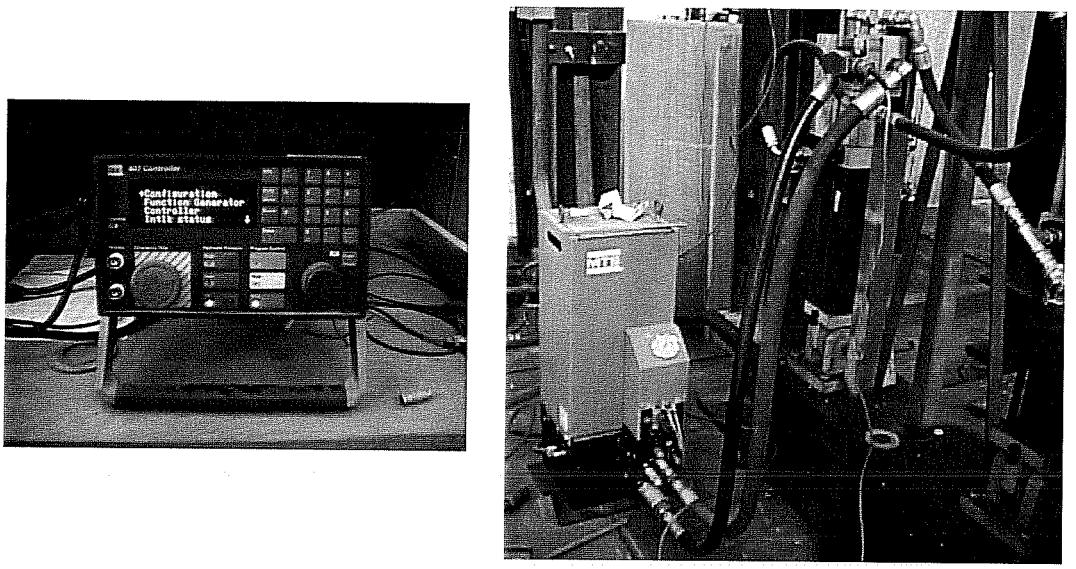

Figure 3.9: MTS Automated Controls Systems, as implemented

During initial trials it was found that there was too much play between the shaft and frame, and the frame itself was not stiff enough under the rapidly applied cyclic loads. One of the main problems was the way the back end of the shaft was restrained. From the foregoing description of the static loading phase setup it was established that the end blocks at the back end of the shaft transferred the torsional load to the floor by doubly bearing on the flanges of wide flanged rolled section, and transferred its dead load by using a slender column member. While this setup was perfectly adequate for the case of the shaft being loaded and unloaded slowly, when attempted with any speed, much movement and associated noise was observed. To remedy the problem, a frame at the back end of the shaft was setup to resist the torsional load. In essence, the end blocks were welded to a cross beam which was in turn welded to two stub columns. The setup was similar to that at the front end of the frame, except the stub columns replaced the loading rams to resist the load rather than apply it. The new restraint system was much stiffer, and also served to carry both the torsional load and the gravity load to the reaction floor below. The modified frame is shown in Figure 3.10.

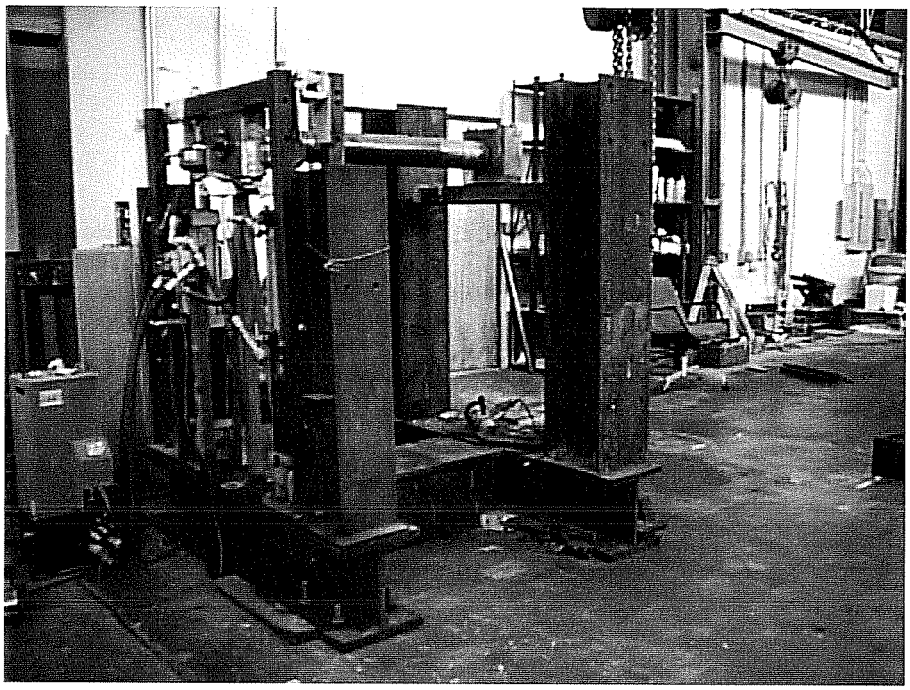

Figure 3.10: Test Frame Modified for Dynamic Loading

Background noise during the dynamic loading was much more of a problem than during the static loading. Rapid movement of the loading rams, shaking of the frame, and movement within the key and keyway system all contributed to the problem. As much of the noise as possible was removed, however, in many cases this was impossible, and a scheme to acoustically isolate the shaft from the remainder of the test frame was adopted. Teflon pads were placed at all metal to metal contact points, as shown in Figure 3.11. Additionally, the existing key was replaced with a new, tight fitting one to minimize movement during load reversal.

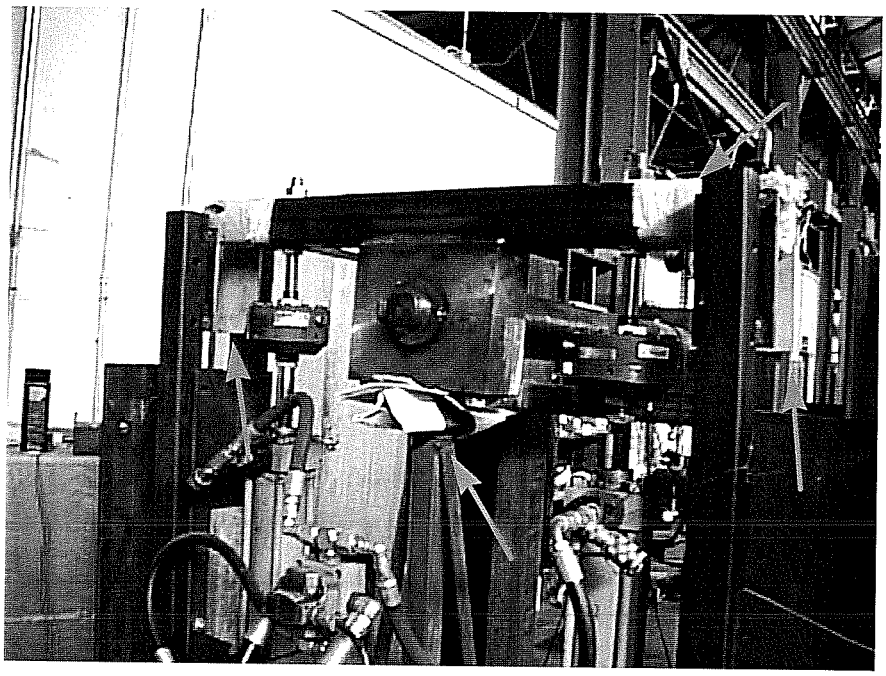

Figure 3.11: Teflon pads were applied to acoustically insulate the shaft from the frame.

3.3.2 Loading

Loading of the shaft consisted of 4,500 cycles at each load level starting at 40 in-kips working up to 100 in-kips in increments of 5 in-kips. A 10% overload was applied every 1,500 cycles. Additionally, a single overload cycle of 150 in-kips was applied at the end of the testing regime. The loading envelope is shown in Figure 3.12.

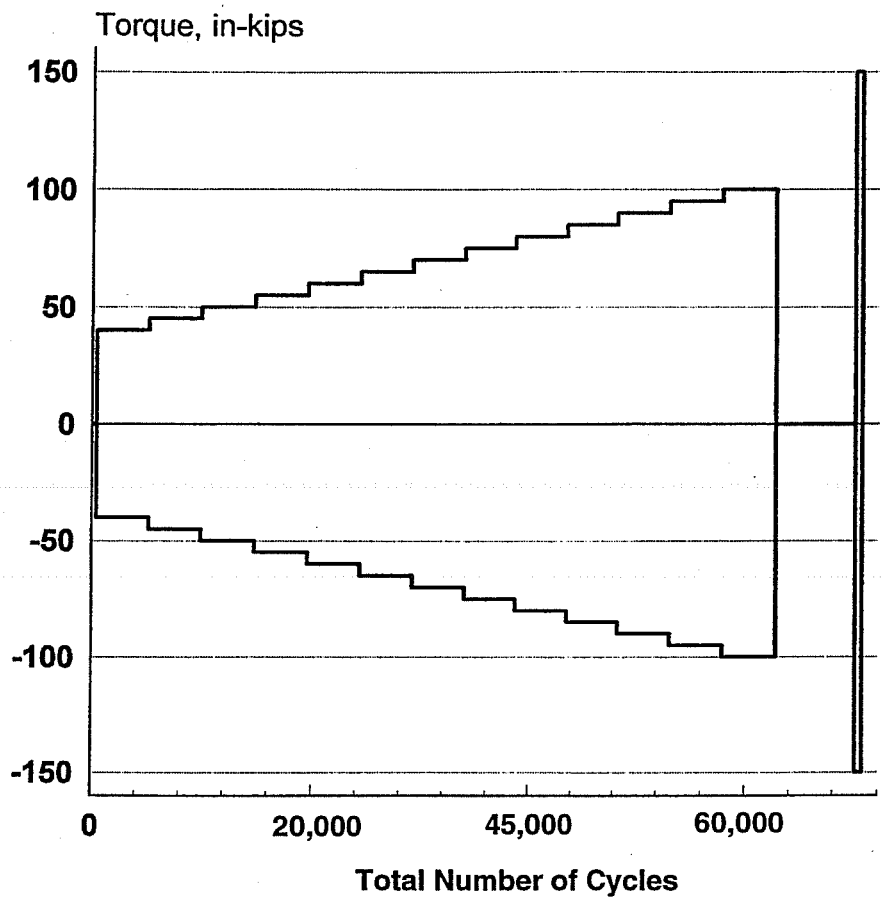

Figure 3.12: Loading Envelope used During Dynamic Testing Phase

Cycling took place at a rate of 0.17 Hz, or six cycles per minute with continuous AE monitoring. The MTS control system was programmed for a square waveform, thus incorporating a load hold at the peak positive and peak negative load during each cycle. A typical load history is shown in Figure 3.13.

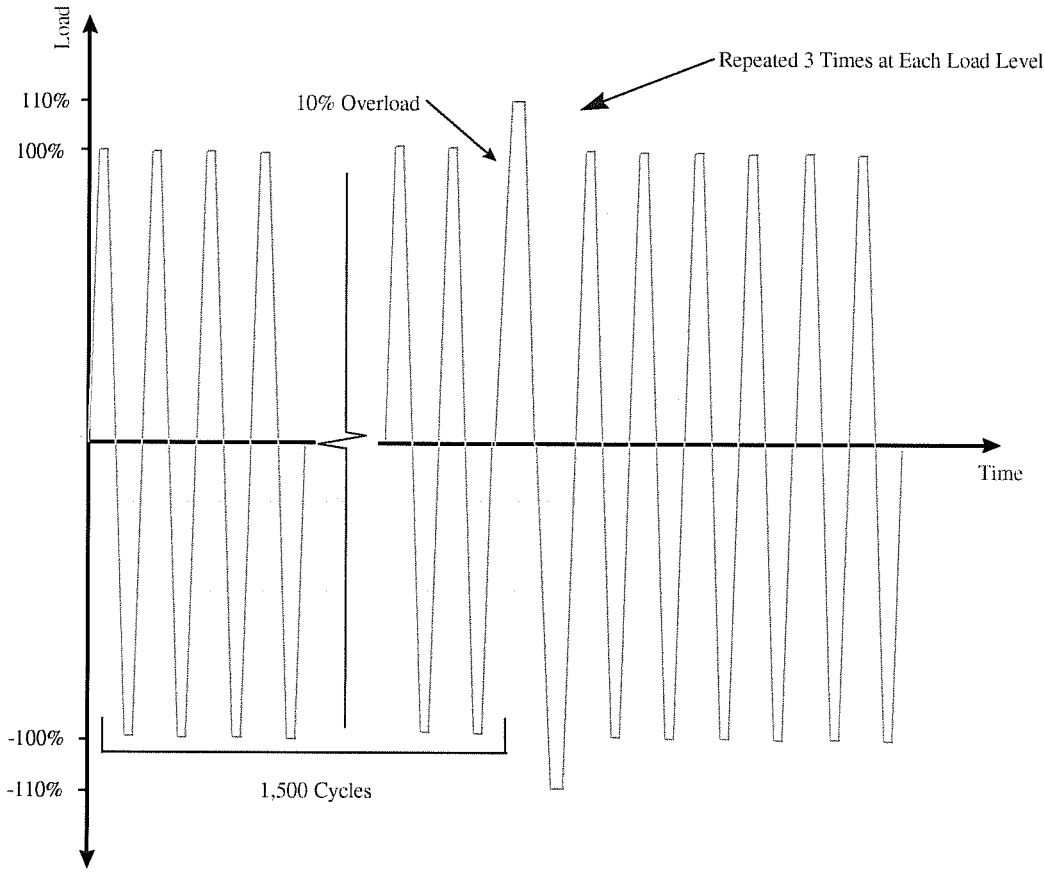

Figure 3.13: Typical Loading Scheme During Fatigue Cycling

Overloads of 10% of the fatigue load were manually applied every 1,500 cycles. The purpose of the overload was to obtain AE data from an overload of a growing crack. This provided data for the standardized test procedure and calibration of the acceptance criteria and intensity plots. The overload was applied by manually adjusting the set point of the rams using the control knob on the MTS 407 Digital Controller. As can be observed in Figure 3.12, the load is applied extremely rapidly when the automated square waveform is used. For the overload cycles it was felt that a slow application of the load was better suited to the purpose, as the Felicity effect and other load based parameters could be more accurately ascertained. Additionally, applying the load slowly further minimized the amount of frame borne background noise originating from the rapid movement of hydraulic fluid into and out of the rams, and the subsequent vibration in the stand. The slow loading rate is how the load is applied in the field tests, as well. Because of the higher load being used and the relatively small number of times the shaft was subjected to an overload at each fatigue load level a load hold of 90 seconds was used. An idealized Load vs. Time graph for the overload cycles is shown in Figure 3.14. AE monitoring was done throughout the entire cycle.

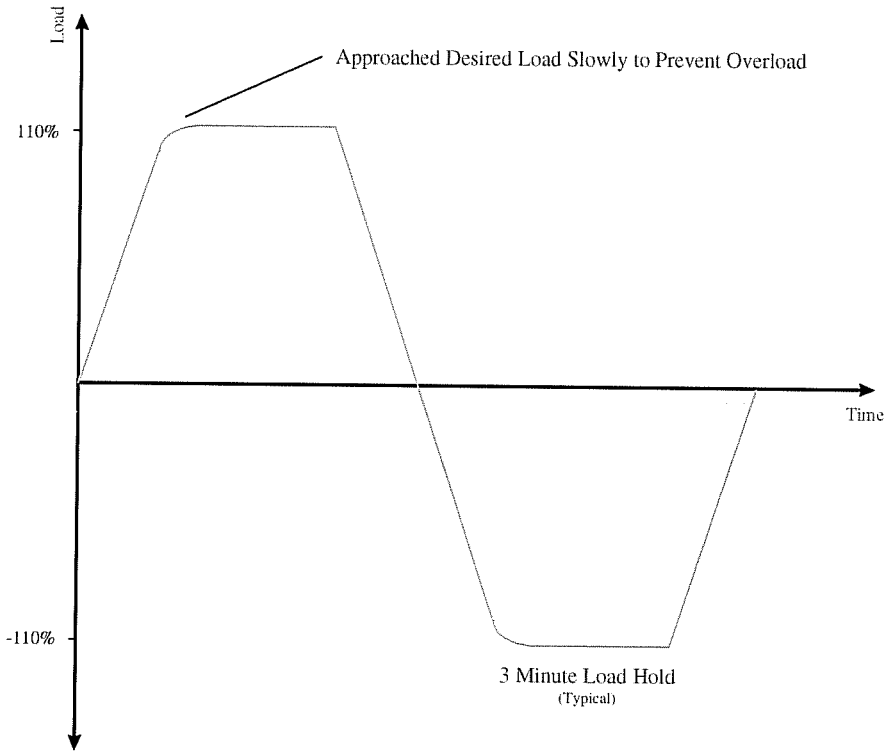

Figure 3.14: Load vs. Time for an Overload Cycle

3.3.3 Instrumentation

In the dynamic testing phase a six channel MISTRAS-2001 digital acoustic emission instrument was used to acquire data. The initial promise shown when using the four channel digital instrument during the first phase of testing played a large role in the decision to go exclusively digital. Another reason supporting the use of the digital instrument is that it could emulate the traditional analog instrument (i.e., not capture waveforms) but the converse cannot be said. The instrument settings described in Table 3.1 were used again during the second phase of testing, however the sensor types and thresholds used were optimized based on the initial trials which showed problems with noise due to the inherently more noisy environment of dynamic fatigue testing, and other problems experienced with the RA2 accelerometer and S9208 broadband sensor during the static loading phase of experimentation.

The first phase of testing showed that the 150 kHz and 300 kHz integral resonant sensors captured all the data of interest. Based on this fact, and previous negative experiences with broadband sensors and accelerometers in terms of sensitivity and background noise, the

choice was made to use exclusively the R15I and R30I sensors. Another factor in this decision was that the data being collected in the lab during the dynamic testing phase was to be used in preparing for an actual field test, and the writing of a field test procedure. A majority of field testing procedures use the 150 kHz and 300 kHz resonant sensors, exclusively.

A placement scheme was developed based on pencil lead breaks as shown in Figure 3.15 and Figure 3.16. Sensors are placed at each end of the shaft at the shoulder region near the end of the keyway. Placing the sensors only at the end of the shaft is consistent with all of the observed failures in the field, which started at the end of the keyway. The edge spacing of the sensors from the shoulder was incorporated to prevent loss of data due to the shadow zone created by the geometry of the shoulder. In order to assure full acoustic coverage of the region of interest, the sensors around the circumference were mounted 120° from each other, as shown in Figure 3.16. Another factor in choosing the mounting scheme was the ability to implement it in the field. The shaft ends are rarely accessible when the shaft is mounted in the crane, and thus the additional flexibility afforded by having the sensors some distance back from the shoulder help to make the technique more widely applicable in the field.

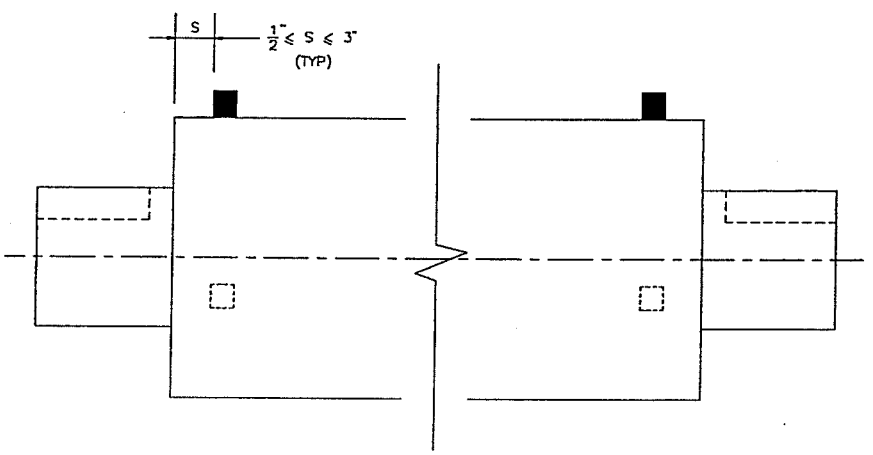

Figure 3.15: Sensor Placement Along the Length of the Shaft

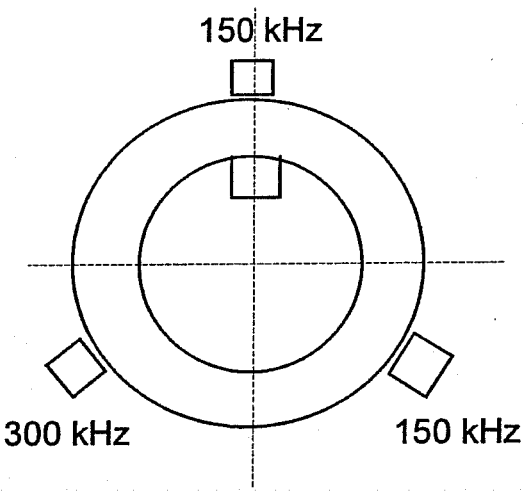

Figure 3.16: Circumferential Sensor Mounting Schematic

The sensors were attached to the shaft using a thin layer of hot melt glue, as was the case during the static loading phase. Before the sensors were attached, the area where the sensor would be mounted was thoroughly cleaned of all rust and debris, especially greasy residues. This was accomplished by means of sanding the surface of the shaft lightly with fine grained sandpaper, and then wiping the area with a paper towel wetted with an environmentally acceptable degreasing solvent, then allowed to air dry. Figures 3.17 and 3.18 show the sensors mounted on the shaft in the laboratory.

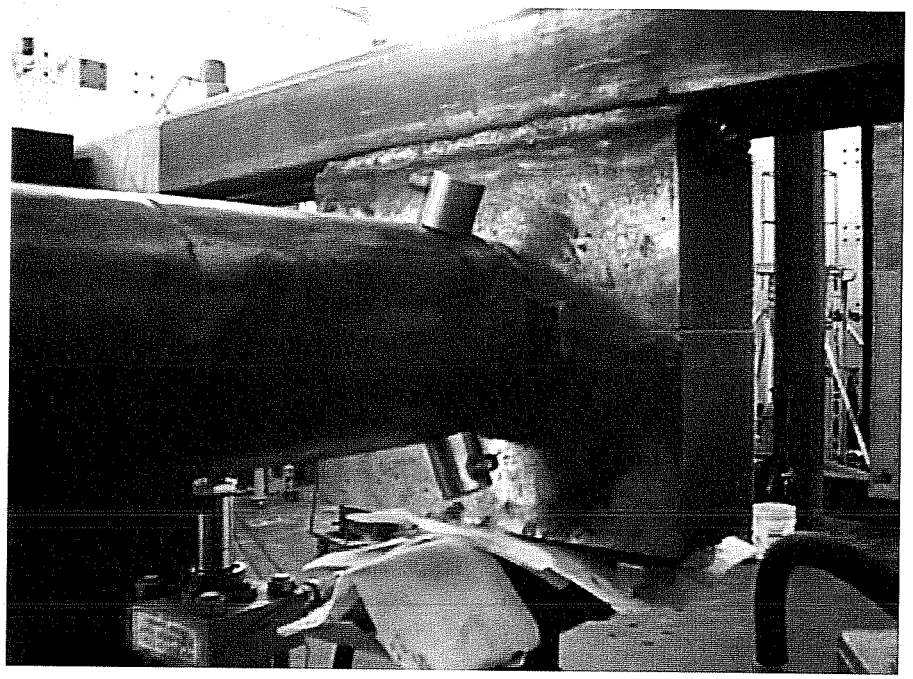

Figure 3.17: Mounted Sensors at Front of Shaft

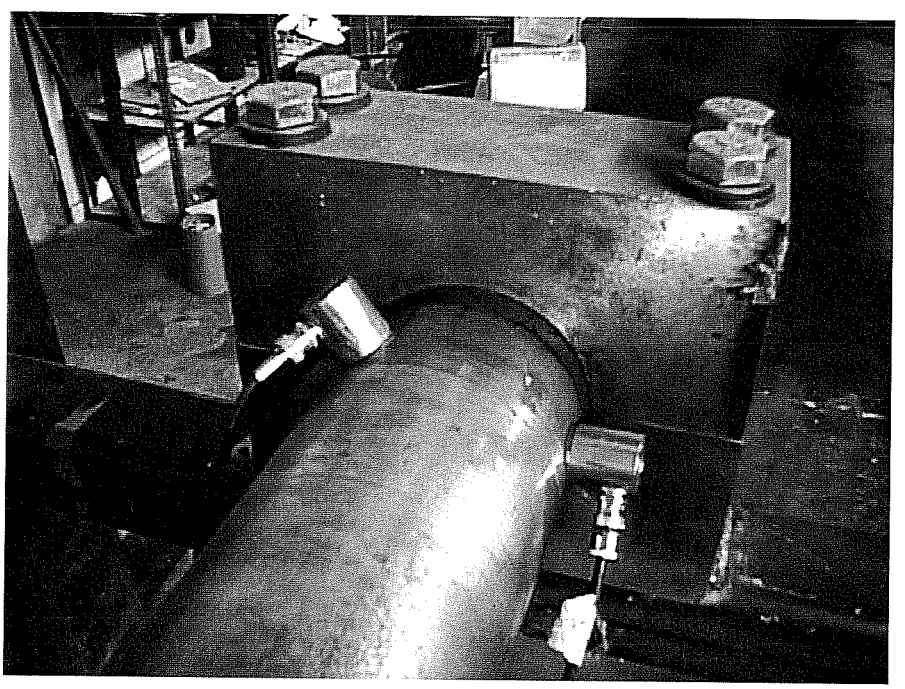

Figure 3.18: Mounted Sensors at Rear of Shaft

Following standard ASTM procedure, pencil lead breaks were performed adjacent to each sensors to ensure that each sensor was adequately coupled, attached and functioning properly. This procedure ensured that the hot melt glue was not too thick, and that the full sensor face was in contact with the shaft. As a matter of interest, pencil lead breaks were performed down the length of the shaft in increments of approximately 6 inches in order to attempt to characterize the acoustic properties of the shaft. Lead breaks performed anywhere on the length of the shaft were picked up by all sensors, with varying amplitude, confirming that attenuation was not a problem and emission anywhere in the shaft would be picked by at least one of the sensors.

3.3.4 Testing

Tests were conducted on a different rotate pinion shaft than was used during the static loading phase of testing. The rotate pinion drive shaft used for the dynamic testing phase was taken from crane P-66 at the Pearl Harbor Naval Shipyard. It was taken out of service during maintenance when the same shaft in its sister crane, P-65, was found to be cracked. Navy NDT personnel were unable to ascertain precisely if the shaft in crane P-66 was at all damaged using conventional nondestructive examination techniques.

Testing took place over the period of January through October, 1997. Much of the first few months were devoted to modifying the test frame and preparing for the field test at the Pearl Harbor Naval Shipyard.

Both fatigue loading and overloading were monitored; in total over 60,000 cycles. The immense amount of data generated was stored on the computers hard disk drive, and routinely burned onto compact disc for subsequent analysis, and long term storage.

3.4 THE FIELD TEST

3.4.1 Background

An acoustic emission test was conducted on crane number P-64, a Meyerstein 50 ton portal crane. The crane had recently been pulled from service due to a vibration problem detected by the operator during main hoist drum motion under load. A sister crane, P-63, was also pulled from duty at the same time. In-situ ultrasonic testing indicated the presence of cracks in the crane shafts, but this result was not confirmed my magnetic particle inspection. Shafts were removed from P-63 and sectioned, but cracks were not found.

Pearl Harbor Naval Shipyard has many cranes, of which only a small handful are currently in service – the remaining cranes are in need of maintenance or repair. The Navy was interested in returning crane P-64 to duty, but first needed to determine if the crane was safe to operate.

In previous tests conducted by the Navy, vibration sensors were mounted on the main hoist shaft face and drive gearbox. Vibrations were detected, and the vibration frequency matched the meshing frequency of the drive gear. The vibrations were observed during

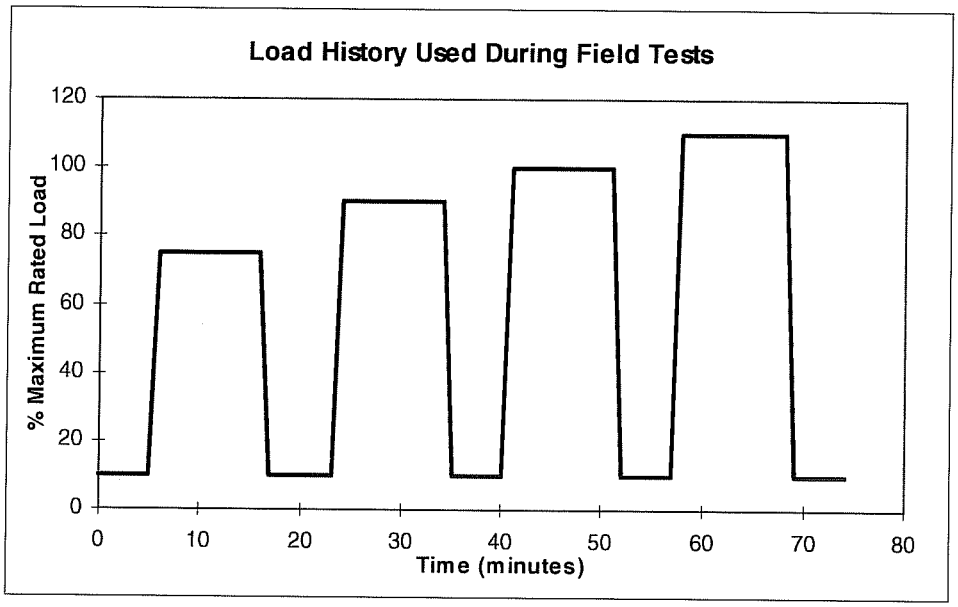

Figure 3.19: Load History used for Field Tests

3.4.3 Loading Strategy

To avoid the complication of shaft (and AE sensors) movement during testing, the main hoist was connected to a 126,000 lb. assembly of certified weights. It was originally intended that this load would exceed the amount of load to be applied during testing, and thus would never be physically lifted. This was the case during the testing of the main hoist shafts. The load load was applied by "booming up", or attaching the main hoist to the weights and raising the boom to apply load. Thus, the main hoist shafts did not move significantly during the main hoist shaft tests.

During the boom hoist shaft tests, the load cell failed during the execution of the load schedule. This failure was probably due to a short in the cable that ran from the load cell to the crane cab - the cable broke at one end after the test was complete.

Failure of the load cell left the crane operator "blind" with respect to the amount of load being applied. The entire load of certified weights was thus lifted completely off the ground, causing the crane to experience higher loads than had been planned. This unforeseen event did have some advantages:

1. The crane probably have never lifted a load this large - this load exceeded the maximum annual certification load of 100% = 55 long tons = 123,200 pounds. AE testing is most effective if the test article has not experienced the load in recent history.
2. Because certified loads were lifted completely off the ground, the final maximum load was well established even though the load cell failed.

3.4.4 Main Hoist Shaft AE Test

During the first test, the main hoist drive shaft and the main hoist drum shaft were instrumented with AE sensors, and AE data was collected continuously throughout the execution of the load schedule. During this test, the boom was held at minimum radius. According to engineers at the shipyard, this reduced the load experienced by the boom hoist to 50% of the value that would occur if the boom were held at maximum radius. This was carried out because acoustic emission is in a sense a "one time" occurrence, and the best data is collected when the structure under study is experiencing a load larger than any loads lifted during its recent load history. Thus, the boom could be set to maximum radius during the evaluation the boom shafts, and the boom drive and drum shafts would see a higher maximum load than they did during the main hoist test.

3.4.5 Boom Hoist Shaft AE Test

During this test, the boom was extended to maximum radius, and the boom drive shaft and drum shaft were instrumented with AE sensors, These sensors were monitored continuously throughout the load schedule.

Loads were applied to the boom by applying force to the main hoist cable, which was attached to the 126,000 pound load. In this manner, a load could be applied to the boom without moving the boom drum or drive shafts.

3.4.6 Advantages and Disadvantages of the Loading Schemes

The primary advantages of the loading schemes used in the two tests were:

1. The shafts under test did not rotate, thus avoiding problems with sensor cables running to the sensors attached to the shaft.
2. It was possible to bring the main hoist to maximum load while experiencing only a 50% maximum load on the boom hoist.

Disadvantages included:

1. It required a long time to complete the tests, since the load schedule had to be repeated twice.
2. The drum shafts were not rotated. They experienced a unidirectional bending moment where the ends of the drum meet the shaft, as the cable tends to "lift" the drum free of its mounts (bearings at each end of the shaft).

This situation raised concern that the drum shafts were not completely tested. Since the bending moment was applied in only one direction, it was feared that a crack might be in compression, thus not providing a detectable AE signal. This was a valid concern, and required careful consideration, and a refined method of loading the shaft, as can be found in the

proposed standardized testing procedure. The following is a summary of some of the important information:

1. As the main hoist and drum shafts rotate during the raising and lowering of loads, the bending moment load is applied over the full 360° of shaft rotation. This should encourage radially symmetric crack initiation sites that are equally dispersed in all radial directions. This type of crack growth has been seen to be responsible for sudden catastrophic failures, and is well documented in Navy reports. [1]
2. Note that the boom shafts are different from the main hoist shafts, which rotates during the raising and lowering of loads. Boom shafts only move when the boom is raised or lowered. The boom may experience more frequent loading at the particular drum and drive shaft orientations associated with maximum and minimum boom angle, or some other angle preferred by a particular crane operator.
3. Acoustic emission is most commonly associated with cracks under tension. However, AE can be generated during compression by compression yielding, crack closure, or crack face rubbing.

3.4.7 Instrumentation

During the first test, AE sensors were placed on the main hoist drum shaft and the main hoist drive shaft. In the second test, the sensors were mounted in the same manner on the boom hoist drum and drive shafts. The layout of the sensors is shown schematically in Figures 3.20 and 3.21.

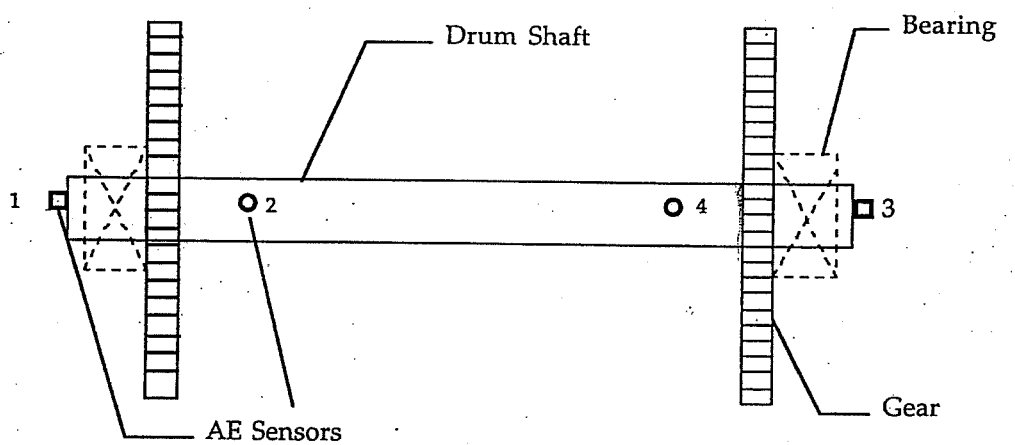

Figure 3.20: Schematic Layout of AE Sensors on the Drum Shaft

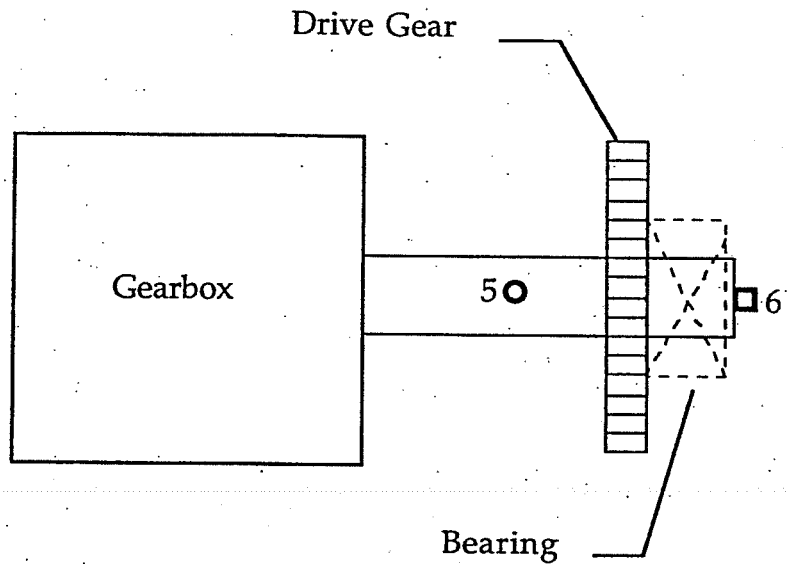

Figure 3.21: Schematic Layout of AE Sensors on the Drive Shaft

The sensor type and placement in Figures 3.20 and 3.21 was as follows:

Type:

Numbers 1, 3 and 5: Broad Band Sensors
Numbers 2, 4 and 6: 150 kHz Resonant Sensors

Location:

Numbers 1, 3 and 6: Located on shaft ends
Number 2: Located 18" from nearby drum shaft end (main host test)
Number 4: Located 15" from nearby drum shaft end (main hoist test)
Number 5: Located 21" from end of drive shaft (main hoist test)
Number 2: Located 16" from nearby drum shaft end (boom hoist test)
Number 4: Located 19" from nearby drum shaft end (boom hoist test)
Number 5: Located 16" from end of drive shaft (boom hoist test)

All six sensors were monitored using the PAC MISTRAS digital AE monitoring equipment.

3.4.8 Sensor Mounting

Once the location for an AE sensor was determined, files and sandpaper were used to remove the paint and reveal the bare metal of the crane shaft. The exposed metal was then

cleaned with environmentally acceptable grease solvents to achieve the cleanest possible surface.

Hot melt glue was used to attach the sensors to the crane shafts. It has the advantage of quick set, and can be removed easily using bare hands. However, there is some evidence to suggest that care must be taken when using this type of glue. After initial sensor placement and preliminary lead break tests, two sensors on the main spool shaft were found to be improperly coupled, and were thus remounted. These sensors had been mounted the night before and seem to have lost some coupling overnight. After remounting these two sensors, another preliminary pencil lead breaks series was conducted and it was discovered that, in the process of reattaching these sensors, a brush against one of the sensors caused by the limited maneuvering room in the crane machinery room caused another sensor to come unattached. This sensor was also remounted and the pencil lead breaks were performed again. Afterwards, all sensors met the required parameters, so the final pencil lead breaks, PAC pulser, and Dunegan cracker procedures (see section 3.4.12) could be performed. Figures 3.22 through 3.25 show some typical mounting techniques used while in the field. Note, in some of the photographs shown in Figures 3.22 through 3.25 two sensors are shown where only one is indicated on the schematics in Figures 3.20 and 3.21. This is because multiple sensors types were tested, although only one sensor was used at a time during data collection.

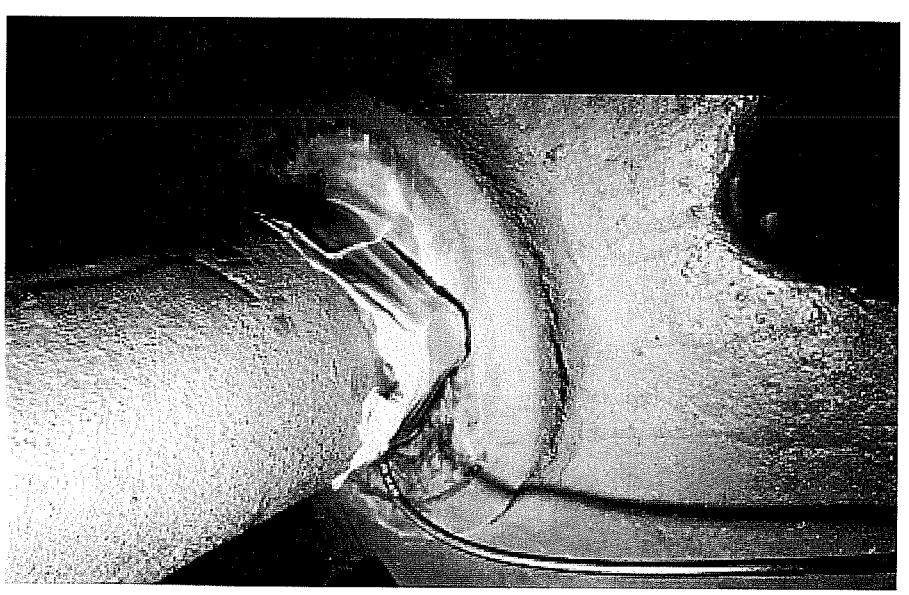

Figure 3.22: Sensor Attached to Main Hoist Drive Shaft and Secured with Duct Tape In Case of Inadvertent Shaft Rotation

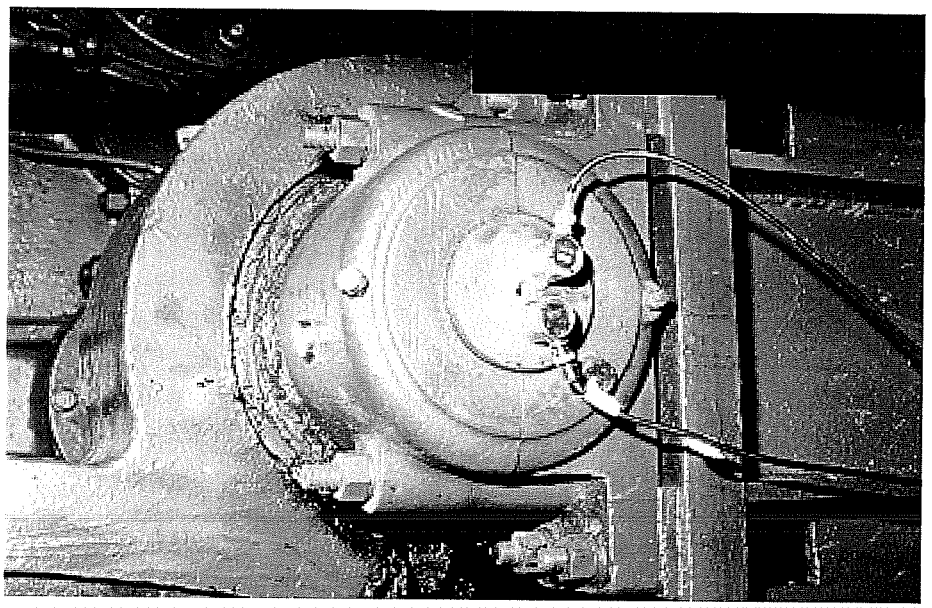

Figure 3.23: Sensors Attached to Exposed End of Boom Hoist Drum Shaft

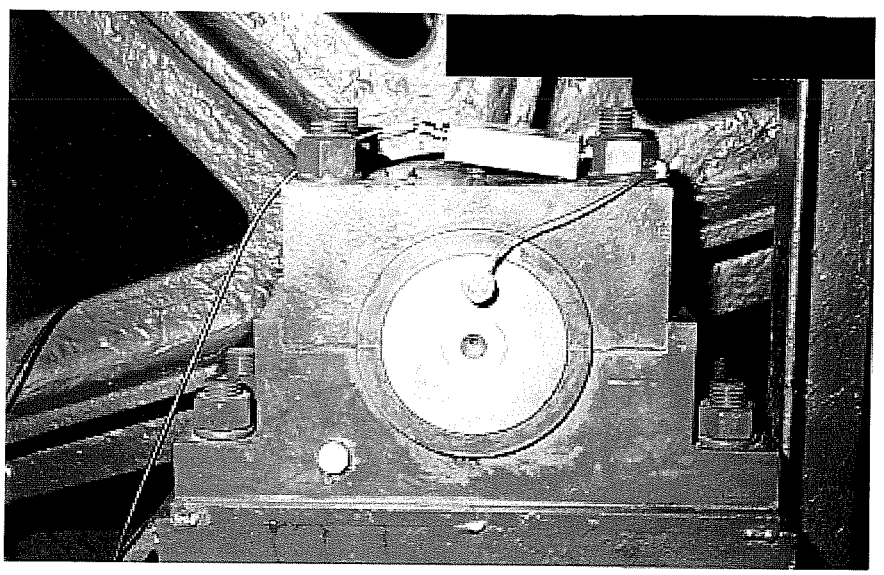

Figure 3.24: Broadband Sensor Attached to Main Hoist Drum Shaft with External Pre-Amplifier

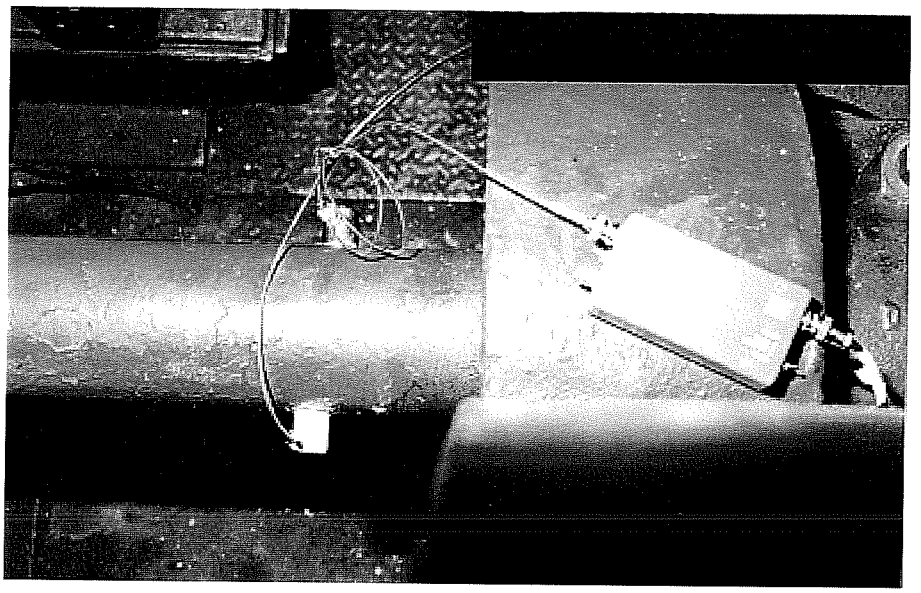

Figure 3.25: Broadband Sensor Attached to Boom Hoist Drive Shaft with External Pre-Amplifier

3.4.9 Verification of Sensor Sensitivity and Coupling

Verifying that AE sensors are properly coupled to the test piece and are functioning correctly with sufficient sensitivity is crucial to acquiring meaningful AE data. Such verification is performed twice: immediately before load testing begins, and immediately after completion of all AE tests. The most common verification technique is pencil lead breaks, in which a 0.3 mm 2H Pentel pencil lead is broken against the test piece. The pressure at which the pencil lead fractures causes a specific displacement on the surface of the metallic object. When the lead fractures, the material rebounds elastically the result of which is a pressure wave which is quite similar to that which occurs during an actual emission causing event. In addition to pencil lead breaks, two other methods were used to introduce signals into the crane shafts. Dunegan crackers were used to induce metallic cracking into a test piece attached to the crane shafts. A piezoelectric resonant transducer attached to a specially designed square wave generator (or pulser) was also used to generate simulated AE signals in the test piece. Each verification method will be described in more detail presently.

3.4.10 Pencil Lead Breaks

After placement of all AE sensors, a 0.3 mm Pentel 2H lead was broken 1" from each sensor. The lead was extended approximately 2.5 mm for each break, and breaks were done with the lead at 30 degrees with respect to the surface of the shaft. Five breaks were recorded at each sensor, and it was confirmed that the amplitudes of the five breaks were within 4 dB of each other. It was also confirmed that the average amplitude recorded by each sensor was

within 4 dB of the average amplitude recorded by all the other sensors of similar type. Typical average amplitudes for the 150 kHz resonant sensors were around 80 dB, while that number decreased to around 75 dB for the broad band sensors. It was much more difficult to obtain consistent results with the broad band sensors than it was with the resonant sensors.

The procedure used is in compliance with the American Association on Railroads Procedure of AE Evaluation of Tank Cars and Intermodal Tanks[15] for determining that sensors are working properly.

3.4.11 PAC Pulser

A Physical Acoustics Corporation (PAC) model C-101-HV electronic pulser was used to send a square wave pulse to a 150 kHz resonant transducer. The transducer introduced a very repeatable 150 kHz signal into the shaft. To evaluate sensor sensitivity using the pulser, the transducer was placed on the shaft 1" from each sensor, and was acoustically coupled to the shaft with high temperature silicone vacuum grease. As in the case of the pencil lead breaks, this AE simulation was repeated five times at each sensor, with the average amplitudes being compared to the average amplitude of other sensors of the same frequency. The pulser signal was found to more consistent in amplitude than the pencil lead breaks, and again indicated that the sensors were well coupled to the shaft and operating with appropriate sensitivity.

It should be noted that additional pencil lead breaks and pulses were applied at various intervals from each shaft face. This data was used to study the signal attenuation characteristics of in-situ crane shafts, as well as those types which were not studied in the laboratory.

3.4.12 Dunegan Cracker

A Dunegan cracker is a device that couples true AE signals from a cracking metallic material into the desired test piece. The cracker holds a torqued, hydrogen-embrittled bolt. AE released from this bolt is transferred, via a waveguide, from the bolt into the test piece. The objective of using a Dunegan cracker is to verify that a specific AE set-up will detect real AE signals, and to observe how these real AE signals, generated only at one location on the test piece, are received at each of the sensors.

3.4.13 Verification After Load Testing

Pencil lead breaks were repeated on each shaft after completion of AE load testing. In all but one case (sensor number 5 on the boom drive shaft), the lead breaks after testing were very similar to the lead breaks before testing, leading to the conclusion that the AE sensors did not fail or lose coupling during the test.

Sensor number 5, which was a broadband sensor on the boom drive shaft, showed amplitudes slightly lower that it did prior to load testing. However, these amplitudes were still in the 70 to 80 dB range indicating that sufficient coupling existed to identify AE signals. The sensor was also remounted with hot melt glue and pencil lead breaks repeated to verify the sensor had not failed. After remounting, the sensor recorded amplitudes were very similar to pre-testing levels. It was thus concluded that small amount of decoupling of sensor number 5

occurred during AE data acquisition, but this decoupling was not large enough to seriously effect the test results.

ANALYSIS AND RESULTS

4.1 FINITE ELEMENT MODELING

A three dimensional finite element model of the critical area of the shaft was developed using the ABAQUS 5.6-2 software package being run on a Cray T90 Parallel Vector Supercomputer. The goal of this analysis was to better understand the state of stresses that existed in the shaft under torsional loading, and to compare the crack propagation rates in the model to that in the real shaft under fatigue loading.

The full geometry of the specimen was modeled, taking advantage of the symmetry between the front and the rear of the shaft. As in the experimental setup, load was introduced into the model via the key and keyway system. Material properties such as elastic modulus, toughness, ultimate strength, and hardness were taken from Naval test reports provided, other required values such as Poison's ratio, and the yield stress were either back calculated from the other data provided by the Navy, or found in tables for the type of steel being used.

An initial crack was input into the model. The location and size of this crack was taken directly from Naval reports on other failed crane shafts, which had been sectioned. The location of the crack introduced into the model started at the inside corner of the keyway and was 1/8" long proceeding into the volume of the material. The choice of the initial size of the imperfection was somewhat arbitrary, the main thrust being that it was in the direction of the proposed failure plane of the model, which was taken directly from observed failures in the field.

The loading of the model was identical to that used in the laboratory. The crack grew along its failure plane as shown in Figures 4.2 through 4.4. As a check, it was verified that the failure plane used in the model was indeed the path of greatest energy release as indicated by the contour integral calculation in the analysis. This lends great credence to the fact that the proposed failure plane (required for the finite element analysis to proceed) is indeed a plausible one. The geometry of the model is complex. Figure 4.1 shows the part of the model which is displayed in the remaining figures for the results from the finite element analysis.

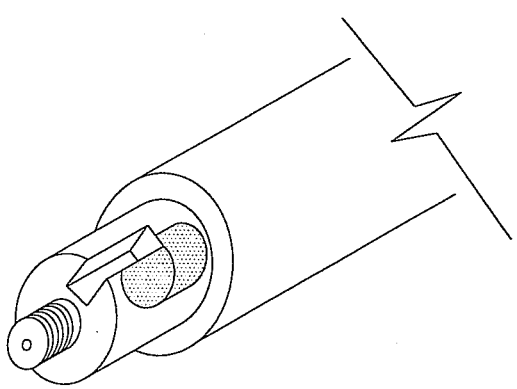

Figure 4.1: Section of Shaft shown in Finite Element Analysis Results

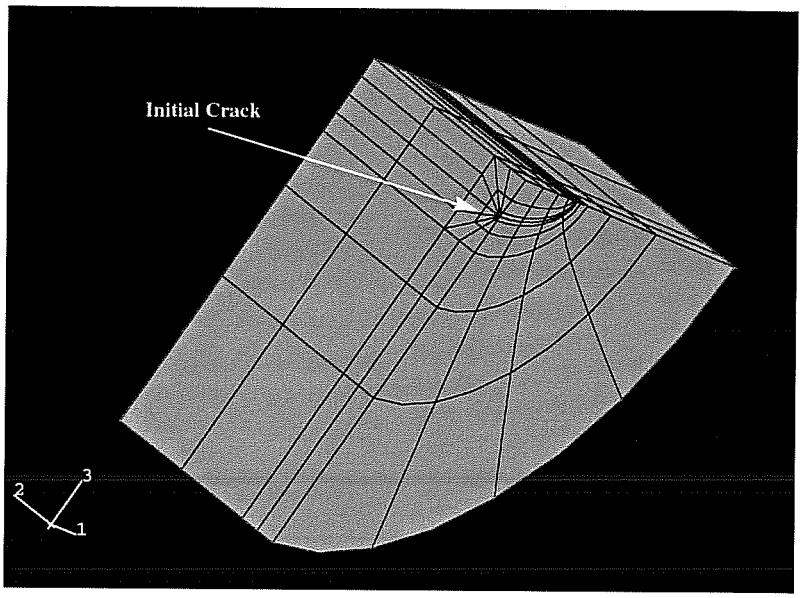

Figure 4.2: Initial Crack Introduced into Model

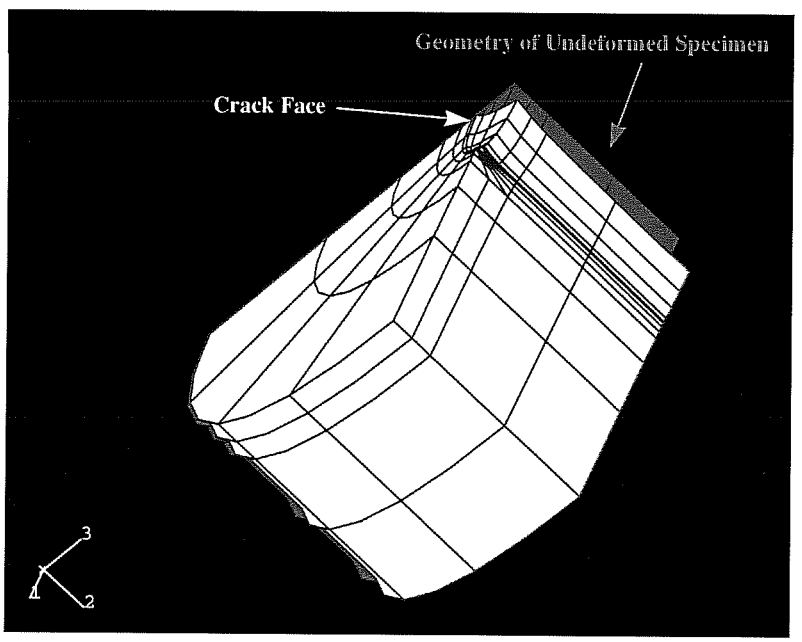

Figure 4.3: Crack at the end of 55 in-kip Fatigue Load Level

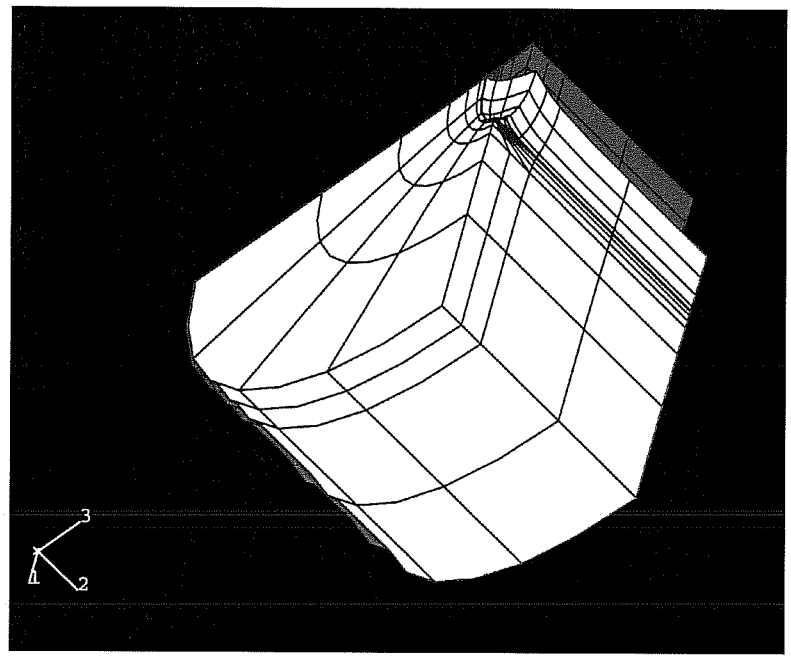

Figure 4.4: Crack at the end of 95 in-kip Fatigue Load Level

It may be seen from the foregoing figures that the crack propagates through the volume of the material as the fatigue cycling progresses, and the crack tip opening displacement (seen in the upper left corner of the model) gets progressively larger. The results obtained verify what was thought to be occurring in the shaft, intuitively. Additionally, the stress contour plots, seen in Figures 4.5 and 4.6 allowed for a better understanding of the stress field in the body as a whole, especially at the crack tip.

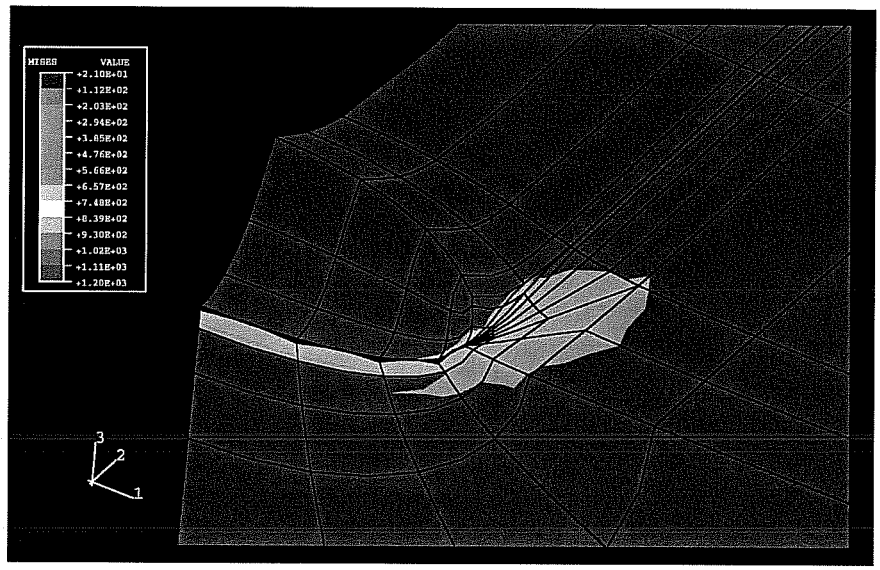

Figure 4.5: Stress Contour of Entire Body under 55 in-kip Clockwise Loading

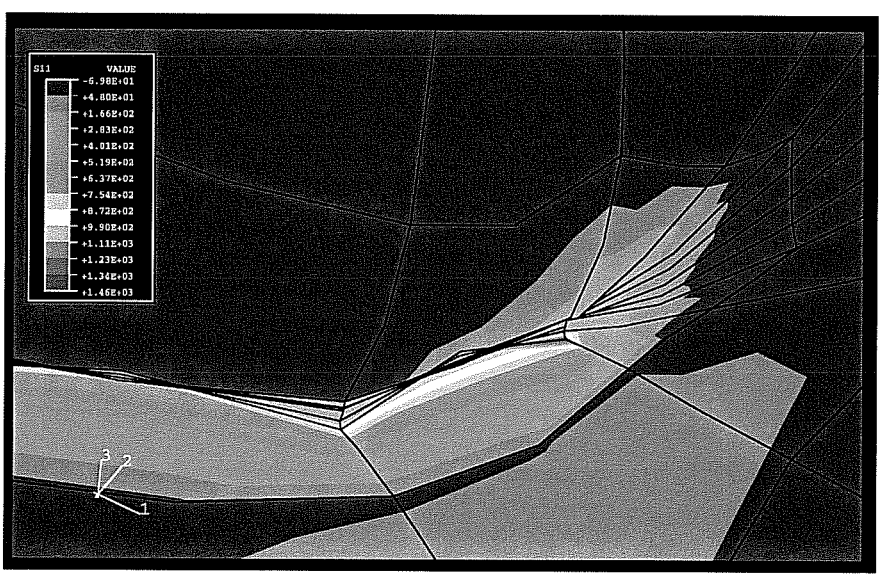

Figure 4.6: Stress Contour of Area Near Crack Tip

Using the stress analysis from the model, the shear stresses introduced into the shaft by the torsion were decomposed into stresses normal to the plane of the crack face. By so doing,

the direction of twist that caused crack opening and the direction that caused crack closing was determined. In the present case, clockwise loading was seen to open the crack, while counterclockwise loading was seen to close the crack. This corresponds well to the data obtained from the AE testing, which will be discussed to follow.

4.2 ANALYSIS METHODS FOR THE AE DATA

4.2.1 Genuine and False Emission

Not all emission is genuine and the ability to distinguish genuine from false emission is a key issue in an acoustic emission test procedure. False emission can arise from a number of sources including mechanical rubbing, wind-induced movement of the cables and sensors, rain, sleet, thermal expansion due to the sun, and corrosion. False emission due to sliding friction was a particular problem with the setup used in the lab.

In the past few years, new techniques have been developed for identifying false emission and applying post-test filtering. Filters, such as the Swansong series of filters[15], eliminate spurious emission from the data record. Post test filtering of data files is almost always required, and many inspectors make it a standard practice to run all data through one of the Swansong filters.

For the present research, the Swansong II filter was used. The Swansong filters are based on the observation that certain telltale hit parameters, such as low amplitude and long duration, characterize sliding and mechanical rubbing. In the Swansong II filter, data are removed for a period of 1 second. The Swansong II filter is defined by the following:

$$\begin{aligned} &\text{If } (A_i - A_{th}) < 5 \text{ and } D_i > 2 \\ &\text{or } (A_i - A_{th}) < 10 \text{ and } D_i > 3.5 \\ &\text{or } (A_i - A_{th}) < 15 \text{ and } D_i > 4.5 \end{aligned} \qquad \text{(Equation 4.1)}$$

then eliminate all hits during the period (seconds):

$$(T_i - 0.5) \text{ to } (T_i + 0.5) \qquad \text{(Equation 4.2)}$$

where for a given hit, i

A_i is the amplitude (dB)

A_{th} is the data acquisition threshold (dB)

D_i is the hit duration (ms)

T_i is the arrival time (sec)

Equation 4.1 is used to define the telltale hits and must be applied on a channel-by-channel basis using the specific threshold for each channel. Tests have shown that some of the sensor hits caused by mechanical movement have large amplitude, high energy characteristics, and propagate throughout the system under test. Accordingly, emissions occurring immediately before and immediately after a telltale hit are removed from all channels. For this reason, Equation 4.2 is applied to all channels on the item under test. The Swansong zone, per se, on a correlation plot is shown in Figure 4.7.

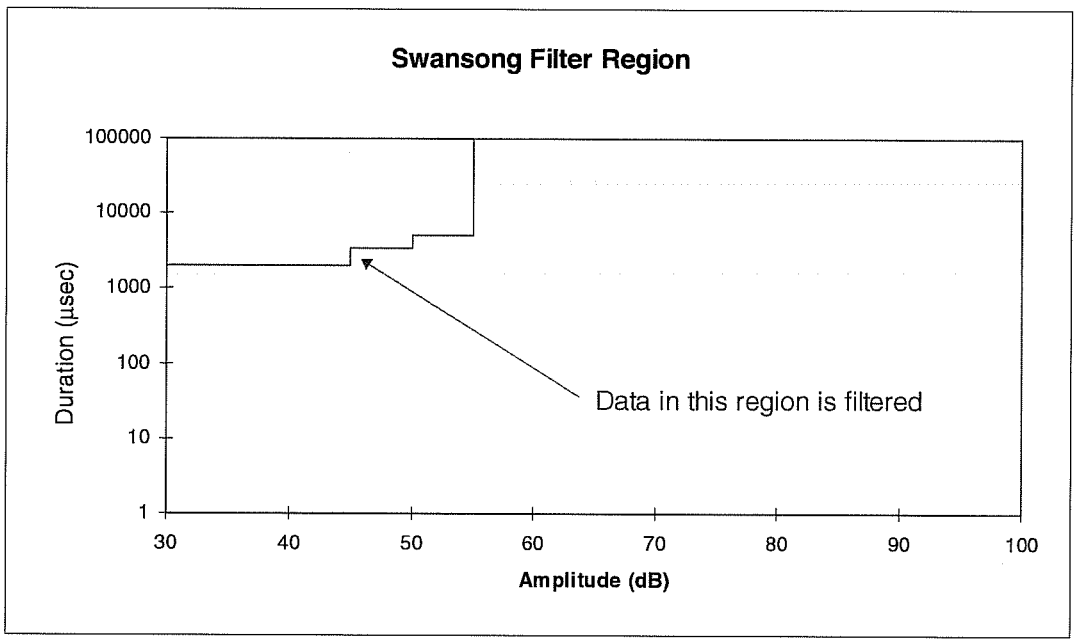

Figure 4.7: Swansong Zone on a Correlation Plot

4.2.2 Intensity Analysis

Intensity analysis is a measure of the structural significance of an acoustic emission source. The technique has been discussed in the literature[16] and the method has been used extensively for analysis of defects in metal equipment. The technique is based on test data from destructive vessel tests, controlled tests with detailed follow-up nondestructive evaluation, and over 1000 tank and pressure vessel tests. The empirical factors described to follow and the intensity grading have been developed by comparing the acoustic emission data with fracture mechanics and finite element based studies of detected defects.

Intensity analysis is a valuable tool for assessing the structural significance of a flaw. The results of the analysis provide guidance on continued operation of the equipment, and the need for follow-up visual inspection, more frequent testing, or possible shut down.

Intensity analysis is carried out on a per channel basis, and uses two factors based on signal strength. The first factor is known as historic index, and compares the signal strength of the most recent hits to the signal strength of all hits. Historic index is essentially independent of specimen size. The second factor, referred to as severity, is the average of the largest signal strength hits striking the sensor. The use of signal strength to define historic index and severity reduces the effect of distance from the sensor, and allows the intensity analysis to be used on the full range of field geometries. Historic index is defined by:

$$H(t) = \frac{N}{N-K}\left(\frac{\sum_{i=K+1}^{N} S_{0_i}}{\sum_{i=1}^{N} S_{0_i}}\right)$$

Where:

$H(t)$ is the historic index at time t.

N is the number of hits up to and including time t.

S_{0_i} is the signal strength of the ith hit.

K is an empirically derived factor that varies with the number of hits and is different for different materials.

Severity, S_r is defined as the average signal strength for the J hits having the largest numerical value of signal strength:

$$S_r = \frac{H_f}{J}\sum_{m=1}^{m=J} \psi(h)_m \, S_{0_m}$$

where:

S_{0_m} is the signal strength of the mth hit (m being ordered on the magnitude of the signal strength).

J is an empirically derived constant that depends on the material of construction. Typically, $J = 10$ for most metals.

H_f is known as the Maize factor and depends on the loading. For tests which use an overload procedure, $H_f = 1$.

$\psi(h)_m$ is a function of the threshold h.

In many common test AE test procedures, such as the MONPAC[16] procedure, the results of the intensity analysis for each sensor are plotted on a chart divided into zones as shown in Figure 4.8 which shows intensity analysis results for a pressure vessel. The meaning of the six zones lettered "No Significant Emission" through E is shown in Table 4.1. As will be described in Chapter 5 a modification and simplification of this approach was developed for the crane shafts.

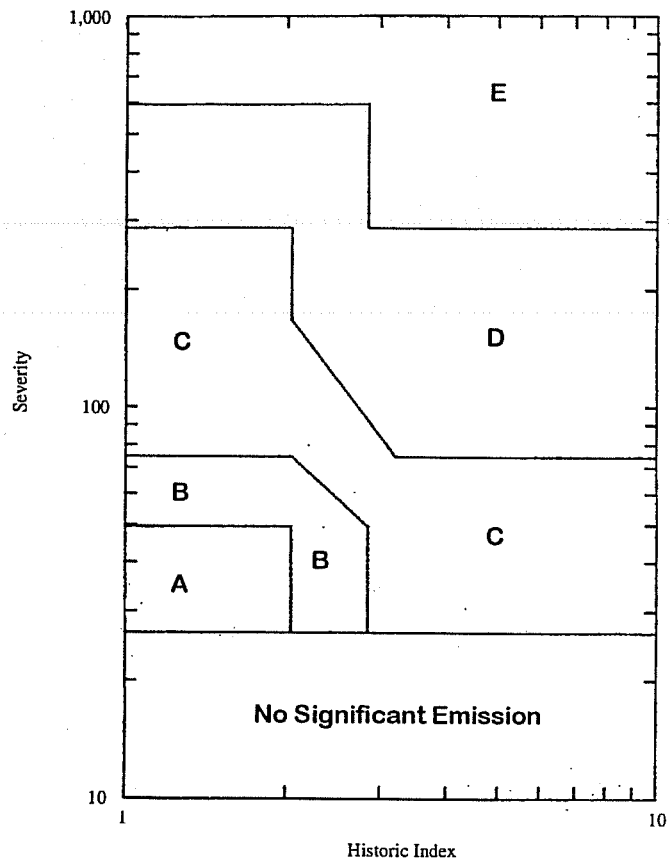

Figure 4.8: Intensity Plot for a Metal Pressure Vessel used in the MONPAC Test Procedure

Table 4.1: Significance of Intensity Zones for Metallic Pressure Vessels

Zone Intensity	*Recommended Action*
No Significant Emission	Insignificant Acoustic Emission. No follow-up recommended.
A	Minor defect, note for reference in future tests.
B	Note for reference in future tests and check for minor surface defects such as corrosion, pitting, gouges, or cracked attachment welds.
C	Defect requiring follow-up evaluation. Evaluation may be based on further data analysis, or complementary nondestructive examination.
D	Significant defect requiring follow-up inspection.
E	Major defect requiring immediate shut-down and follow-up inspection.

4.2.3 Source Location

For the present work, the Jolly-Stuart method of source location was used. This zonal location technique is robust and defines a small area which contains the defect. The Jolly-Stuart technique uses all sensor hits to refine the zone of interest. This is in contrast to conventional time-of-arrival source location which requires a minimum number of hits from an AE event to locate an emission source. Time-of-arrival source location utilizes hit arrival times and assumed wave velocity to calculate the position of the source. For a number of reasons, this technique has given incorrect answers and most codes and standards utilize zone source location[17].

The Jolly-Stuart method divides sensor hits into two categories, first hit and ancillary hit. As a stress wave propagates through a structure it will strike a number of sensors. The first sensor struck will record the "first hit". Subsequent hits to other sensors are referred to as "ancillary hits". Reflections, which can strike the first hit sensor and other sensors are also considered ancillary hits. Ancillary hits are ordered as second, third, fourth, etc. hits. The Jolly-Stuart uses the following algorithm for determining first and ancillary hits:

- Order all hits by time. For hits with the same time, order by amplitude. For hits with the same amplitude, order by signal strength.
- Consider hits in the time range, T to T+ΔT, as being caused by the same stress wave. T is the time of the first hit arrival. ΔT is the time for the stress wave to travel to other

sensors. Hits that occur beyond this time range are considered to be from a different stress wave.

- If a hit has an amplitude of 5 dB or greater than the first hit, consider the new hit as a first hit and restart the process.

For the four foot long crane shafts studied in the laboratory, the travel time, ΔT, was one millisecond. This travel time represents the time for the wave to travel the complete length of the shaft and back plus 15 percent. Accordingly, reflections at the sensor nearest the emission source were considered ancillary hits.

4.3 DATA ANALYSIS

A large amount of data was collected during the course of experimentation, as both the overload data and the fatigue load data for over 60,000 cycles were recorded. The data was analyzed in separate groups consisting of positive overloading, negative overloading, load holds for both positive and negative overloading, and positive and negative loading and load holds during the fatigue loading. All the data was subject to the Swansong II filter before analysis. The data sets were spot checked at regular intervals by looking at the waveforms and power spectra for individual hits to verify their validity and admissibility.

4.3.1 Positive Overloading

A total of 39 positive overloads were conducted during the course of the experiment. In order to isolate the data of interest, a post test filtering process was adopted. The computer program ATPOST by PAC, supplied as part of the MISTRAS-2001 software package, was used in this effort. Ideally, because of the Kaiser and Felicity effects, during an overload cycle the sample should generate no acoustic emission until it reaches a load greater than the fatigue load level being used, unless it is damaged. Some of the problems with background noise described in Chapter 3 came to bear during extremely low loads in the fatigue and overload cycles. It is suspected that the reasons for this stemmed from the hydraulic fluid moving between the rams near the zero load and the key shifting bearing positions as the load was transferred from one direction to the other. The latter cause came to dominate toward the end of the testing regime as the key was worn down, and the amount of potential movement during a bearing shift increased.

The filter used the load parametric input to determine what data to accept into the filtered data set. Data would start to be accepted at about 30% of the ultimate load level reached, and stopped immediately prior to the load level, to prevent any of the load hold data being captured. This is shown schematically in Figure 4.9. Typical data as collected during the entire overload cycle is shown in Figure 4.10

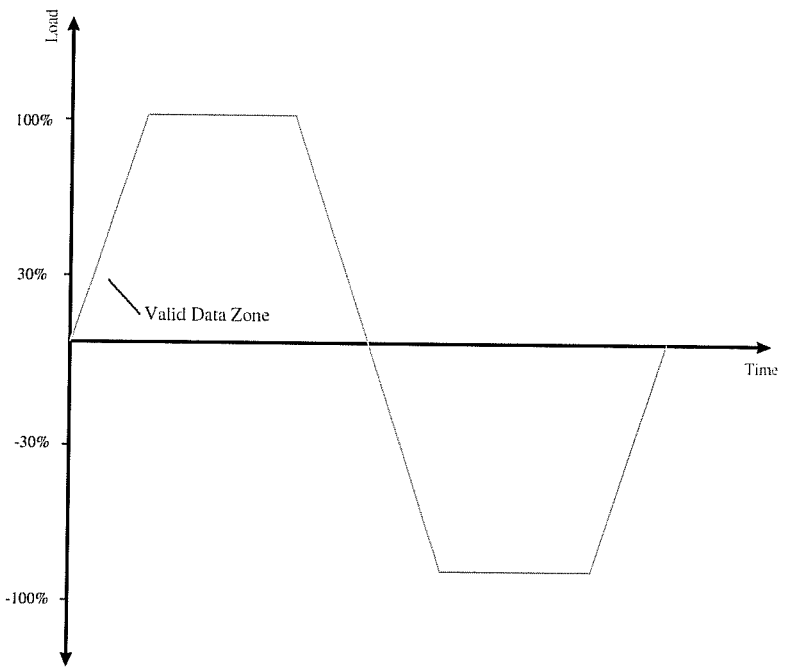

Figure 4.9: Values of Load for which Data was Accepted during Positive Overload Data Filtering

The data for each of the two overloads and load holds for a specific fatigue load level was analyzed separately. The cumulative signal strength for the hits on all channels in the zone of interest was calculated, and is shown in Figure 4.11.

The data obtained was remarkably good. It is important to note that the data presented in Figure 4.11 is not cumulative. The data at each fatigue load level is separate and unique from the data before it. Emission appears at fatigue load level of 40 in-kips, the starting load level, which in the present case is greater than the load the shaft ever experienced when being used in the field. Emission over the next few overload levels remains reasonably constant, indicating that under the fatigue load cycling, the rate of damage accumulation is constant, and seemingly load independent. The damage occurring at these low load levels is likely quite minor. A visible "knee" appears in the data trend at a fatigue load of 60 in-kips, and from that point on damage begins to accumulate at a much faster rate. It is interesting to note that the trend is almost linear as load level increases, indicating that greater loads cause damage to occur more rapidly. This result is consistent with the fracture mechanics finite element analysis data and known material failure mechanics theories, although it is inconsistent with Williams[91] approach detailed in the literature review. Williams suggests that the range $\Delta\sigma$ affects the rate of crack growth; the experimental evidence points toward the absolute value of σ as a predictor.

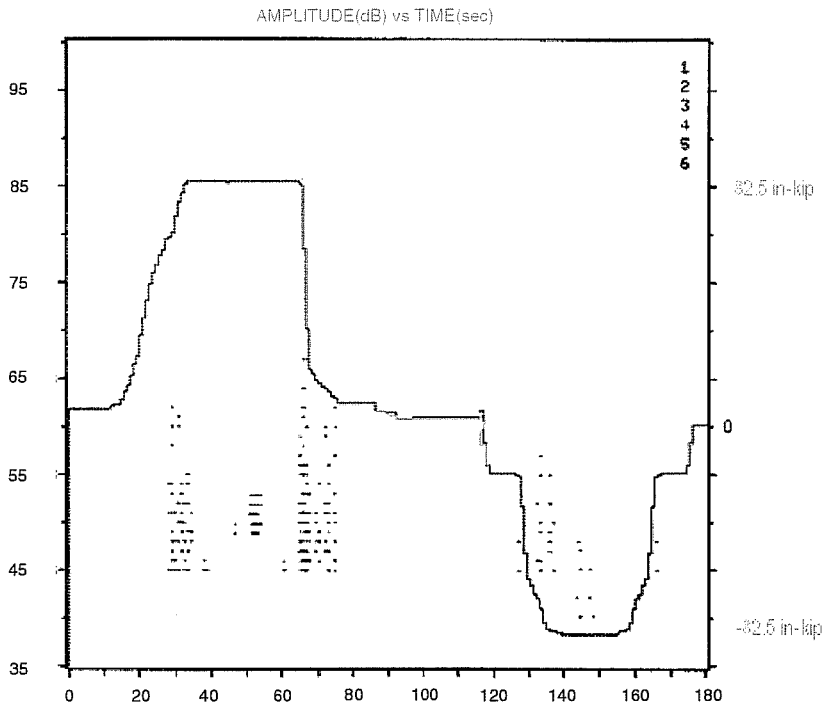

Figure 4.10: Typical Data Set Collected During Overload Cycle. Load Parametric is Superimposed on Amplitude vs. Time

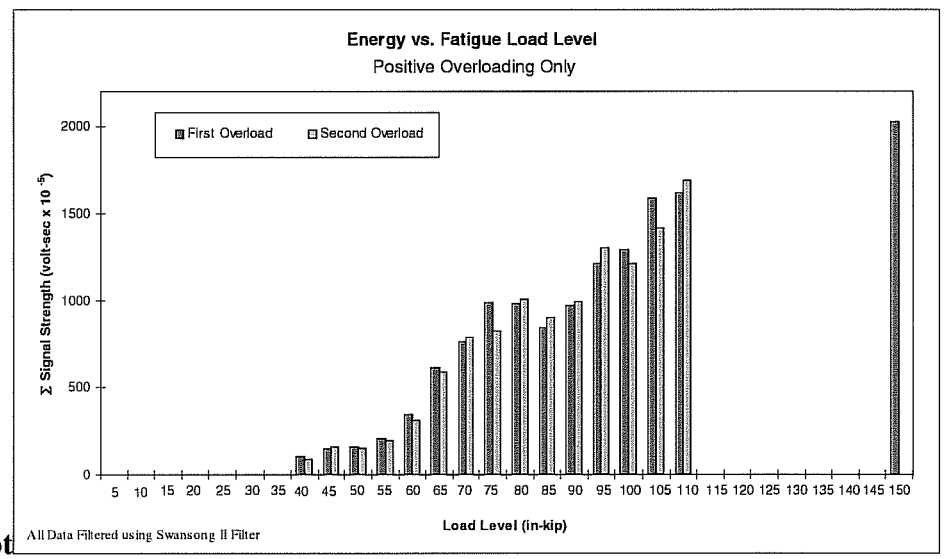

Plot

Figure 4.11: Energy vs. Fatigue Load Level During Positive Overloading

The Felicity ratio for each overload was also calculated. The calculation was done manually for all overloads. A load versus time plot was superimposed on a hit amplitude versus time plot with equivalent scale x-axes. The load level at which emission was first detected was divided by the fatigue load level in order to determine the Felicity ratio. The data used in these calculations was previously filtered, and only included data in the zone of interest. Figure 4.12 shows the results of the calculations.

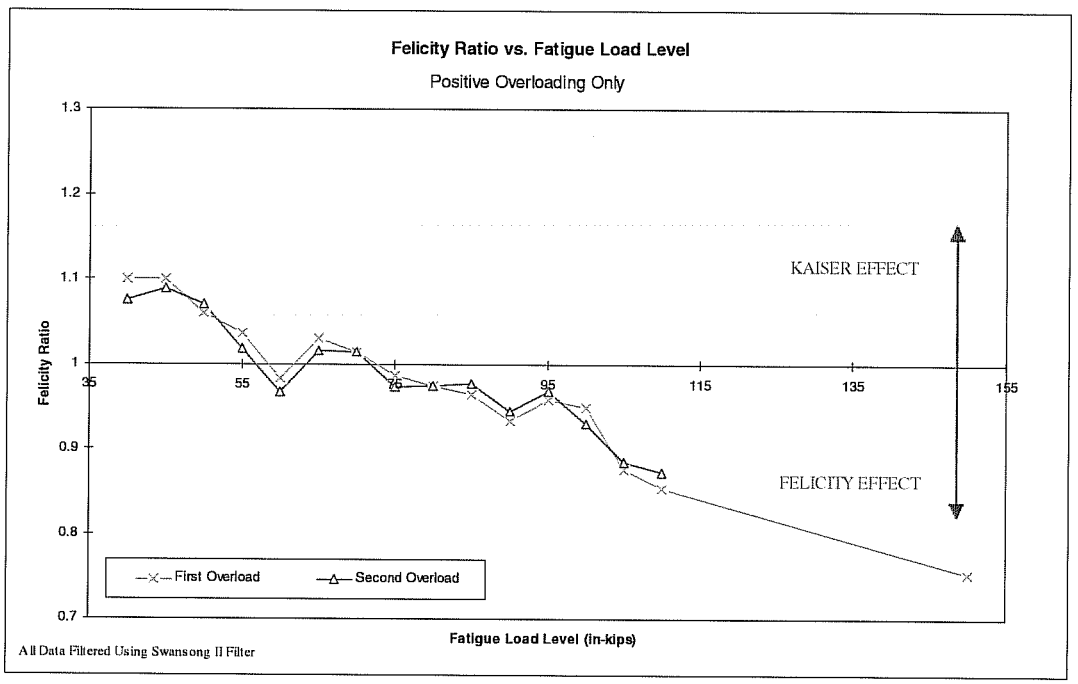

Figure 4.12: Felicity Ratio vs. Fatigue Load Level for Positive Overloading

The lower load levels show Felicity ratios greater than unity, indicating that the crane shaft is performing well. The Felicity ratio starts to decrease to a value less than one at around the same point as the "knee" in the cumulative signal strength versus load plot occurs. An interesting result. The data trend is decreasing in a reasonably linear fashion. The points at which the Felicity ratio increases slightly compared to its previous can perhaps be explained by the fact that the blunted cracks didn't grow as much during the preceding load cycles, however the increase does not always occur with both data points at a particular load level and the change in values are sufficiently small as to safely assume that they are insignificant, and do not reflect on the general trend observed.

In acoustic emission testing a Felicity ratio as low as 0.95 is cause for concern, and usually requires that follow-up action be taken. The data at the upper load levels shown in Figure 4.12, decreasing toward 0.8 is indeed cause for alarm. The extremely low Felicity ratio,

in combination with the high cumulative signal strengths observed at the upper load levels indicates that there is significant cracking in the shaft which is active under clockwise loading.

4.3.2 Negative Overloading

Analysis of the negative overloading regime was carried out in an identical fashion to the positive overloading regime. Again, a 30% to nearly 100% of load "zone of interest" filter was applied, as was the Swansong II filter. Figure 4.13 graphically illustrates the zone for negative overloads.

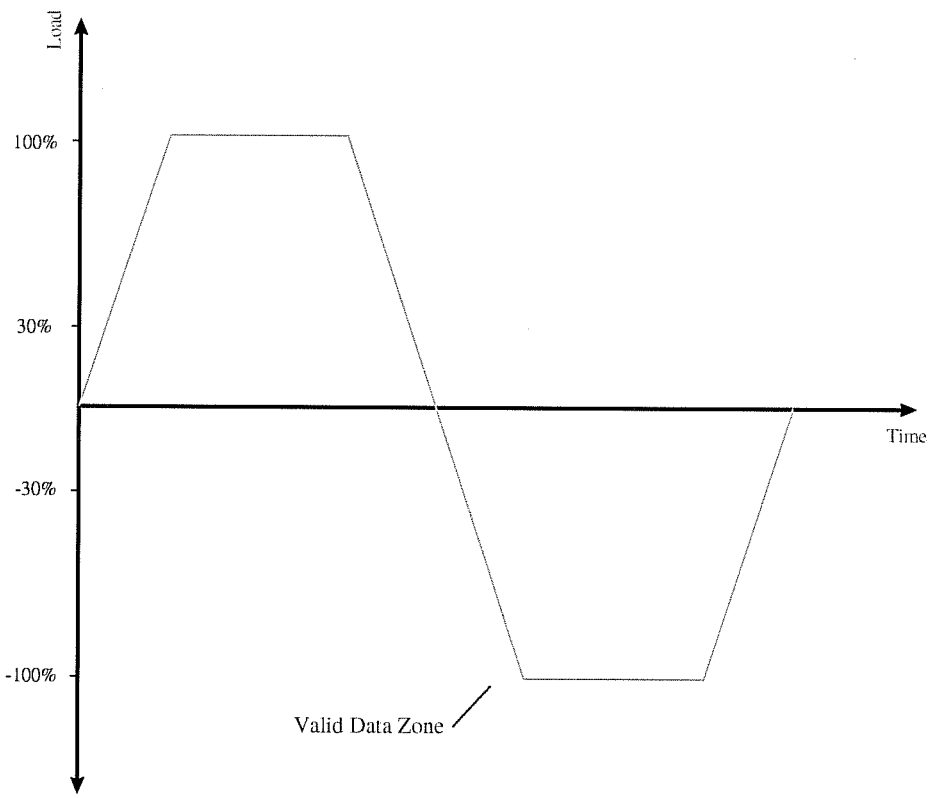

Figure 4.13: Values of Load for which Data was Accepted during Negative Overload Data Filtering

The unloading data going from 30% of the maximum positive load down to zero load was of little interest. As seen in Figure 4.10, generally speaking this load range had few hits and most of the hits recorded were subsequently filtered out when the Swansong II filter was applied, leading to the conclusions that mostly non-genuine emission was being generated during the unloading phase. Figures 4.14 and 4.15 are plots of Energy versus Fatigue Load

Level and Felicity Ratio versus Fatigue Load Level, respectively. They were calculated in the identical manner as the positive overload data, described previously.

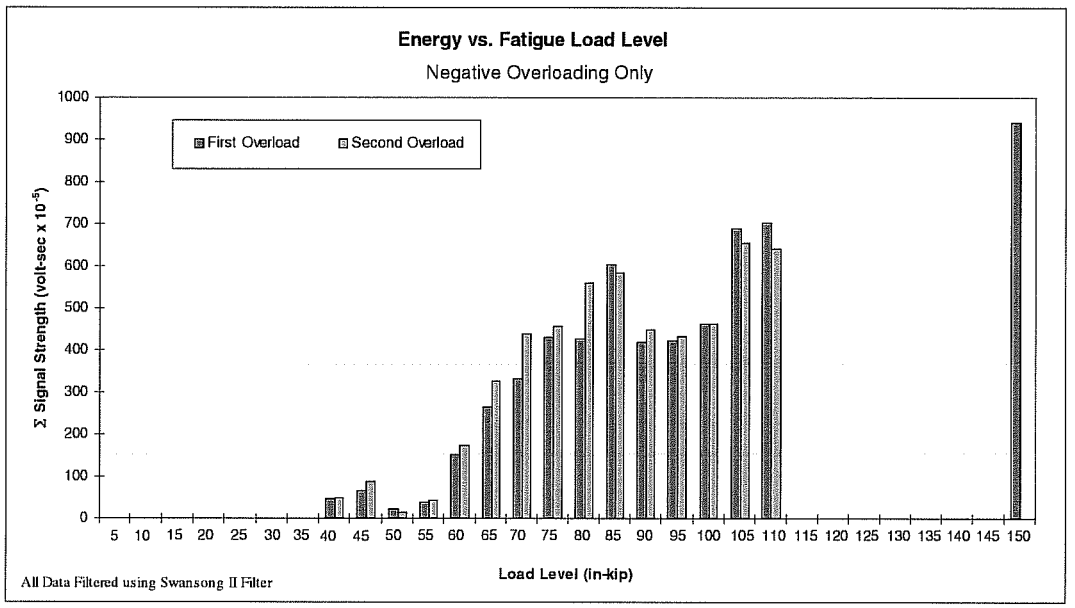

Figure 4.14: Energy vs. Fatigue Load Level During Negative Overloading

By way of comparison, the data from the positive overload cycle and the negative overload cycle show the same general trend. The cumulative energy increases in a fairly linear fashion, although there are more dips and flat plateaus in the negative overload data than in the positive overload counterpart. This may be an indication that if the crack is opened by positive load, the negative load (crack closed) with shear dominating may be more sensitive to changes in crack growth. They represent a relatively small deviation from the linearity of the data trend, and are thus thought to be insignificant.

An important feature to notice in the negative overload data is that the magnitude of the cumulative energy released at each fatigue load level is lower than that released during the positive loading. This indicates that the crack is more active in one direction than in the other, meaning that more damage is occurring under clockwise loading than is under counterclockwise loading. This is consistent with the finite element analysis results which showed the crack to be opening when the shaft was subject to clockwise load. In relative terms, the cumulative signal strength levels during negative loading are approximately one half of what they are during positive loading. The combined state of stress under the counterclockwise load is likely promoting crack closure, and some compression yielding, a phenomenon well documented in the literature, but obviously to a much lesser extent than the clockwise loading is causing damage by crack opening.

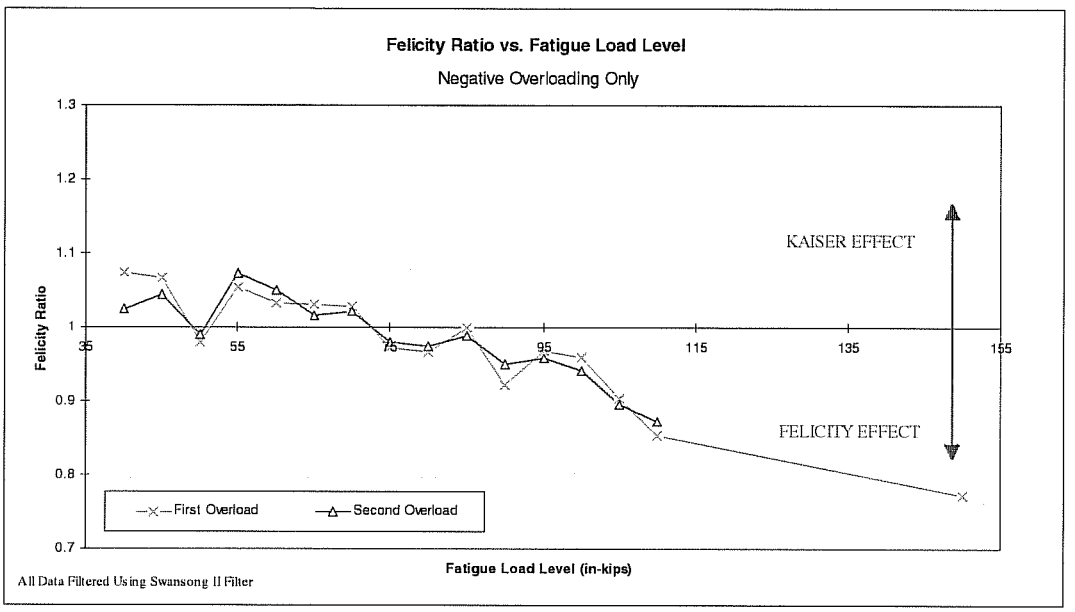

Figure 4.15: Felicity Ratio vs. Fatigue Load Level for Negative Overloading

The results from the Felicity Ratio calculations for the negative overloading are consistent with the results obtained from the positive overloading. The trend of a decreasing Felicity Ratio with increasing load is again observed, as are the minor fluctuations in the data. The fluctuations are not of great magnitude, and are once again thought to be negligible compared with the overall trend observed. It is interesting to note that the Felicity Ratio for both the positive and negative overloads fall below unity and remain there at a fatigue load level of 75 in-kips. This may be a positive indication that for this specific shaft, the damage occurring as a result of loading in one direction begins to affect the behavior of the shaft in the other direction at this particular load.

4.3.3 Positive and Negative Overload Load Holds

The data for the positive and negative load holds for each overload cycle was contained within the same data set as the positive and negative overload data. The ATPOST program was used to filter all but the load hold data by using the load parametric with very narrow bands around the maximum load reached. This is shown schematically in Figure 4.16.

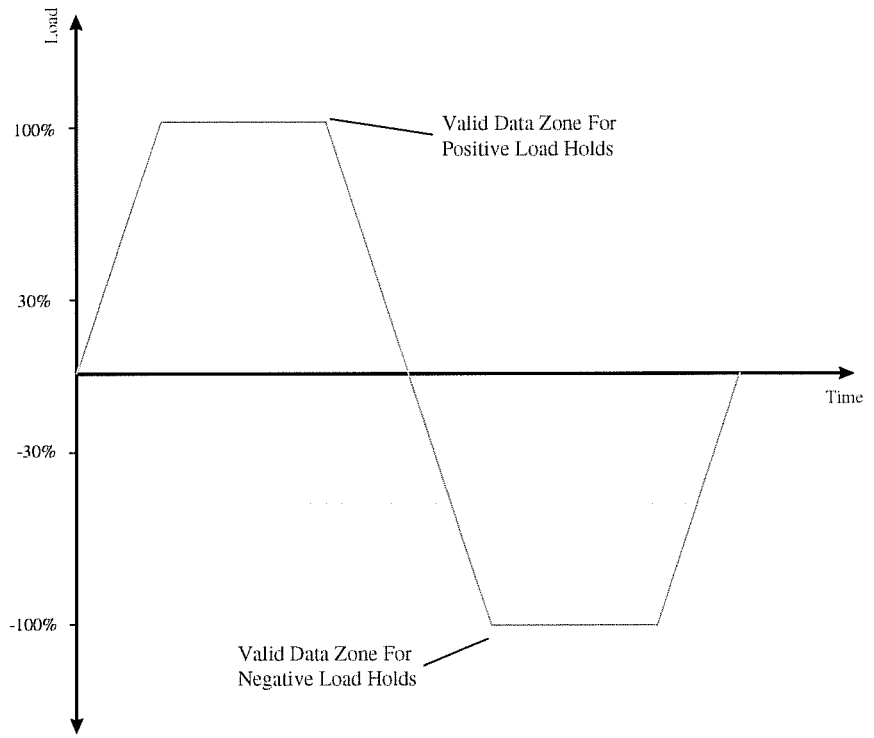

Figure 4.16: Values of Load for which Data was Accepted for Load Hold Data Analysis

As with the overload data, the cumulative signal strength for each load hold was calculated, and is shown in Figures 4.17 and 4.18. Unlike the overload data, however, the Felicity Ratio was not calculated, as it has no meaning in the case of load holds.

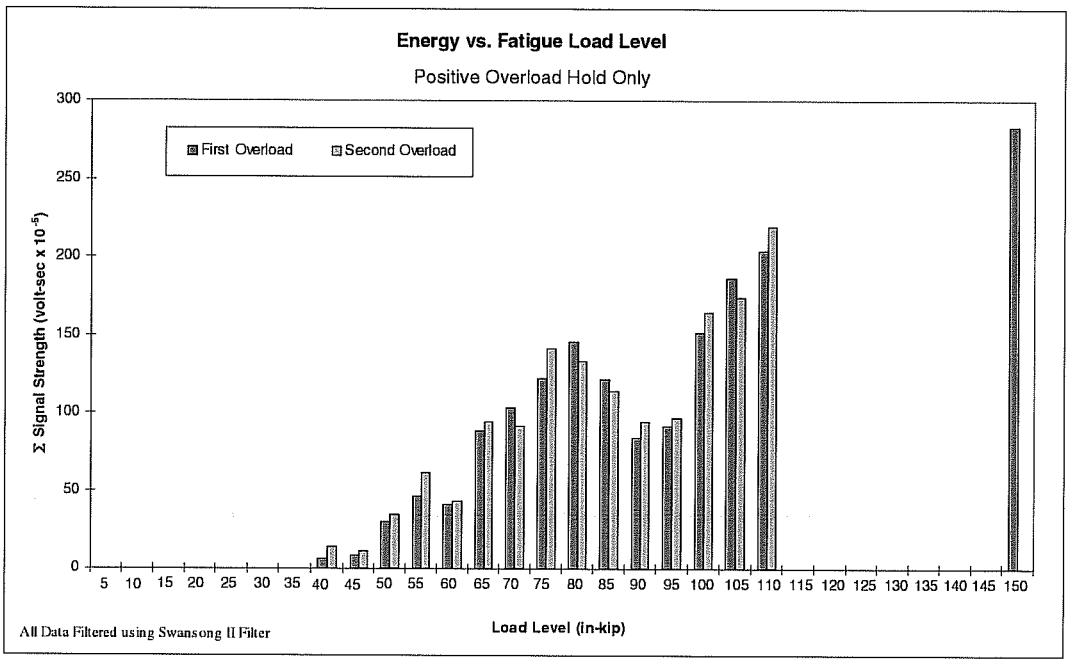

Figure 4.17: Energy vs. Fatigue Load during Positive Overload Load Holds

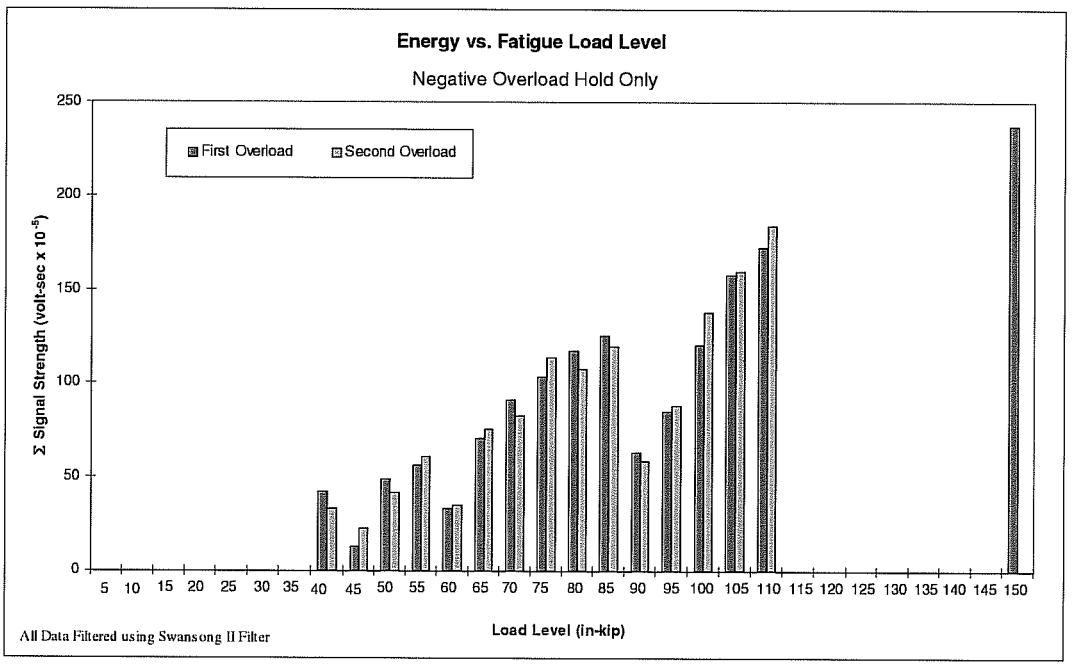

Figure 4.18: Energy vs. Fatigue Load during Negative Overload Load Holds

As with the overload data, a strong linear trend in the load hold data can be seen. The amount of ongoing damage after loading has stopped increases with increasing fatigue load levels. An important feature to realize with the load hold data is that the magnitude of the events are much lower than with the overload data (250 volt $\cdot$ seconds $\times 10^{-5}$ compared to 3,000 volt $\cdot$ seconds $\times 10^{-5}$), but the magnitude of the positive and negative load holds events are roughly equal. This observation lends credence to the entire notion that the load hold data is truly representative of the amount of damage that has occurred in the shaft, regardless of which direction it is being loaded in.

4.3.4 Fatigue Loading

The post test filtering of the fatigue loading data was carried out somewhat differently than with the foregoing data sets. Positive and negative loads were considered separately, but the load, load hold, and unloading data were all grouped in the same data set. This is shown graphically in Figure 4.19. As with the overload data, the first 30% of the load in either direction was filtered out.

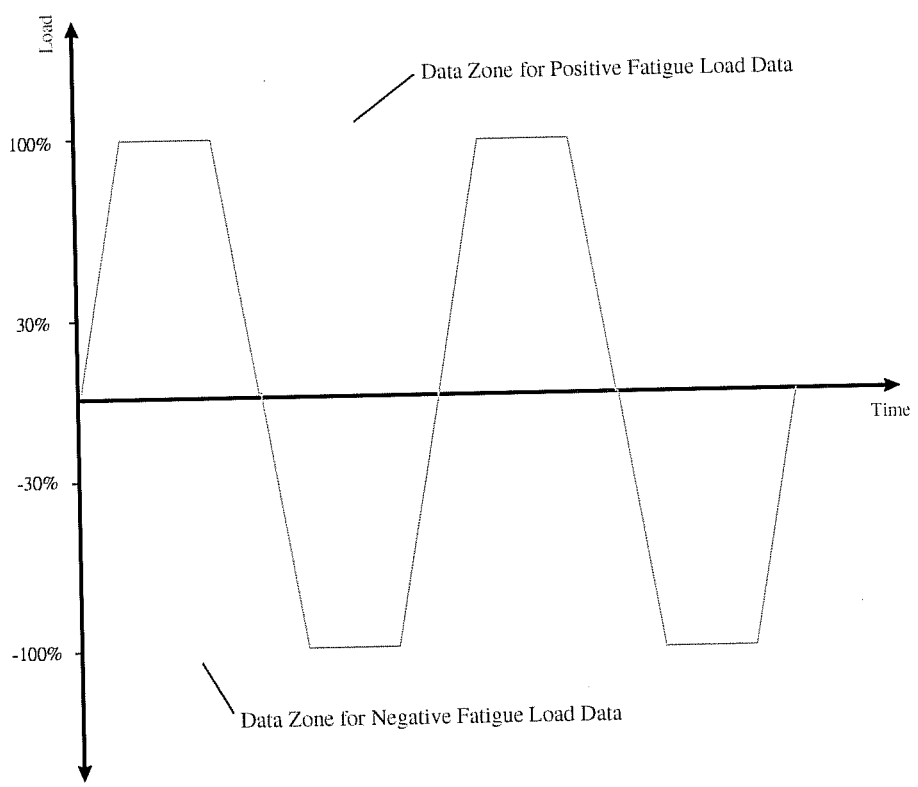

Figure 4.19: Data Zones for Positive and Negative Fatigue Load Data

It would have been much more desirable to filter within the blocks defined in Figure 4.19; for example to differentiate the data sets into data obtained while the load was increasing, data collected during the load hold, and data from when the load was decreasing. This would have allowed for pinpointing the type of emission generated during a fatigue cycle of the crack opening (during positive loading, for example) and the crack closing (during positive unloading) and would perhaps have allowed some signature analysis to be carried out. Due to limitations within the ATPOST software this was not possible, although at the time of writing Physical Acoustics Corporation was working on incorporating second order filters into subsequent releases of their software.

Part of a typical fatigue cycle is shown in Figure 4.20. The figure shows the positive portion of one of the fatigue cycles. The emission observed where the load level is low, at the start and end of the half cycle shown, is likely caused by some type of background noise. The emission observed just prior to the ultimate load and during the load hold is considered genuine data, and is precisely what the filter selectively accepts. The figure is typical insofar as when emission occurred during a cycle, remaining cycles looked similar to what is shown. The majority of all fatigue cycles, however, had much less, if any, emission - both when the load was changing and remaining constant.

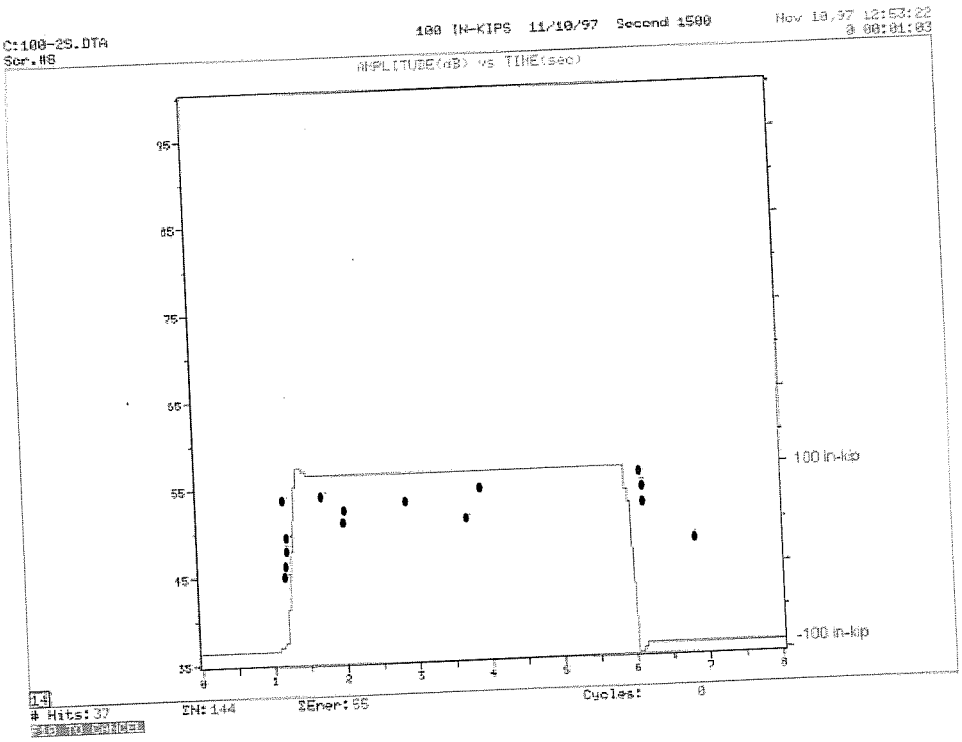

Figure 4.20: Typical Positive Portion of a Fatigue Load Cycle

The cumulative signal strength for each of the three, 1,500 fatigue loadings for each load level were calculated, and are shown in Figures 4.21 and 4.22.

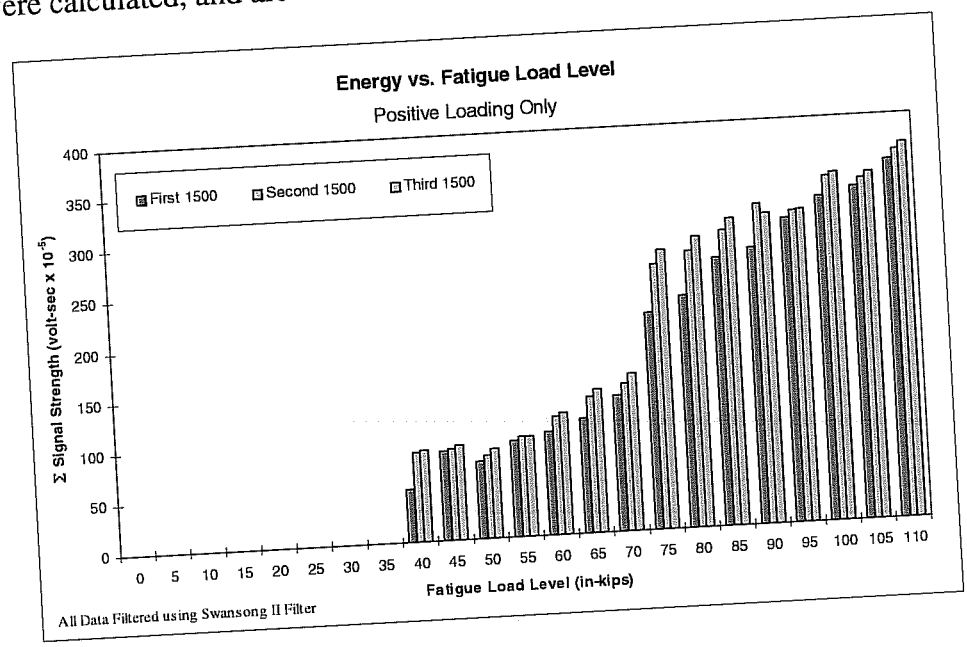

Figure 4.21: Signal Strength vs. Load Level for Positive Fatigue Loading

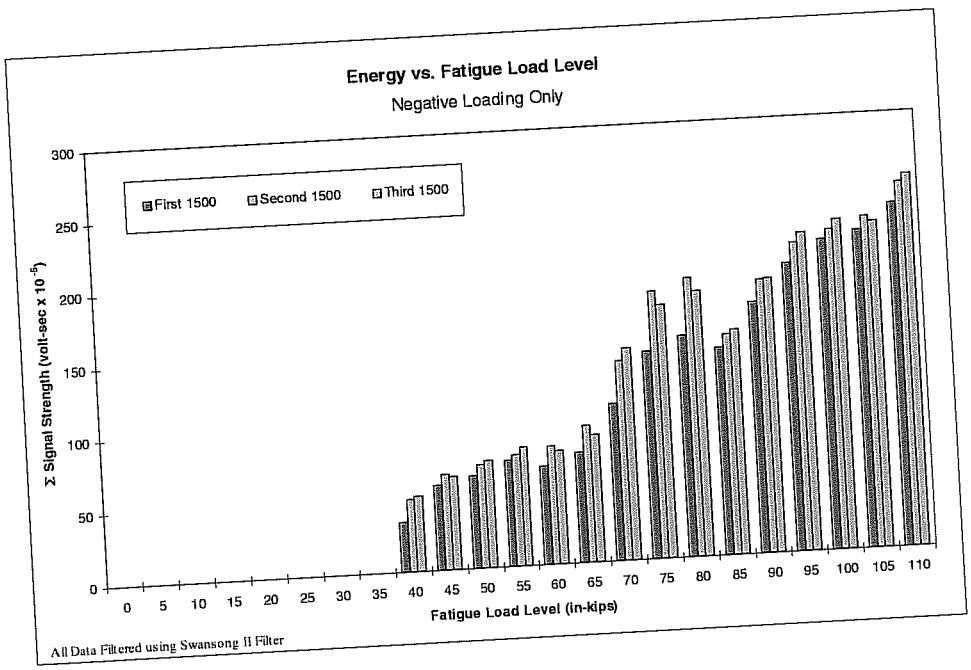

Figure 4.22: Signal Strength vs. Load Level for Negative Fatigue Loading

The positive and negative data may be discussed together, as for the most part they show the same trends. As with all the foregoing cases, the emission during negative loading is notably smaller in magnitude than the emission during positive loading. The emission during the first 1,500 cycles is lower than the emission of any of the succeeding 1,500 cycles at the same load. This result conclusively shows that more damage occurs at any given load level as the number of fatigue cycles grows. The emission occurring after the first and second overloads, for the most part, are very similar in their magnitude, indicating perhaps that damage occurs at a slower rate initially, and then transitions into a linearly increasing rate, with a more gradual slope.

It is worth noting that the cumulative emission during the fatigue cycles is less than the emission during the overload cycle that follows. This suggests that yielding during the overload causes more emission than the minute crack growth steps.

The data in the form presented in Figures 4.21 and 4.22 make an overall trend analysis difficult. To better observe what is occurring with the data on a macroscopic level, the data was examined in a different way. Figures 4.23 and 4.24 show the heretofore presented data, but in a cumulative manner. That is to say, the total signal strength at each load increment (all 4,500 cycles) was added to the total signal strength of the preceding load increment. In essence, the integral with respect to load of the bar charts in Figures 4.21 and 4.22.

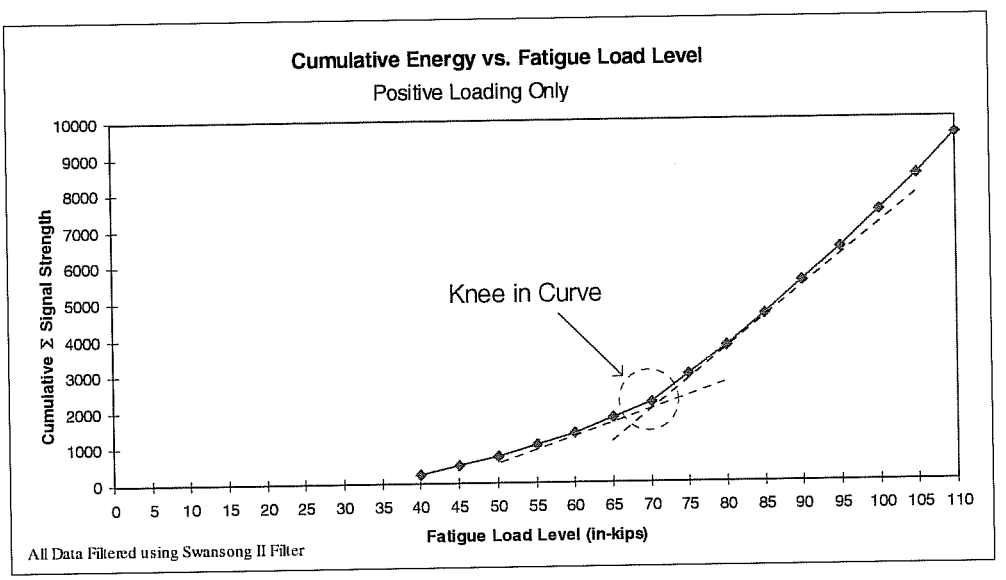

Figure 4.23: Cumulative Energy vs. Fatigue Load Level for Positive Loading. Overload Data Not Included.

The curves in both the positive and negative loading cases appear quite bilinear, with a distinct knee separating the two slopes as shown with the indicated tangents. Before the knee in the curve, damage to the shaft was occurring at a slower rate than after the knee. It is very interesting to note that in both cases, the load level at which the knee occurs is the same load

level at which the Felicity ratio was seen to consistently fall below unity in the overload data. This observation reinforces all the previous results, and additionally shows that the Felicity ratio is a very powerful tool in assessing the structural significance of a defect.

It was of some interest to look at the distribution of hits with time for the fatigue loading. Two different load levels are shown in Figures 4.25 and 4.26.

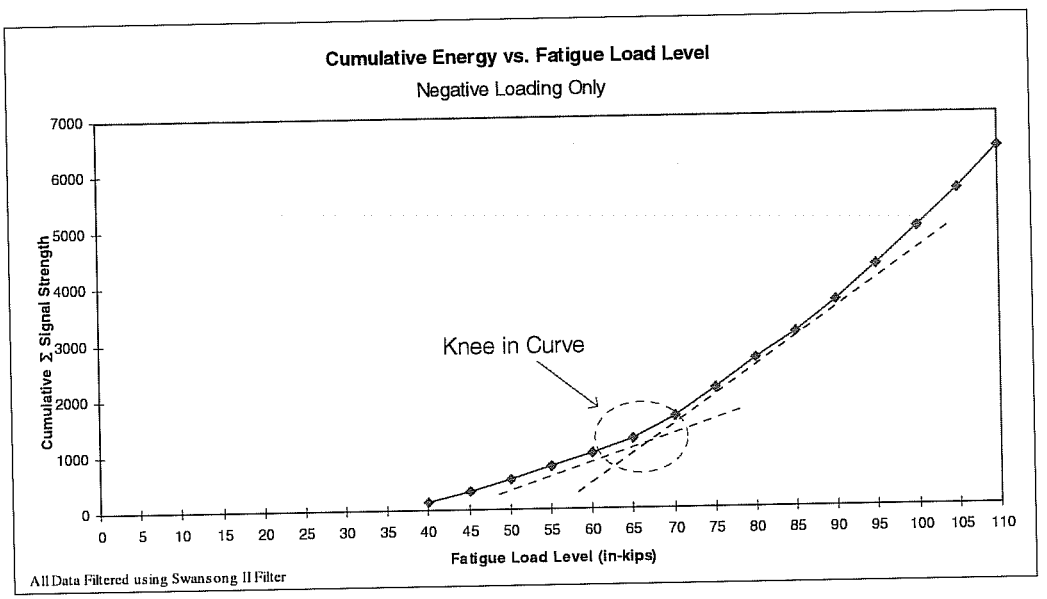

Figure 4.24: Cumulative Energy vs. Fatigue Load Level for Negative Loading. Overload Data Not Included.

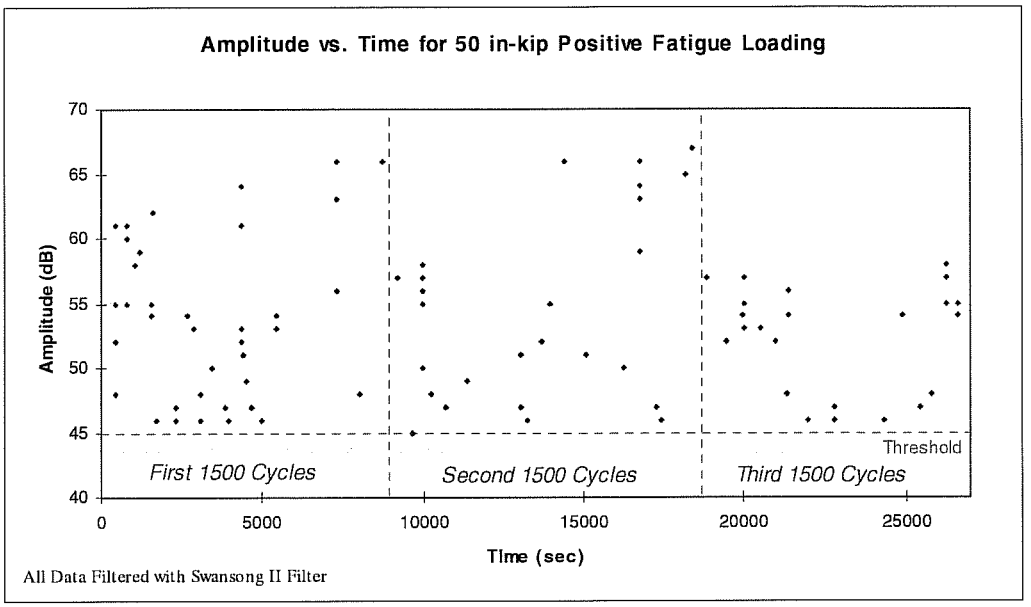

Figure 4.25: Amplitude vs. Time for 50 in-kip Positive Fatigue Loading

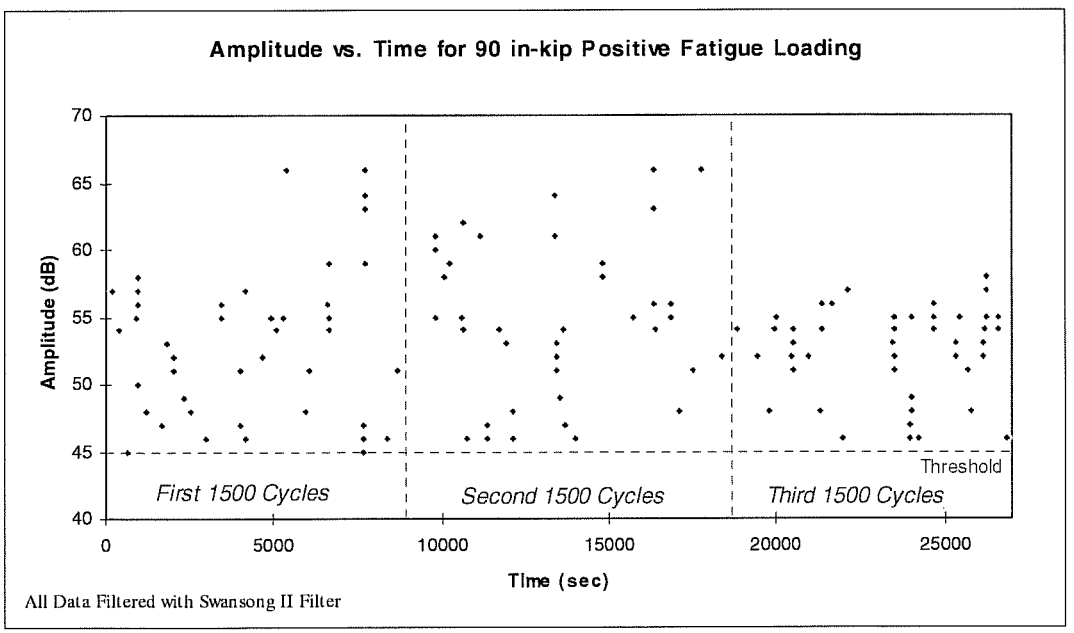

Figure 4.26: Amplitude vs. Time for 90 in-kip Positive Fatigue Loading

The data for the two load levels shows some interesting trends. Although it appears quite random initially, spikes of emission activity (occurring over a time period of less than one tenth of a second) can be seen at certain time increments. It is suspected that these spikes are the result of crack progression or further crack tip yielding. The crack can be seen to be growing, or at the very least worsening, in distinct stages. It is also interesting to note that emission dies down immediately following the overloads. This is consistent with what is being accomplished during the overload – blunting of the crack tip.

A final thing that may be noted about the fatigue data, which was seen indirectly with an examination of the signal strength data from fatigue cycling, is that at the 90 in-kip load level, both the number of hits and the average amplitude of those hits was higher than with the 50 in-kip data. This is further evidence of the failure model proposed, and reinforces the fact that the crack, or at least the effects of the crack, have worsened with increased fatigue loading.

4.3.5 Results from Pearl Harbor Field Test

The loading schedule for the main and boom hoist shafts is shown in Figure 4.31. Acoustic emission data was collected during the entire load schedule. The load data is given in percent of maximum rated load vs. seconds. Before the load was increased, it was returned to the nominal load value of 10% of the rated capacity. Keeping a nominal load on the cable at all times may have helped limit extraneous noise due to cable stretching; however, it was shown that such noise could be removed via post test filtering if it occurred.

Before testing, the Dunnegan Crackers were used to characterize the attenuation characteristics of the shaft in the field. It was confirmed that the sensors were capable of recording actual emission events (not only simulated ones) from all regions of the shaft. The Dunnegan Crackers provided a more realistic waveform than did the other simulation methods. This is shown in Figures 4.27 through 4.30.

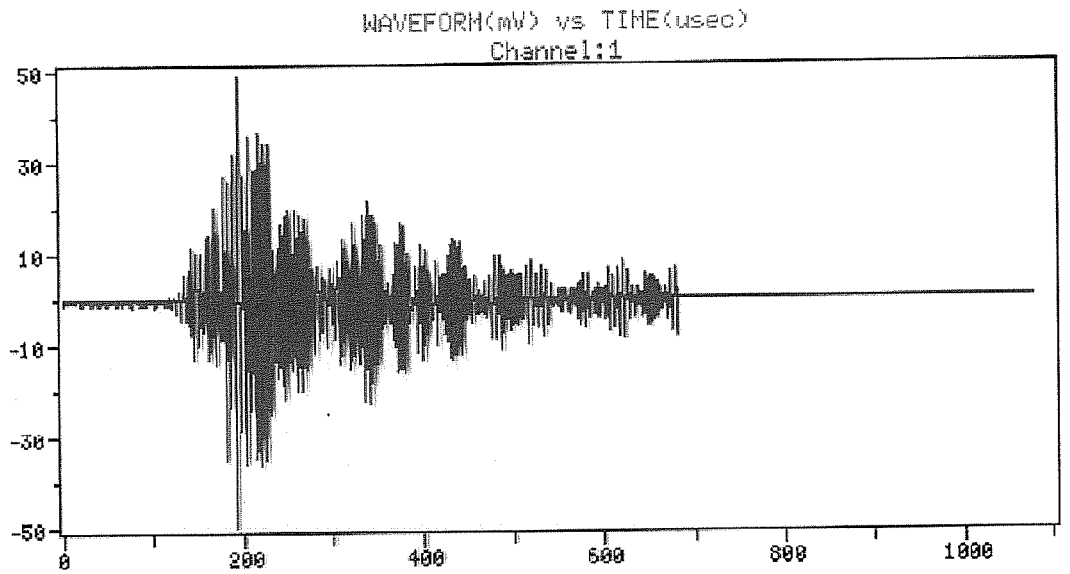

Figure 4.27: Actual AE Event as Recorded by R15I Sensor

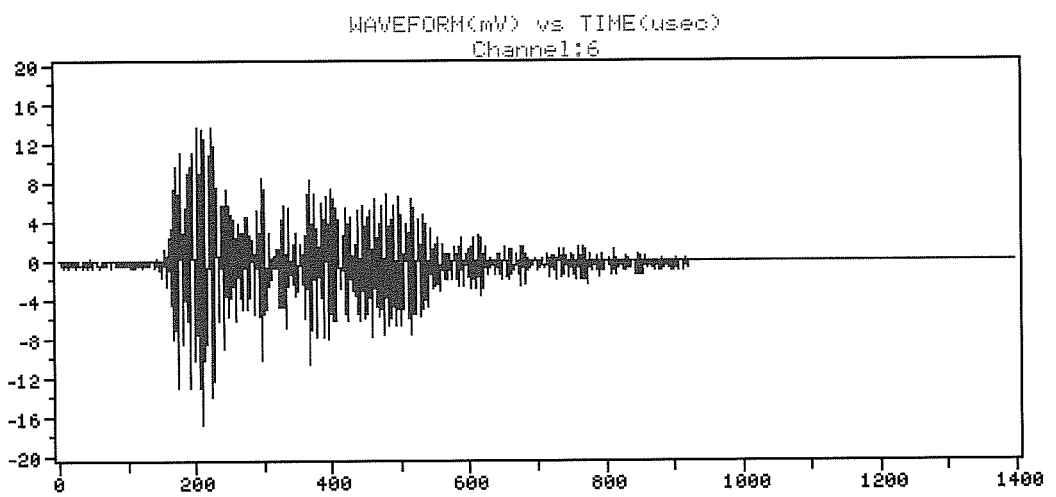

Figure 4.28: Dunnegan Cracker Waveform as Recorded by R15I Sensor

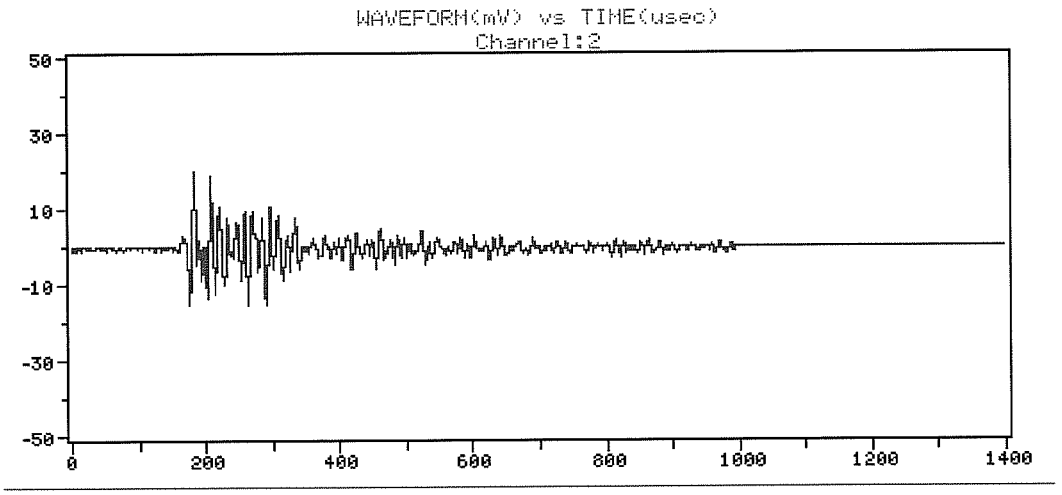

Figure 4.29: Pencil Lead Break Waveform as Recorded by R15I Sensor

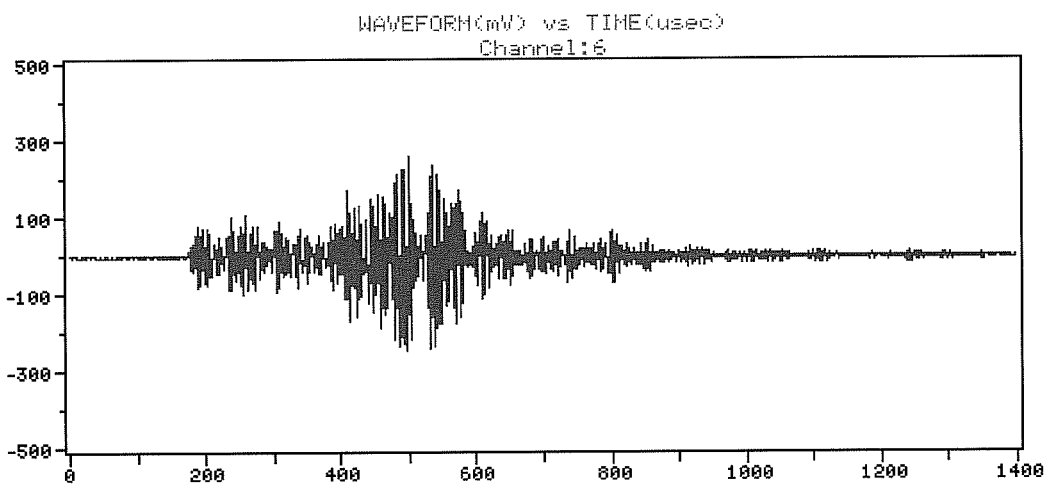

Figure 4.30: PAC AE Pulser Waveform as Recorded by R15I Sensor

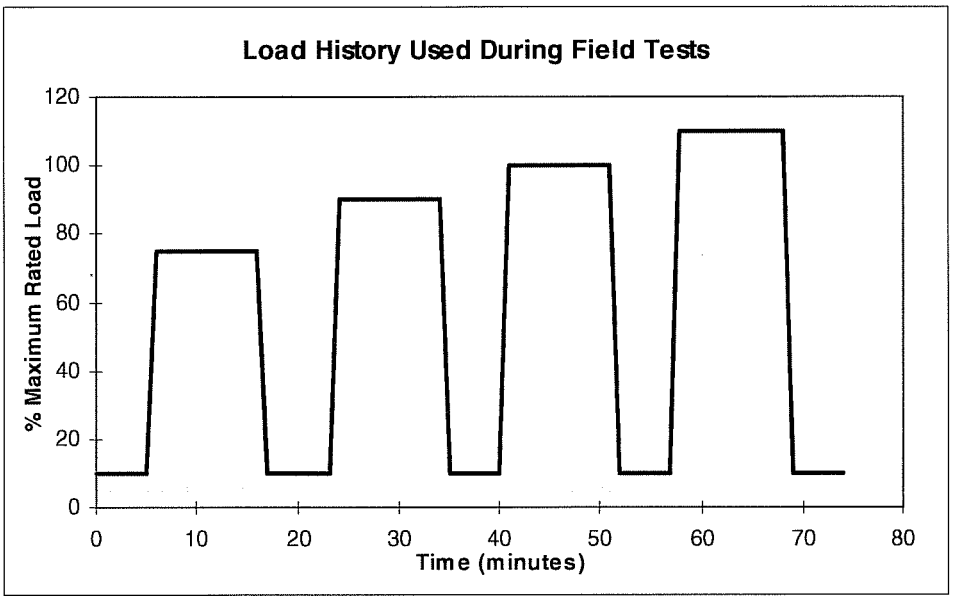

Figure 4.31: Load vs. Time for Main and Boom Hoist Shaft Tests

Main Hoist Shafts

Figure 4.32 shows duration versus amplitude for all the hits collected during the entire load sequence. Hits for both the main hoist drum shaft and the main hoist boom shaft are included here. The data in this figure has not been subjected to any filters, and data due to EMI and mechanical rubbing are present in this plot. This being the case, the total number of AE hits total only 117, quite a small number in AE parlance.

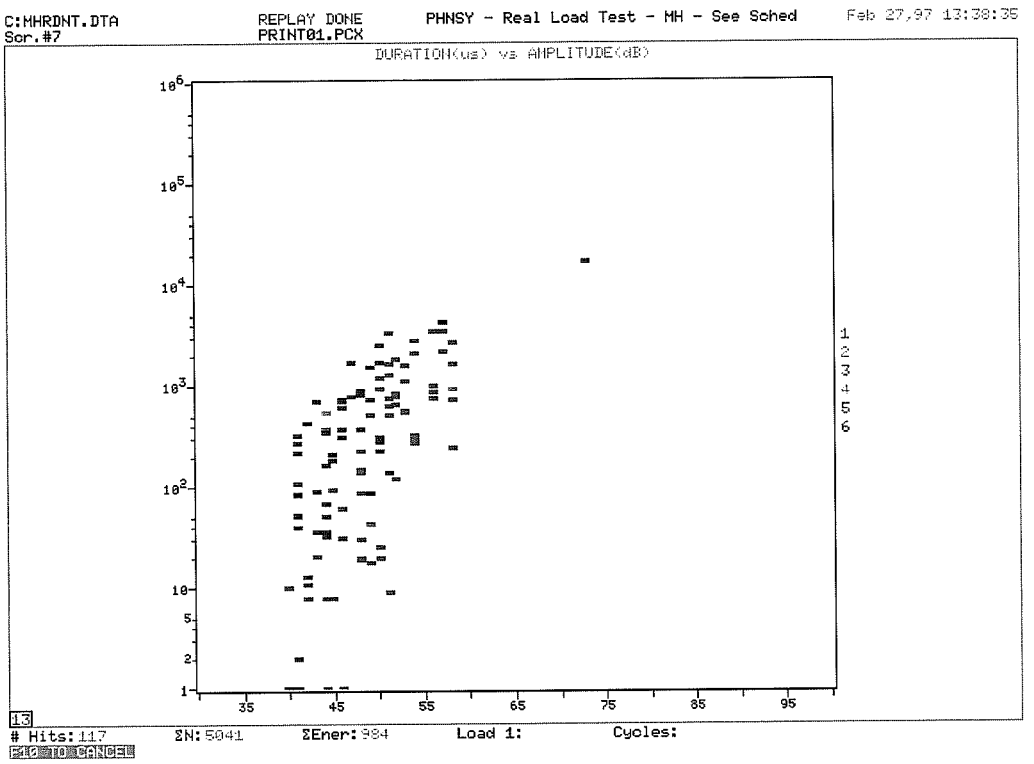

Figure 4.32: Correlation Plot for All Sensors (Included Both Main Hoist Drive and Main Hoist Drum Shaft Sensors). The Data in this Plot is Unfiltered, and Hits from EMI and Mechanical Rubbing are Still Present.

Figure 4.33 shows the number of hits vs. channel of the unfiltered data given in the previous Figure. Note that the majority of the data was detected by the broadband sensors #1 and #3, which were located at each end of the main hoist drum shafts. The broadband sensors were expected to pick up more data than the resonant sensors #2 and #4, which were are only sensitive to hits in a limited frequency range. However, it is interesting to note that the broadband sensor #5 located on the main hoist drive shaft picked up very little data. This indicates that the majority of the AE data collected during the test originated from the drum shaft.

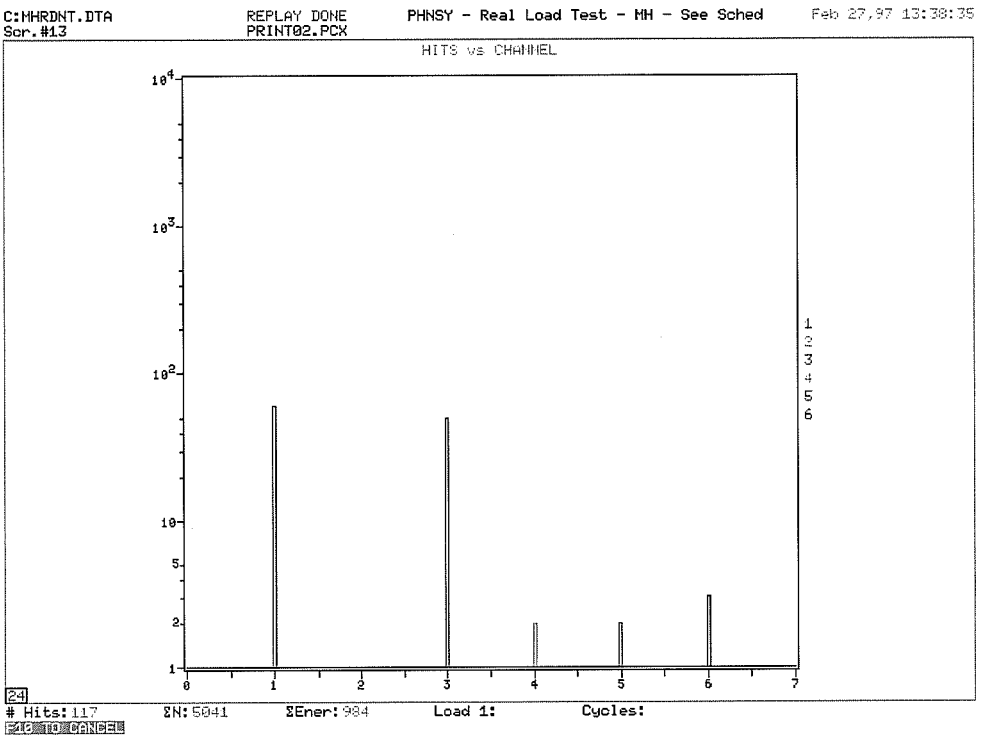

Figure 4.33: Total Number of Hits vs. Channel for the Unfiltered Data given in the Previous Figure

Figure 4.34 shows the remaining hits after removal of EMI only. Note that the number of hits decreased from 117 to 27. The number of hits, qualitatively, is considered to be a very small.

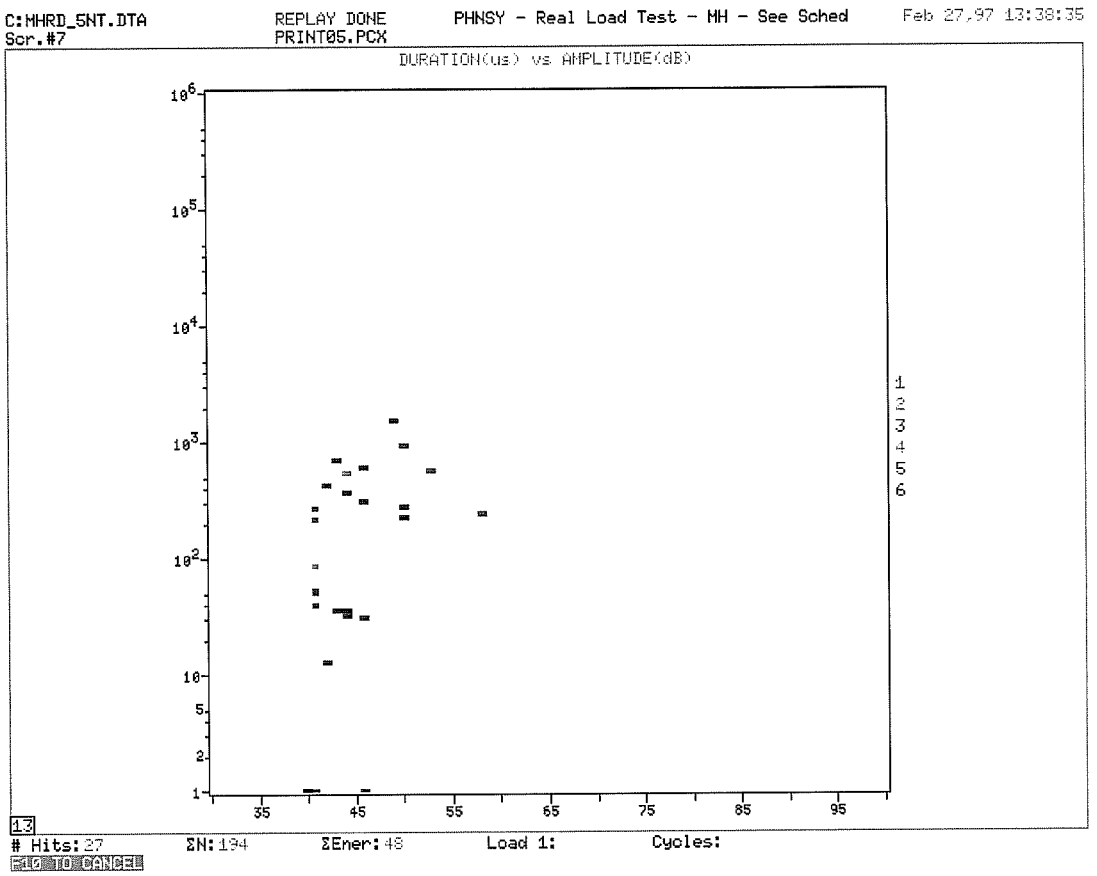

Figure 4.34: Correlation Plot for All Sensors (Including Both Main Hoist Drive and Main Hoist Drum Shaft Sensors). The Data in this Plot has been Filtered to Remove EMI, but Hits from Mechanical Rubbing are Still Present

Before the EMI data was removed, the Swansong II filter was applied. The filter removed no hits from the data set. This indicates that mechanical rubbing was not a problem during main hoist drive and drum shaft testing. Most of the mechanical rubbing problems experienced in the laboratory was likely an artifice of the experimental technique used, and not indicative of what would be experienced in the field. The use of the Swansong filtering technique with the lab data, however, made the results obtained in the laboratory fully applicable for comparison to results obtained in the field.

EMI was a known problem during the field testing. The cause stemmed from banks of relays on the walls of the crane cab opening and closing causing electrical arcing and sparks. The precise time which a control movement was made that caused the relays to activate was manually noted, electronically, in the data file. Using the ATPOST software, all hits occurring within a time zone of ±1 second of the EMI event were removed. This was done by means of a time filter.

The 27 remaining hits, after EMI had been filtered, can thus be considered to be genuine emission. Note that the vast majority of this data has an amplitude lower than 50 dB, and the cumulative signal strength for all 27 hits is a mere $48 \text{ volt} \cdot \text{sec} \times 10^{-5}$.

From a qualitative standpoint, all the data collected suggests that the main hoist shafts do not have large, rapidly growing, structurally significant cracks. Quantitatively, this is also true. The amount and magnitude of emission for the entire test sequence is much smaller than that collected during a single overload procedure on a single shaft in the laboratory. This indicates that no defects are present which are being stressed by the loading scheme used, and in all likelihood the main hoist drive shaft and main hoist drum shafts are fully serviceable.

Boom Hoist Shafts

The data collected from the boom hoist drive and drum shafts was similar in many ways to that collected from the main hoist shafts. A correlation plot of the data, without any filtering, is shown in Figure 4.35. As with the former case, the EMI emitted from the large banks of relays on the walls of the crane cab was responsible for much of the emission detected. The data with the EMI filtered out is shown in Figure 4.36.

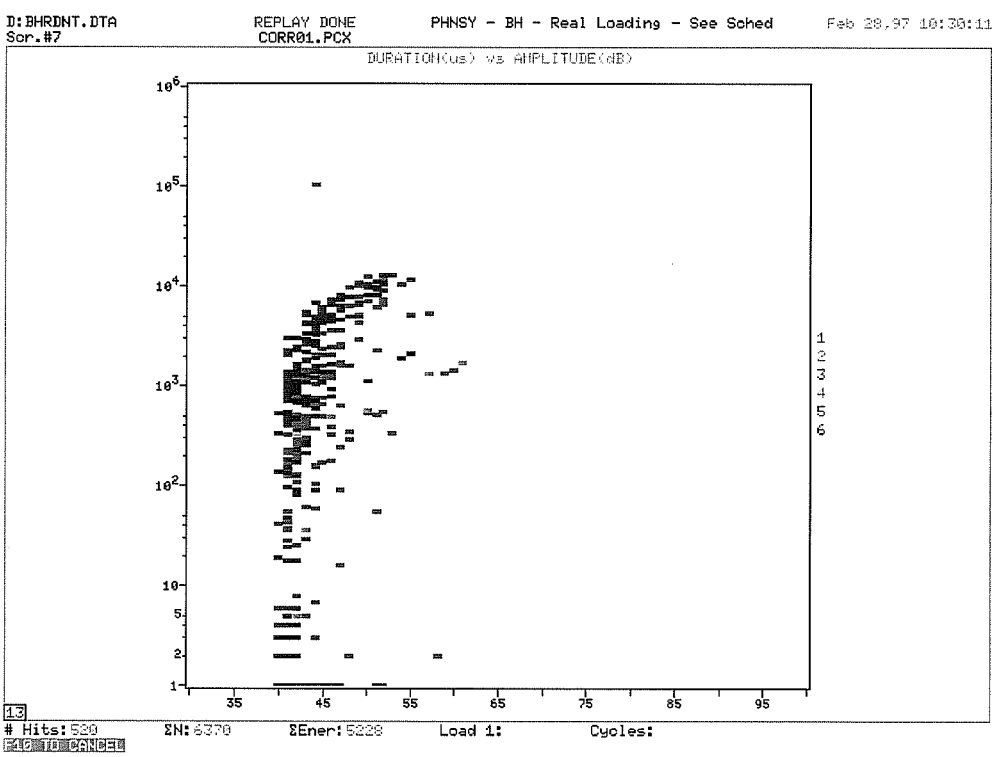

Figure 4.35: Correlation Plot of the Boom Hoist Drive and Drum Shaft Data Before Filtering

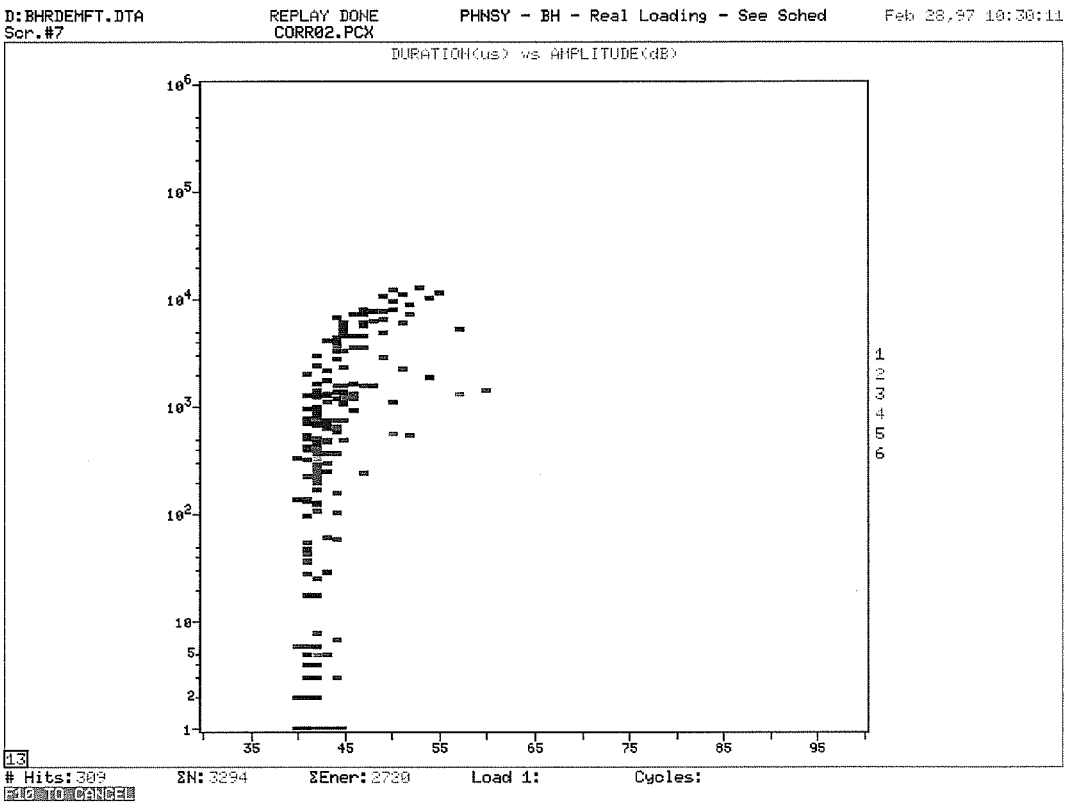

Figure 4.36: Correlation Plot of the Boom Hoist Drive and Drum Shaft Data with EMI Removed

With the EMI removed, the number of recorded hits was reduced from 520 to 309. When the data set was subjected to the Swansong II filter, a further 170 hits were removed, leaving a total of 139 genuine AE hits. This is shown in Figure 4.37. The 170 hits resulting from mechanical rubbing are in stark contrast to the case of the main hoist shafts where no rubbing hits were seen to have been recorded. This observation cannot be explained, but it is speculated that noise borne in the crane is more readily transferred to the boom hoist shafts as opposed to the main hoist shafts because the boom hoist shafts are loaded more directly (i.e., through a fewer number of gears) than their main hoist counterparts.

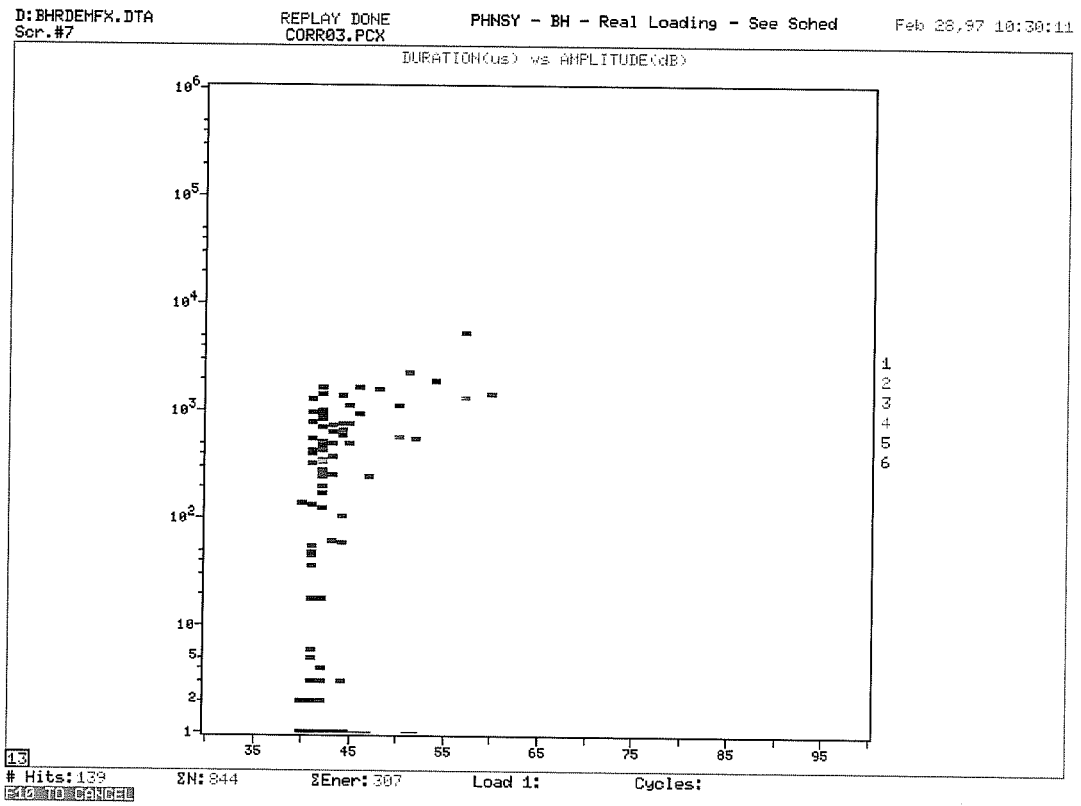

Figure 4.37: Correlation Plot of the Boom Hoist Drive and Drum Shaft Data with EMI and Rubbing Removed

While the 139 AE hits recorded on the boom hoist shaft test is over 5 times the number of genuine AE hits observed on the main hoist test, compared with the laboratory data, it is still a modest number of hits. Also, the amplitude of the vast majority of the hits is below 55 dB; these hits can thus be qualitatively described as low amplitude. Quantitatively, the cumulative signal strength of the filtered data was calculated to be 307 volt $\cdot$ sec $\times 10^{-5}$, again, quite a small number when compared to a single overload cycle in the laboratory.

From a qualitative standpoint, as with the main hoist shafts, all the data collected suggests that the boom hoist shafts do not have large, rapidly growing, structurally significant cracks. Quantitatively, this is also true. The amount and magnitude of emission for the entire test sequence is much smaller than for a single overload procedure on a single shaft during the laboratory testing. This indicates that no defects are present which are being stressed by the loading scheme used, and the boom hoist drive shaft and boom hoist drum shafts are fully serviceable.

4.3.6 Intensity Analysis

An intensity analysis was carried out on the positive overload data using the traditional MONPAC intensity analysis charts. The results for both the 150 kHz sensors and the 300 kHz sensors are shown in Figures 4.38 and 4.39, respectively.

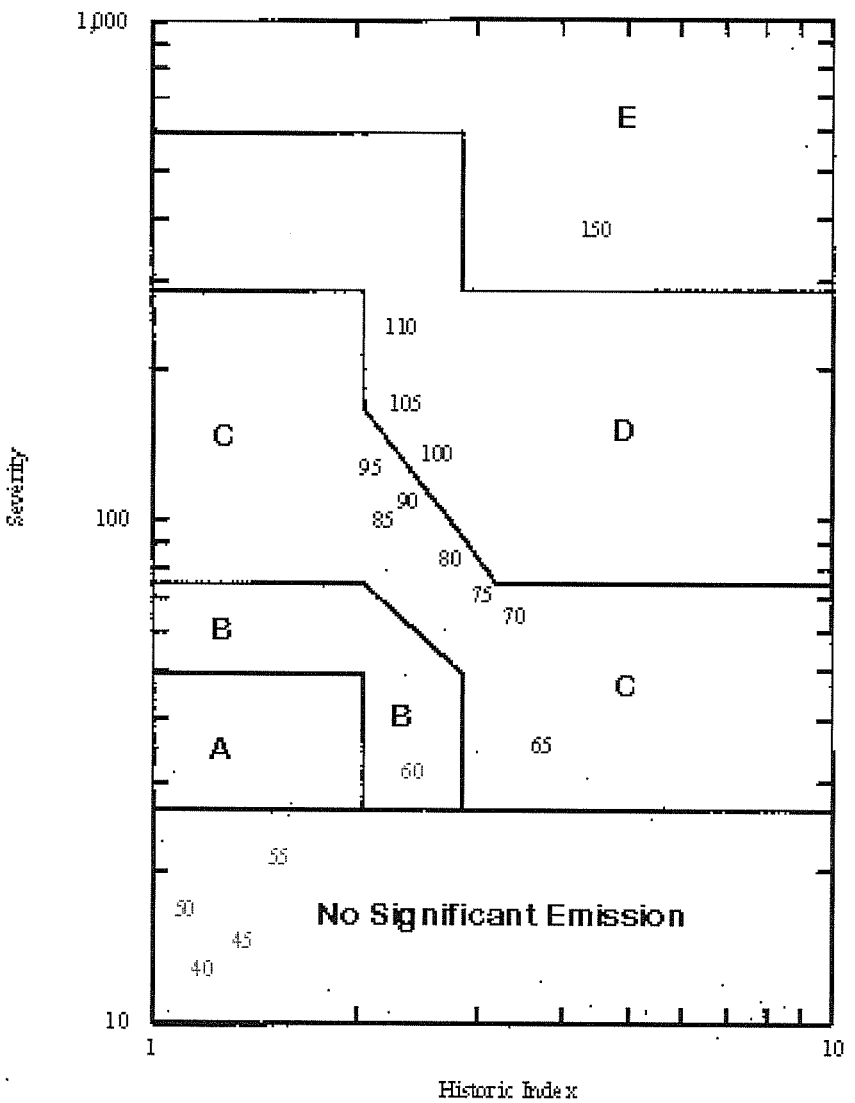

Figure 4.38: MONPAC Intensity Analysis for Positive Overload Data using R15I Sensors

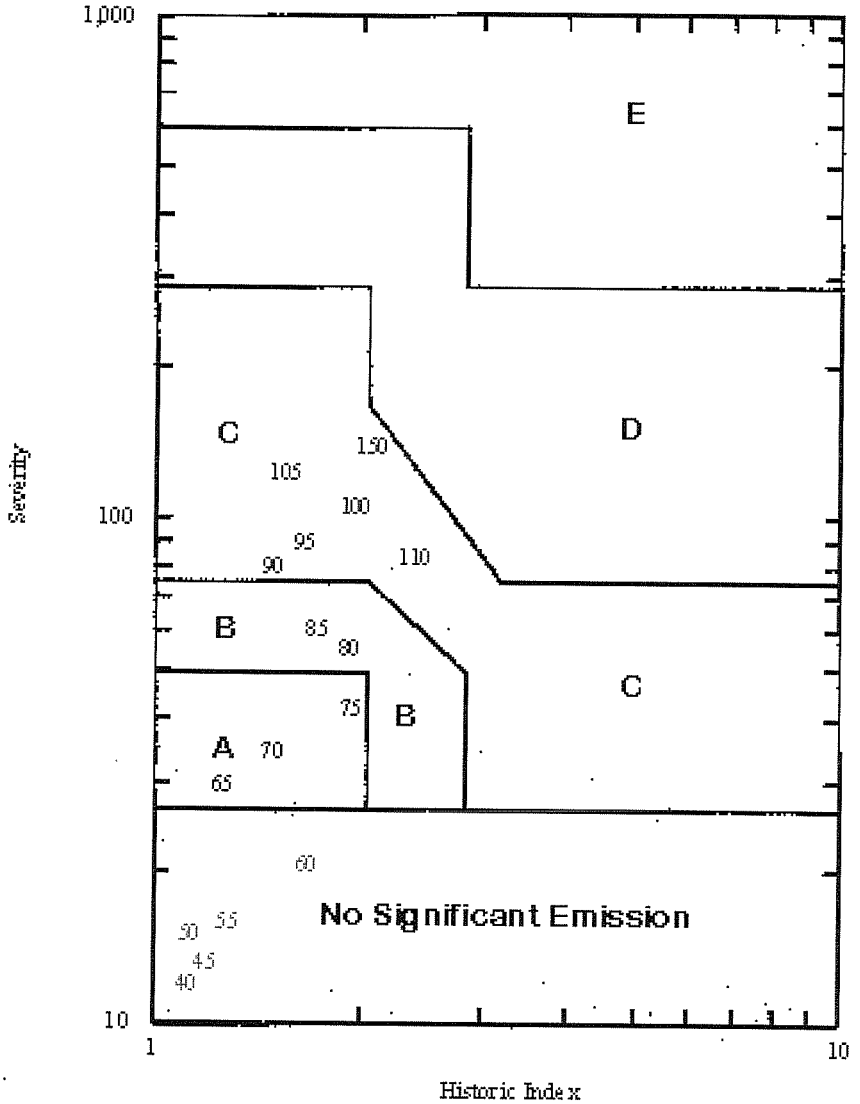

Figure 4.39: **MONPAC Intensity Analysis for Positive Overload Data Using R30I Sensors**

The intensity analysis confirms much of what was seen in the signal strength based analysis. As fatigue load level increases, so does the intensity of the emission. Note the fact that the intensity of the 300 kHz sensor data is less than for the 150 kHz sensor data. As discussed previously, this stems from the higher attenuation at the 300 kHz central frequency range and the reduced sensitivity of the sensors.

Definite "groups" of numbers can be seen in the charts for both frequencies of sensors. These groupings were used to propose a simpler type of intensity analysis chart to be used in the standardized test procedure, as shown and discussed in Chapter 5.

4.3.7 Source Location

The Jolly-Stuart method of zonal source location was used with the lab data to determine the location of the defect in the shaft. For the purposes of the present analysis, overload data taken at fatigue load levels above 75 in-kips was considered, as the analysis up to the present point indicates that damage was definitely occurring in the shaft at 75 in-kips and above. Although each overload was analyzed, a trend in the data quickly became apparent. For the purposes of the present discussion, a typical overload will be discussed in detail with the realization that virtually all the other data, even that taken at fatigue load levels of less than 75 in-kips, follows the identical pattern.

The Jolly-Stuart source location analysis of the R15I data shows that the source of the majority of the emission comes from the front of the shaft, and that the defect is most active under clockwise loading. Similar data is found on the R30I sensors, however, because of the attenuation, fewer second hits are present and no reflections are recorded. The emission from the back of the shaft may be caused by other sources. It was suspected, for example, that the welds attaching the end blocks to the transfer beam were a bit noisy. Those welds were of particularly poor quality, and eventually failed. The number of first hits recorded near the back of the shaft increased slightly as the load level went up, as the weld got closer to failure. Even with the noisy weld at the back end of the shaft, on average, the number of first hits recorded at the back were on the order of one eighth the number recorded at the front of the shaft. When the welds were repaired with ones of suitable quality, virtually all genuine emission from the back end ceased.

Table 4.2: Jolly-Stuart Analysis of 150 kHz and 300 kHz Data for a Typical Overload Cycle. Data Presented is for the Second Overload at a Fatigue Load Level of 85 in-kips.

	Front End Sensors	*Back End Sensors*
R15I SENSORS		
Clockwise Loading		
First Hits	63	8
Ancillary Hits Relative to Front End	6	1
Ancillary Hits Relative to Back End	3	16
Counterclockwise Loading		
First Hits	16	2
Ancillary Hits Relative to Front End	3	1
Ancillary Hits Relative to Back End	1	2
R30I SENSORS		
Clockwise Loading		
First Hits	9	5
Ancillary Hits Relative to Front End	1	0
Ancillary Hits Relative to Back End	0	1
Counterclockwise Loading		
First Hits	2	1
Ancillary Hits Relative to Front End	1	0
Ancillary Hits Relative to Back End	0	1

4.3.8 Results From Other Nondestructive Examination Methods

Following the failure of the first crane shaft, the Navy ordered all other crane shafts from the same manufacturer and of the same vintage to be nondestructively examined for cracks. The Navy's in-house NDT personnel used ultrasonic, eddy current, and wet fluorescent magnetic particle testing to try and detect the cracks. The results were less than satisfactory.

The geometry of the shaft, especially mounted in-situ, makes obtaining good results with traditional NDT methods very difficult. The problems experienced by the Navy were typified in one of the methods giving a positive indication of a defect, and then the other methods would not. In one case, all three methods gave no indications of defects and then the shaft failed catastrophically only a few days after the inspection took place. The failure analysis reveled the presence of a major structural crack in the location where it was suspected when the nondestructive examination was ordered. It is impossible to say with any degree of certainty why the defect was missed. As with most traditional applications of the aforementioned NDT techniques, operator skill and acuity plays a key role in the sensitivity of the method.

Ultrasonic and wet fluorescent magnetic particle testing of the shafts also took place in the laboratory. Matrix Engineering and Testing in Houston, Texas performed the inspections. The shafts used during the static loading phase (phase I) and the dynamic loading phase (phase II) of the laboratory testing were both examined.

The magnetic particle examination showed no indication of defects. The ultrasonic examination, performed by Dr. John McMillan, one of the foremost experts in the field, was attempted using almost every conceivable technique and approach known. Pulse-echo and time of flight diffraction were both attempted, using many different frequencies, sensor configurations, and wave types. Special transducer shoes were even manufactured specifically for the radius of the shafts being inspected, all to no avail. The ultrasonic testing from the outside of the shaft did not reveal with any degree of certainty the presence or location of a crack. There were some indications during the testing, but they were sporadic and difficult to narrow down, much less assess.

The ends of the shaft used during phase I of the testing, which was not to be reused during subsequent testing were sectioned off and sent to Matrix for ultrasonic inspection. Once sectioned, cracks at the inside corner of the keyway were identified. The cracks were small, but still well within the resolution of the ultrasonic techniques attempted. It is suspected that the complex geometry of the specimen prevented the detection of the cracks before sectioning.

This result has profound implications for the Navy, although it is likely one already known to them; the proof being in the commissioning of the present work. The acoustic emission techniques proposed and demonstrated in the laboratory and in the field are global in nature and not as susceptible to operator skill especially when clearly defined failure criteria are used for analyzing the results. This is discussed further in Chapter 5.

4.3.9 Verification

In the present research, as with any other innovative work in science that has never before been done, it is important to establish that the emission did indeed result from a crack which grew during the fatigue cycling. One way of doing this would be to section the shaft, find the crack, further section the specimen along the crack face, and then finally use electron microscopy to identify the location of the crack tip at various stages of the loading history. Because of the very small size of the cracks present in the shaft (indeed, even a small crack can be critical in this material) and the difficulty in locating them using complimentary NDT methods, it is doubtful that this method would have been successful.

Recall, one of the bases on which it was determined that the crack was growing as the number of cycles increased was the increasing energy being released at higher load levels. It could be argued that it was the increasing load which caused the higher emission, and the fatigue cycles between overloads had no part to play. This argument is paramount to saying the crack did not grow and the increased emission from the crack tip at higher load levels was simply a function of the increased stress. In order to counter such an argument, another, more elegant, method than sectioning the shaft was needed to prove that the crack did indeed grew as a function of the fatigue loading.

Such a method was devised, and proved that the crack had to have grown during the fatigue cycling. By simply subjecting the specimen to the overloads and not the intermediary

fatigue cycles, the data resulting from monitoring such a process with acoustic emission could be used to prove the point by inference. This is precisely what was done, and the results are shown in Figure 4.40.

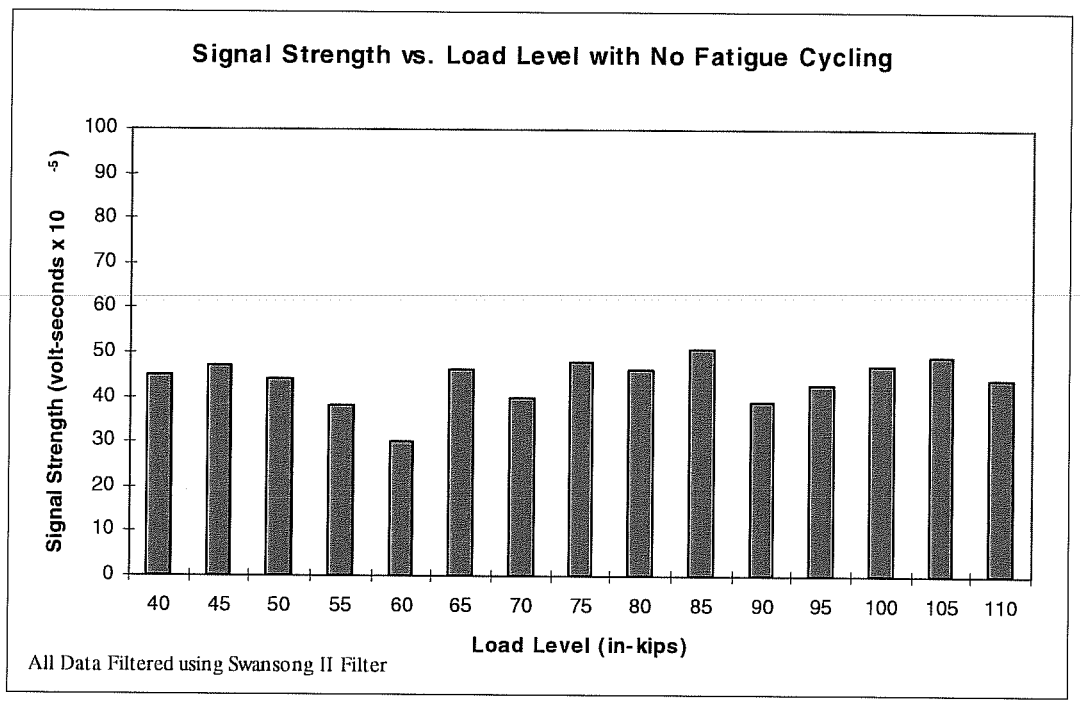

Figure 4.40: Signal Strength vs. Load Level with No Fatigue Loading

The Figure shows that without any fatigue loading, the amount of emission remains quite constant as the load level increases. The fact that no linear increase in emission with load level is seen, as was the case with the overload data, it may be concluded that the increase seen previously was in reality a function of the crack growing under the fatigue cycling, and not an artifice of the increasing stress level. It is interesting to note that the magnitude of the emission is orders of magnitude less than for the equivalent loads under the overload procedures in the fatigue cycling regime. Signal strengths as low as $60 \text{ volt} \cdot \text{sec} \times 10^{-5}$ are very, very small indeed. Figure 4.41 shows a cumulative plot of the data shown in Figure 4.40. Note the absence of a knee in the curve, indicating that the strong trends seen in the fatigue cycling data were not an artifice of the experimental technique used.

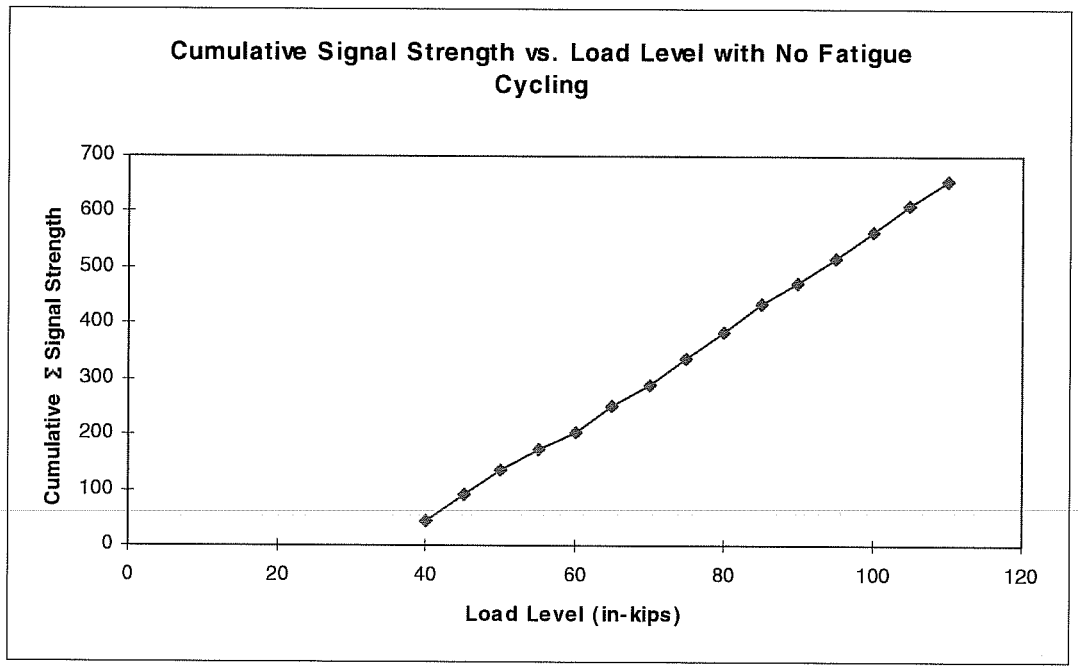

Figure 4.41: **Cumulative Signal Strength vs. Fatigue Load Level. Note absence of knee in curve**

APPLICATIONS

5.1 STANDARDIZED TEST PROCEDURE

Using the results of the data collected in the laboratory during both the static and dynamic loading phases, a test procedure to be used by the Navy's NDT personnel was proposed. The procedure is built upon the American Association of Railroads procedure for railroad and intermodal tank cars[15]. In order to assure that the crane shaft is exposed to a load level greater than any in the previous six months, it is recommended that the AE monitoring be done during annual crane certification proof loading. This is, in essence, an overloading procedure, and thus the results from the overload data obtained in the lab are used as a basis for comparison.

The procedure encompasses all traditional aspects of a standardized AE procedure, including instrument settings and calibration, sensor types and placement, specimen surface preparation, attenuation characterization, personnel qualification and interpretation of test data.

The procedure allows for two different operating frequency ranges for sensors, preamplifiers, filters and other frequency sensitive instrumentation. The two ranges are centered on a nominal frequency of 150 kHz and 300 kHz. Selection of the appropriate operating frequency depends on the characteristics of the emission recorded during a preliminary background noise check. The 150 kHz range is preferred. Separate evaluation criteria are proposed for the two operating ranges.

The procedure requires mechanical loading of the shaft. Loading is accomplished by pulling against a large mass while monitoring with a load cell. Normally, the load that is lifted off the ground during certification is used as the large mass. Details of the loading sequence follow. The test procedure specifies loading to a maximum load determined on the basis of the crane's design load. The procedure does not apply to shafts loaded above the maximum rated load during the six month period prior to performing an AE test. Typically, the maximum AE test load is 110 percent of the maximum rated load. The loading test assesses the shaft for defects such as cracks, corrosion, and other defects which are stressed during loading.

Two loading options are proposed in the procedure. The first applies load to the shaft of interest which remains in a fixed position. The second varies the angular position if the shaft under a number of successive loadings. The angular position of the shaft is changed to allow bending moments and shear stresses to be applied in different directions in order to develop the most serious combination of stresses. The fixed position loading was used for the field test at Pearl Harbor. The variable shaft position was suggested as a result of the work carried out during the first field test, (to ensure that the crack tip is activated under one of the loading directions) and is recommended for subsequent tests.

The master load schedule, in terms of percent of maximum rated load, is proposed as follows:

- Begin by applying a load of 10% (-0% +5%) of maximum rated capacity. Use this load to keep tension on the shaft: it becomes the baseline, or minimum load.

- Increase to 75% (-0% +5%); hold for 10 minutes; decrease to 10%; hold for 5 minutes.
- Increase to 90% (-0% +5%); hold for 10 minutes; decrease to 10%; hold for 5 minutes.
- Increase to 100% (-0% +5%); hold for 10 minutes; decrease to 10%; hold for 5 minutes.
- Optional: Increase to 110% (-0% +5%); hold for 10 minutes; decrease to 10%; hold for 5 minutes.

The load schedule for variable shaft position test is essentially similar in terms of load magnitudes, but at each load level a step is included to release the load, lower the boom slightly, and repeat 3 times to obtain other angular rotations.

After the data has been collected, post-test filters are applied. The two filters suggested for use are the Swansong II filter, as it was seen to be very effective both in the lab and in the field in removing background noise.

Evaluation criteria for each individual channel are proposed. Table 5.1 details the acceptable emission levels for which a shaft can be considered safe. The values in the table are a direct product of the static and dynamic loading phase laboratory testing carried out at the Ferguson Structural Engineering Laboratory.

Table 5.1: Individual Channel Acceptance Criteria

Criterion	*150 kHz Sensors*	*300 kHz Sensors*
Cumulative Signal Strength During Loading and Load Holds, Volts-Seconds^{-5}	< 350	< 100
Felicity Ratio	> 0.95	>0 .95
Cumulative Emission During Load Holds, Hits	20	10

Additionally, an intensity analysis using the traditional parameters of Historic Index and Severity has been incorporated into the evaluation criteria. Again, there are different criteria for different sensor types. The intensity chart for 150 kHz sensors is shown in Figure 5.1. The intensity chart for 300 kHz sensors is shown in Figure 5.2.

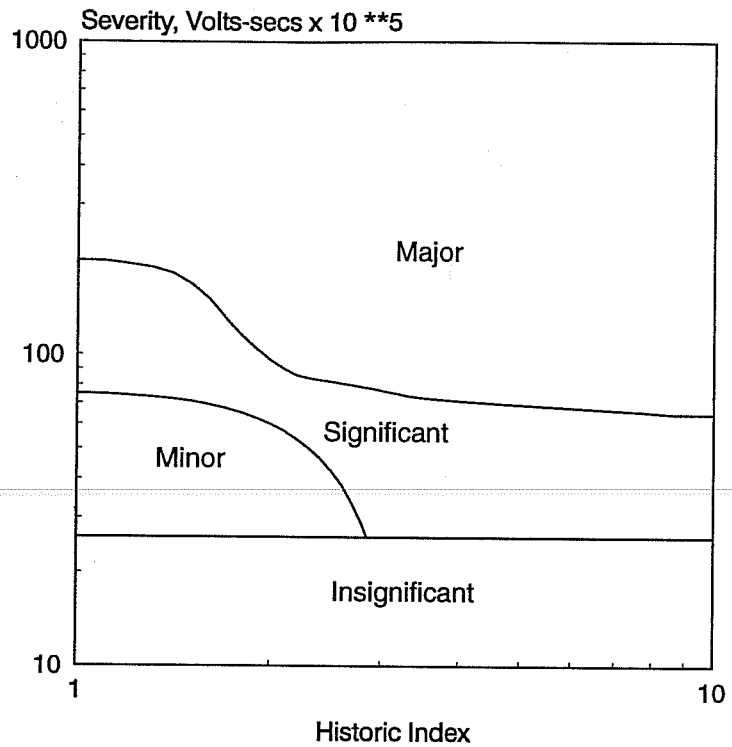

Figure 5.1: Intensity Chart for 150 kHz Sensors

Based on the intensity analysis, minimum recommended follow-up actions were proposed:

- **Insignificant**: Emission source is structurally insignificant.
- **Minor**: Minor emission Note for future reference. Visually inspect accessible areas.
- **Significant**: Significant structural defect requiring follow-up evaluation. As a minimum, evaluation should include further data analysis and visual inspection of accessible areas. Consideration should be given to comprehensive nondestructive examination, retest, and increased frequency of inspection.
- **Major**: Major structural defect. Immediate shutdown and nondestructive examination.

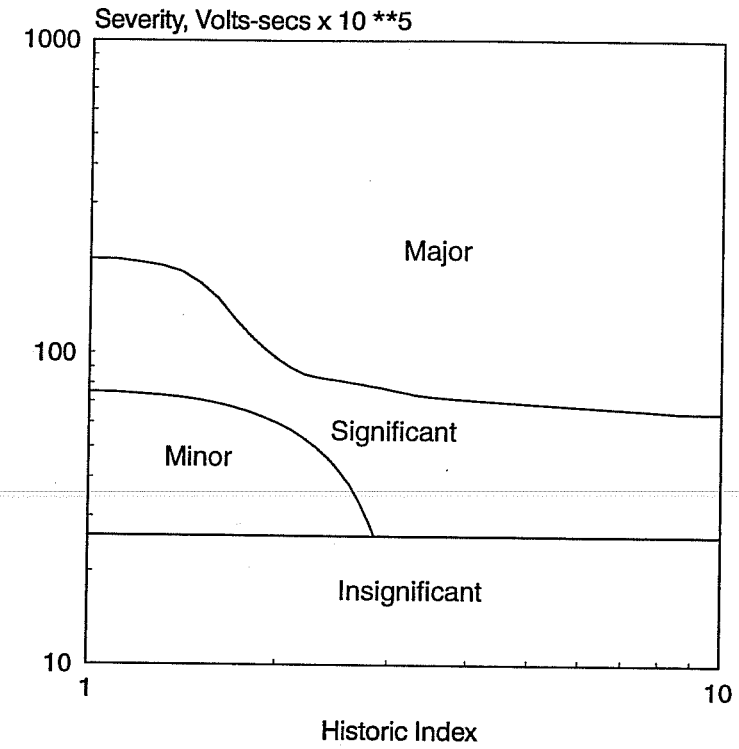

Figure 5.2: Intensity Chart for 300 kHz Sensors

Using the above evaluation criteria in conjunction with the data obtained during the field test at Pearl Harbor, as detailed in Chapter 4 and summarized in Table 5.1, crane P-64 which had been taken out of service because of a shaft failure in its sister crane, was judged to be structurally sound and its return to service was recommended.

5.2 COMMERCIAL AND GOVERNMENT APPLICATIONS

The present work is widely applicable to both government and commercial/industrial applications. The Navy, Department of Defense, and other government clients can use the results of the experimentation as well as the proposed standardized test procedure directly to diagnose the health of cranes in their world theater of operation. The inspections need not be carried out by government personnel, the test procedure may be included in contract bids for consultants or civilian contractors.Some potential commercial/industrial clients include crane owners at commercial ports, and others in the shipbuilding, steel, railroad, and oil industries. Additional applications include the paper and textile industries, where large diameter shafts are used in spools during manufacturing.

Table 7.1: Evaluation of Field Test Data using Criteria Defined in Test Procedure

CRITERIA	*MAIN HOIST SHAFTS*		*BOOM HOIST SHAFTS*	
Cumulative Signal Strength During Loading and Load Holds	**182** (<350)	✓	**20** (<100)	✓
Felicity Ratio	**0.98** (>0.95)	✓	**0.98** (>0.95)	✓
Cumulative Emission During Load Holds	**7** (<20)	✓	0 (<10)	✓
Significance	Insignificant	✓	Insignificant	✓
RESULT	PASS		PASS	

CONCLUSIONS

Acoustic emission is a powerful nondestructive testing technique that has wide ranging applications in traditional civil engineering environments. The experimental program carried out during the research reported here showed that by using acoustic emission, the condition and state of serviceability of Naval portal crane shafts can be definitively and conclusively identified.

The laboratory data showed that acoustic emission can be used to detect the presence of fatigue cracks. Indeed, the larger and more significant the crack is, the more emission it will cause. Traditional parameters such as signal strength, number of hits during load hold, intensity analysis, and the Felicity ratio can be used together to determine the state to which a crane shaft is damaged, and suggest a course of action for further inspection or usage.

The technology was seen to be effective in the relatively noisy environment of dynamic fatigue testing. By acoustically insulating the shaft from the test stand, and being judicious in the selection of sensors, thresholds, and a post-test filtering regime, the background noise problems did not in any way prevent the acquisition of genuine and usable data. The data correlated well to that obtained during static load testing where, as expected, background noise problems were almost non-existent.

The use of 150 kHz and 300 kHz integral resonant sensors, with a 45 dB threshold was effective both in the laboratory and in the field. The Swansong II filter was all that was needed to remove any remaining background noise that was encountered. The effectiveness of the filtering techniques was specifically verified by examining the digital waveforms in the data before and after filtering. Characteristically bad data was completely removed from the data sets in all cases by using the filters.

The work carried out in the laboratory transferred over to field testing quite well. In part this was due to the extreme care that was taken when devising the laboratory test setup to closely replicate field conditions. The shafts tested in the lab were generally shorter than those found in the field. This was not a problem, however, because of the shaft's excellent acoustic transmission properties, as well as the fact that the most critical areas to monitor are the shaft ends, which behave independently of length.

The field test carried out at the Pearl Harbor Naval Shipyard helped identify potential problems that might be encountered during field testing which were not seen in the highly ideal environment of a laboratory. This test, in conjunction with the lab research, led to a proposed standardized test procedure which effectively documents the techniques necessary to test and interpret data from a load test where the critical shafts are monitored with acoustic emission instrumentation. The laboratory data taken during overload cycles were mainly used for this purpose.

The Jolly-Stuart method of zonal source location is effective in determining from which end of the shaft the emission was generated. This result allows for a detailed follow up inspection with a complementary nondestructive testing technique to more clearly identify the geometry of the defect, and to further dictate follow-up action. Some of the traditional nondestructive testing techniques such as magnetic particle, eddy current, and ultrasonic inspection, however, have been shown by the Navy and by this research to not be as sensitive

as acoustic emission in locating structural defects. The Navy's nondestructive testing branch has struggled for years with the lack of consistency in finding defects using an entire host of methods. This, in part, may be attributed to the complex geometry of the key and keyway interface in the shaft, and furthers the need for a global nondestructive technique to be adopted. Acoustic emission is one such technique, one which can be applied to a wide range of materials and geometries, and one whose data analysis results are readily identifiable and relatively independent of the acuity of the operator.

Fundamentally, this research has valuable technical information concerning fatigue crack development and detection. This work has broad implications beyond the present research. The laboratory program shows how a well conceived program and complementary field test program can be used to apply acoustic emission technology to new applications. Future research in acoustic emission stemming from this research includes basic lab work in data analysis and signature analysis. Indeed, there is a wealth of data that was collected during the course of this research that can be analyzed.

During a time in history where cost cutbacks and financial restraint rule the day, material infrastructure is being called upon to perform its function well past its intended design life. Enabling this to occur safely is clearly in the interest of most. The decisions which are made must be based on clearly defined criteria on the existing condition of the subject of study. A global nondestructive testing technique that can be used to quickly, inexpensively and decisively evaluate that condition empowers those who make the decisions to do so using as much information as possible. This enables the greatest common good for the greatest public safety, which after all is the primary duty and responsibility of a structual engineer.

REFERENCES

1. Dingus, M., "Methods for Nondestructive Analysis of Fatigue in Cranes, " Report 95-225, Texas Research Institute Austin, Austin, TX.

2. Akhtar, A., J.Y. Wong, G.S. Bhuyan, C.T. Webster, and D. Kung, "Acoustic Emission Testing of Steel Cylinders for the Storage of Natural Gas on Vehicles," NDT&E International, Vol. 25, No. 3, Butterworth-Heinemann Ltd., UK, 1992.

3. Courtesy of the Physical Acoustic Corporation, Princeton, NJ. Calibration Curve for R15I Sensor; Serial Number EF90. Reprinted with permission.

4. Bassim, M.N., and F. Hamel, "Acoustic Emission Associated with Crack Propagation in Fatigue," 1981 Paper Summaries, ASNT Spring and Fall National Conferences, ASTN, Columbus, OH, 1981.

5. Berkovitz, A. and D. Fang, "Fatigue Design Model Based on Damage Mechanisms Revealed by Acoustic Emission Measurements," Durability and Reliability of Airframes, Transactions of the ASME, 1995.

6. Heiple, C.R., S.H. Carpenter, and D.L. Armentrout, "Comments on the Origin of Acoustic Emission in Fatigue Testing of Aluminum Alloys," Journal of Acoustic Emission, Vol. 10, No. 3, January 1992.

7. Heiple, C.R., and S.H. Carpenter, "Acoustic Emission Produced by Deformation of Metals and Alloys - A Review," Parts I & II, Journal of Acoustic Emission, Vol. 10, No. 3, January 1992.

8. "Acoustic Emssion Examination of Metallic Vessels During Pressure Testing", Section V, Article 12, Boiler and Pressure Vessel Code, American Society of Mechanical Engineers, New York, NY.

9. Williams, R.V., Acoustic Emission, Adan Hilger Ltd., Briston, U.K., 1990

10. Whittaker, J.W., "A Note on the Prediction of Fatigue Life of Metal Structures by Use of the Felicity Effect," Journal of Acoustic Emission, Vol. 5, No. 4, Oct. 1986.

11. Siedlaczek, J., S. Pilecki, and F. Dusek, "Acoustic Emssion of the 45HNMFA Structural Steel during Low-Cycle Fatigue," Journal of Acoustic Emission, Vol. 10, No. 3, Jan. 1992.

12. Almeida, A. and E. Hill, "Neural Network Detection of Fatigue Crack Growth in Riveted Joints Using an Acoustic Emission Approach," Materials Evaluation, Vol. 53, No. 1, ASNT, Columbus, OH, 1995.

13. Scala, C.M., S.J. Bowles, and I.G. Scott, "The Development of Acoustic Emission for Structural Integrity Monitoring of Aircraft," ARL/MAT-R-120, Department of Defense, Aeronautical Research Laboratory, Australia, 1988.

14. Broek, D., Elementary Fracture Mechanics, Kluwer Academic Publishers, Norwell, MA, USA. 1991.

15. "Procedure for Acoustic Emission Evaluation of Tank Cars and IM-101 Tanks," Association of American Railroads, Operations and Maintenance Department, Mechanical Division, Washington, D.C.

16. Fowler, T.J., J.A. Blessing, P.J. Conlisk, and T.L. Swanson, "The MONPAC System," Journal of Acoustic Emission, Vol. 8, No. 3, 1989.

17. Fowler, T.J., "Acoustic Emission Testing of Chemical Industry Vessels", *Progress in Acoustic Emission II,* Proceedings for the 7th International Acoustic Emission Symposium, Zao, Japan, The Japanese Society for Nondestructive Inspection, 1984.

18. ASTM. "Standard Terminology for Nondestructive Examinations," Standard E1316. Annual Book of ASTM Standards, Nondestructive Testing, Vol. 03.03. American Society for Testing and Materials, Philadelphia, P.A. 1994.